isvr Institute of Sound and Vibration Research

Design of an Inertial, Electrodynamic Actuator with Internal Velocity Sensor for Active Vibration Damping of Lightweight, Flexible Structures

C.Paulitsch, R. Boonen, P. Gardonio, P. Sas and S.J. Elliott

ISVR Technical Memorandum No 940

August 2004

University of Southampton

SCIENTIFIC PUBLICATIONS BY THE ISVR

Technical Reports are published to promote timely dissemination of research results by ISVR personnel. This medium permits more detailed presentation than is usually acceptable for scientific journals. Responsibility for both the content and any opinions expressed rests entirely with the author(s).

Technical Memoranda are produced to enable the early or preliminary release of information by ISVR personnel where such release is deemed to the appropriate. Information contained in these memoranda may be incomplete, or form part of a continuing programme; this should be borne in mind when using or quoting from these documents.

Contract Reports are produced to record the results of scientific work carried out for sponsors, under contract. The ISVR treats these reports as confidential to sponsors and does not make them available for general circulation. Individual sponsors may, however, authorize subsequent release of the material.

UNIVERSITY OF SOUTHAMPTON

INSTITUTE OF SOUND AND VIBRATION RESEARCH

SIGNAL PROCESSING & CONTROL GROUP

Design of an Inertial, Electrodynamic Actuator with Internal Velocity Sensor for Active Vibration Damping of Lightweight, Flexible Structures

by

C.Paulitsch, R.Boonen, P.Gardonio, P.Sas and S.J.Elliott

ISVR Technical Memorandum N° 940

August 2004

Authorised for issue by
Prof S J Elliott
Group Chairman

ABSTRACT

The design of a miniature, electrodynamic, inertial actuator with internal relative velocity feedback for active vibration control of lightweight structures is presented. Dynamic and electromagnetic requirements associated to active and semi-active vibration control are compiled. A design concept for the electromagnetic circuit is selected and based on requirements it is optimised using finite element analysis (FEA). A combination of solutions for the mechanical functions, suspension, guide and cover, is found and the dynamic, mechanical behaviour is checked using FEA to fulfil requirements. The different steps of the manufacturing process of the chosen design are illustrated and difficulties are highlighted. Finally dynamic parameters of the actuator are determined measuring various frequency response functions (FRFs) and the maximum operating range is estimated. Requirements are compared to design results.

INDEX

1. INTRODUCTION

Large vibrations may lead to failure of mechanical structures or compromise the functionality of attached sensitive devices. Vibration suppression is especially important for lightweight structures with low damping. Despite good static properties under dynamic loads vibrations may be amplified at resonance. Moreover due to the reduced impedance of the structure outside the stiffened load path noise transmission may be enhanced.

In order to prevent failure or reduce noise radiation active vibration damping may add a higher degree of damping than passive means of the same weight when actuators, sensors and the control scheme are properly chosen. Passive means are especially disadvantageous for low frequency noise attenuation [1] since a large amount of material is required to be effective. Flexible structures have multiple resonance frequencies that all should be controlled when they are exposed to broadband excitation. But often these resonance and anti-resonance frequencies are not precisely known or change during operation. Therefore collocated direct velocity feedback using a dual actuator-sensor pair [2] should be used so that in theory unconditional stability is guaranteed [3] and a large amount of damping can be added.

Commonly used sensors are point accelerometers that usually have a high cut-off frequency. Electronic integration of the measured acceleration signal is possible even at low frequencies when appropriate signal processing equipment is used. Since distributed actuators exert a moment [4] on the attached structure they are not dual to this kind of point sensor. They also excite in plane vibrations that cannot be sensed with a point sensor so that control spill-over occurs [5]. Due to a small lever effect for transformation of the in-plane force into an out of plane force [6] at low frequencies they also have limited control authority for bending vibrations that are important for sound radiation [7]. Excitation effectiveness increases with higher frequencies so that very high amplitudes together with an important phase shift are reached at the cut-off frequency of the accelerometer [8], which is difficult to control. Usually larger vibration reduction is possible at lower frequencies when point force actuators are used that also do not couple into in-plane modes [9, 10]. Additionally a point force actuator is dual and collocated with a point sensor. The phase shift of accelerometers at high frequencies and the electronic integration can potentially be avoided when a self-sensing actuator, which is a transducer that is simultaneously used as sensor and actuator, is applied. Therefore this study considers point force actuators together with a point sensor in a self-sensing combination.

In practical applications a point force actuator often does not react relative to a solid ground, but an inertial mass is added as shown in Figure 1.1. Following [11] the resonance frequency of the added spring-mass system of this inertial actuator should be well damped and it should be lower than the smallest, structural resonance frequency to be controlled. Hence the inertial actuator should be designed to be well damped, have a large, inertial mass M and low stiffness K of the actuator suspension. However, in a practical system the increase in mass is limited by the requirement of a lightweight design and a lower limit on the suspension stiffness is given by the yield strength of the used suspension material. Alternatively internal damping could be added by internal relative velocity feedback using a self-sensing algorithm [12] or an internal velocity sensor. Additionally a low inertial mass implies a high actuator stroke in order to generate the necessary transmitted force F_t. The generation mechanism of the actuation force F_a should not add much additional weight or should be integrated into the reaction mass of the actuator. In particular the contrasting requirements compiled in Table 1.1 demand a force

generation mechanism with low added mass, high stroke, high internal damping and as small as possible suspension stiffness.

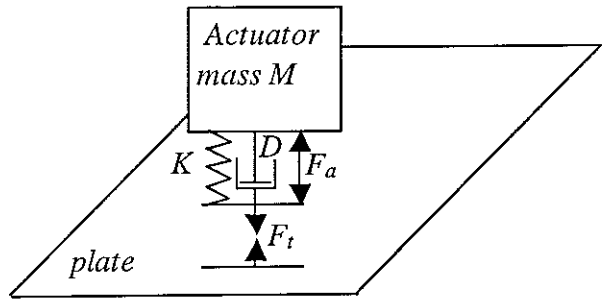

Figure 1.1: *Schematic view of an inertial actuator on a lightweight plate*

Following [13] actuator technologies with mechanical output include electromagnetic, fluid, bimetallic, electrochemical, electrorheological, piezoelectric, magnetostrictive, shape memory and micro actuators. Braided pneumatic actuators [14] can also be used as actuators for mechanical systems. Only small forces F_a and small displacements can be generated by microactuators [15], chemomechanical actuators have a large time constant, electrochemical actuators are still in development, magnetorheological, electrorheological and hydraulic actuators have a response time in the milliseconds range and shape memory, bimetallic and braided pneumatic actuators are even slower. A subclass of actuators are electromechanical transducers that can be either classified in inductive, capacitive or resistive actuators or following the used materials [16]. Magnetostrictive and piezoelectric actuators allow large forces and small displacements [17], whereas electromagnetic actuators can be designed for a large force range and large displacements. In contrast to magnetostrictive actuators piezoelectric actuators do not need an external magnetic field generator.

Table 1.1: *List of contrasting requirements and proposed solution (underlined)*

Contrasting requirements
A **lightweight design** implies low mass and **small dimensions** that lead to a **lower limit on vertical suspension stiffness**.
A **high transmitted actuator force** can be realized by a **high inertial mass** and **a high stroke** that **limits possible force generation mechanisms**.
A **low lower limit on the control bandwidth** implies a **low, well-damped resonance frequency** of the actuator that can be realized by a **high inertial mass, low suspension stiffness** and **high internal damping**.
A **high actuation force** tends to **increase the actuator mass** and **limits possible force generation mechanisms**.

Figure 1.2 from [18] shows the blocked force - free displacement characteristic and the weight of various linear piezoelectric actuator technologies. As a general tendency, not without exceptions, the weight increases with increased free displacement and reduced blocked force for a given actuator technology. Hence, although the reaction mass is reduced using a large stroke the force generation mechanism increases the required mass again for larger strokes.

Moreover piezoelectric actuators have a high stiffness so that it is difficult to obtain a low resonance frequency that is required for stability of inertial actuators in an absolute velocity feedback loop. Internal actuator damping could be added electronically.

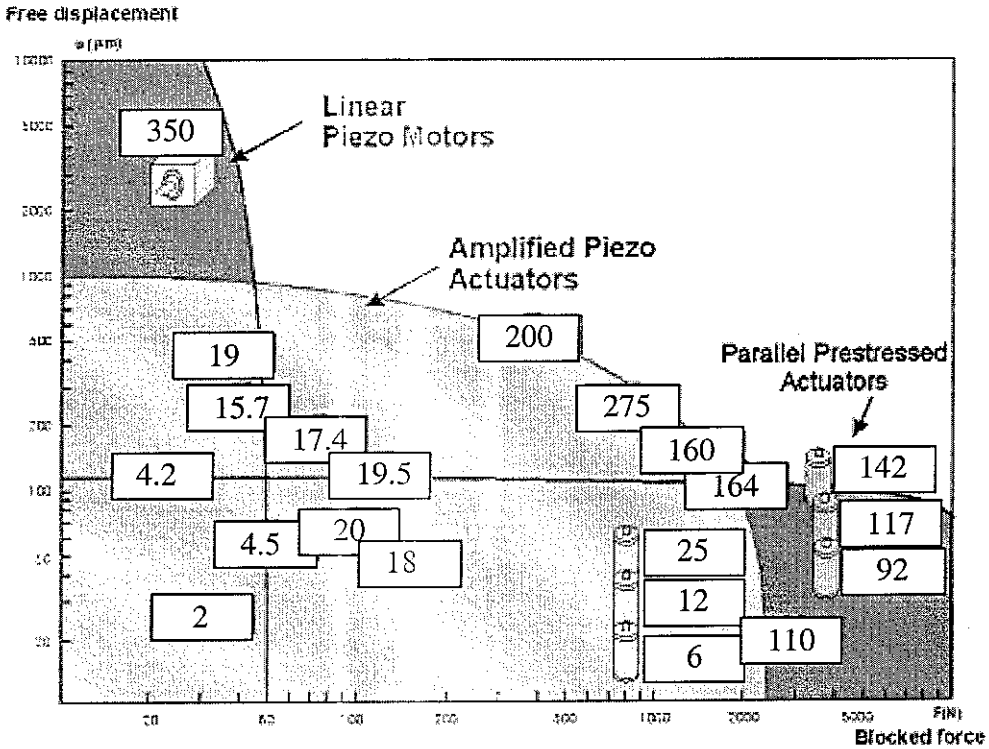

Figure 1.2: *Free displacement in µm and blocked force in N for various piezoelectric actuator technologies, weight in g*

There is a large range of electromagnetic actuators [19, 20]. Since an additional gear for the rotary-linear transformation adds weight, increases the time response and might introduce backlash and non-linear friction via the stick-slip effect only direct linear actuators are considered. Linear electromagnetic actuators [21] consist of a current carrying coil, a (permanent) magnet ('stator') and/or an additional moving part ('rotor'). In voice coil motors (VCM), also called electrodynamic actuators, the current carrying coil moves in a static magnetic field, whereas in linear motors an additional moving part moves in a constant magnetic field. Since an additional moving part is necessary for linear motors electrodynamic actuators can be designed with a smaller volume [13]. In electromagnetic actuators the magnetic field changes by displacing the magnet or coil, so that due to inherent non-linearity special control electronics are necessary [22, 23]. Applications of electromagnetic actuators for active vibration control can be found in [24], [25], [26] and [27]. The design of an electromagnetic miniature actuator is described in [28].

Figure 1.3 shows the blocked force-maximum free displacement characteristics and weight for various commercially available electrodynamic actuators each indicated by a dot '.' and the actuator weight in grams.

First a maximum force maximum stroke combination can be obtained with different actuator weights. Second for a given design, weight seems to increase with increasing force and to a smaller extend with increasing stroke. In order to obtain a certain actuation force there seems to be a minimum weight that is needed.

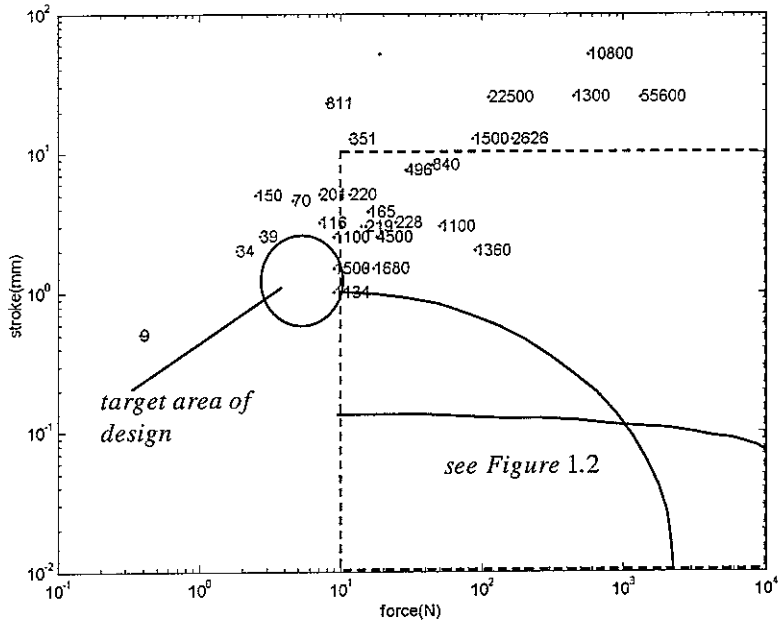

Figure 1.3: *Stroke in mm and blocked force in N for various commercially available electrodynamic actuators indicated by a dot '.' and weight in g* [29] - [35].

In order to compare Figure 1.3 and Figure 1.2 the range of Figure 1.2 is indicated as a dashed line in Figure 1.3. Piezoelectric actuators can be used for high forces and small strokes in the lower right hand corner of the figure. Lightweight, electrodynamic actuators can be found in the upper left hand part of the figure for high strokes and low forces, but not for high forces. In particular there is the indicated target area of the design above 0.6mm stroke and 3N that is not reached by available lightweight piezoelectric or electrodynamic actuators lighter than about 50g. In a theoretical comparison of the static force-stroke characteristic of a piezoceramic positioning drive including transmission gears and an electromagnetic actuator at hydraulic valves, [36] found that dc magnets have a higher force starting at a positioning range of about 0.5mm. In practice this value is likely to be higher for electrodynamic actuators since it does not consider dynamic thermal aspects. Acoustic attenuation experiments at airplanes have shown that a lower number of electrodynamic point force actuators than distributed piezoelectric actuators are needed in order to insert the same power in the vibrating surfaces [10]. Hence a system of electrodynamic actuators might be lighter than a system of piezoelectric actuators with the same performance, although individual actuators are heavier. Moreover since the beginning of the 1990s, when some authors described electrodynamic actuators as not lightweight [37], the introduction of strong permanent magnet materials has allowed the design of powerful permanent magnet motors in many applications [38]. Figure 1.4 from [39] indicates that the introduction of new stronger permanent magnets is likely to continue in the future since the theoretical limit of the magnetic energy density in a material has not been reached yet. In parts of this study it is examined in how far the contrasting requirements low added mass, high stroke and high actuation force can be balanced in the design to obtain a lightweight, electrodynamic actuator with characteristics in the circular target area shown in Figure 1.3.

Although a number of parameters of linear electromagnetic actuator design can be taken from the rotary electromagnetic actuator design literature [40] an important value, the allowable

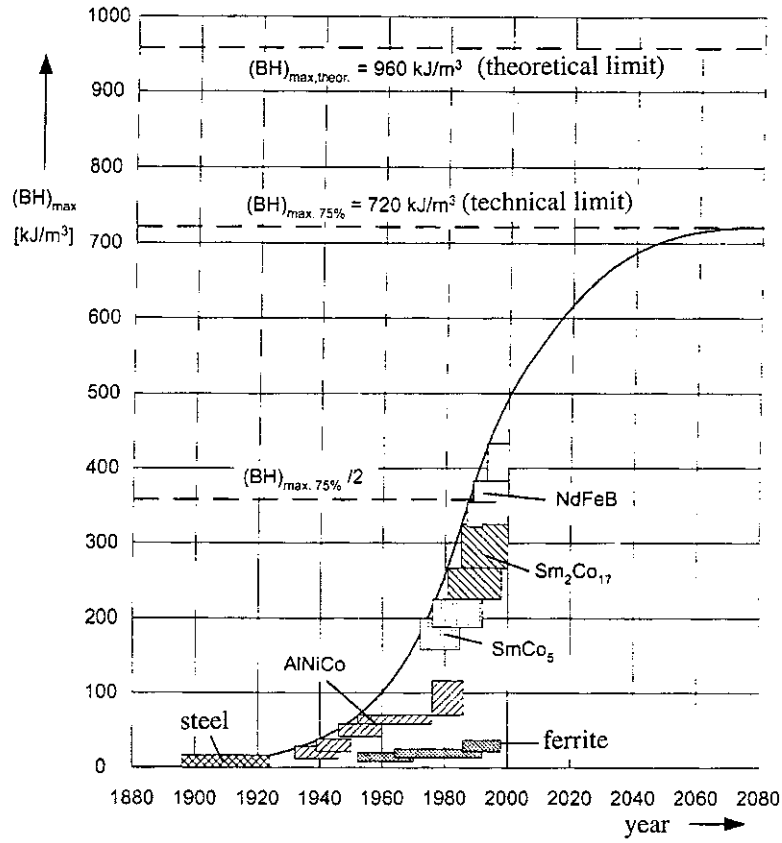

Figure 1.4: *Development potential of the $(BH)_{max}$ product of permanent magnet materials [39]*

coil current density, is usually based on past experience [41] and cannot easily be determined before having actually designed the actuator. An estimation for different actuator sizes based on a scaling factor is given by [42]. Similar problems arise when consulting the loudspeaker design literature since every loudspeaker designer seems to have its own design philosophy based on specific experience. A detailed summary of different aspects of this application of linear, electrodynamic actuators can be found in [43]. The design of the magnetic circuit is well explained for example by [44, 45]. A description of permanent magnet materials can be found in [38] [46]. Although a lumped self-inductance is a good representation of the electromagnetic behaviour of an electrodynamic actuator until a certain frequency [12] a more detailed model can include additional equivalent lumped parameter components [46] or more complicated eddy current models [47]. Details of the coil winding procedure are found in [48]. Including these models the coupled, dynamic behaviour of electrodynamic actuators can be simulated using either network models [49] or a detailed finite element analysis [50, 51 ,52]. Based on the model an optimisation can be carried out. Previous designs are presented in [35], [53]-[58] and typical parameters of electrodynamic actuator can be found in [59], [29]-[35].

An innovative design feature of electrodynamic, inertial actuator in order to fulfil requirements is adding internal damping using relative velocity feedback. As shown by [60, 61] internal damping does not only stabilize the inertial actuator [11], but it can then also be used for vibration reduction of the attached structure and enhance the effect of direct velocity feedback. For instance the relative velocity can be sensed and fed back using a self-sensing control scheme [12, 62]. Previous work [12] has shown first that for a self-sensing control

scheme the primary coil resistance has to be chosen in such a way as to balance power consumption and control robustness. Second the magnetic field in the air gap is to be chosen to balance sensitivity and control bandwidth. In order to avoid and facilitate balancing an explicit internal sensor i.e. a secondary coil already proposed by [63] is introduced in this study. Such an implementation has been already used in order to stabilize resonant sensors [64].

In this study the design procedure of an electrodynamic, inertial actuator for active vibration control of a lightweight panel used in [65] is presented. First requirements are outlined. Then the electromagnetic circuit is chosen and optimised using FEA. The mechanical design step includes the design of the suspension, the cover and the guide. In order to allow for self-sensing control and relative velocity feedback a sensing and a driving coil are designed based on the available space and electrical power requirements. The presentation of the manufacturing illustrates the assembly of the electrical and mechanical parts and highlights practical implementation challenges. In a final validation step measured parameters of the designed electrodynamic actuator for inertial actuation at lightweight panels are compared to predictions. The aim of the study is to show the feasibility of an electrodynamic, inertial, miniature actuator with internal sensor for active vibration control of lightweight structures.

The report is organised in five parts:

In Section 2 requirements for the electromagnetic circuit and the mechanical part of the inertial actuator for the application at a lightweight panel are described. Additionally some design criteria for self-sensing vibration control are given based on results in [12].

Section 3 gives an analytic description of the electromagnetic circuit in terms of the geometrical parameters of the chosen actuator concept. Based on this description the actuator force is maximised for a given electrical input power and different inertial masses. Linear analytical results are compared to results from a finite element analysis using a non-linear model of the electromagnetic circuit. A second optimisation of the actuation force based on a number of FEA allows the optimisation of the geometry of the electromagnetic circuit.

In Section 4 the mechanical design of the inertial actuator and the coil are described and a number of solutions for each of the mechanical functions suspension, guide and cover are proposed. The dynamics of the chosen combination of solutions is investigated using a dynamical FEA.

Section 5 presents the manufacturing process and the challenges encountered herein. The state of the actuator is visualized at different manufacturing steps.

Finally in Section 6 actuator parameters are identified using selected FRF measurements and the maximum operating range is determined experimentally. Necessary electronic circuits are illustrated.

2. REQUIREMENTS

The electrodynamic actuator should be lightweight, but still transmit a sufficient force F_t on the structure. The actuator force F_a generated by the electromagnetic circuit might limit the transmitted force. The actuator force is limited by the strength of the magnetic field in which a coil is immersed, by the length of the coil wire which is immersed in the magnetic field and by the current that can be input to the actuator. At a given electrical power input which depends on thermal losses that can only be precisely determined by ex-post measurements the limits depend on the chosen materials and geometric parameters that are closely linked to the total mass of the actuator to be minimized. Moreover since the actuator is used as an inertial actuator with a reaction mass the maximum transmitted force is given by the reaction mass of the actuator and its stroke that depends on the required control bandwidth. These two parameters determine the actuator geometry and the minimum actuator mass. Other constraints are given by material properties such as the maximum magnetic field saturation for the electromagnetic circuit and the yield strength for the mechanical system. Protection from the environment and manufacturing issues also constitute important constraints on the design.

2.1 Electrodynamic requirements

Limits for the electromagnetic circuit mainly arise from the available material. The permanent magnet should generate a high magnetic B-field that should not degrade largely with temperature. Since heating is related to power losses in the coil wire the material characteristics of the coil wire and heat evacuation interfere. Moreover using a permanent magnet demands special handling considerations.

The demagnetisation characteristics of common permanent magnet material are shown in Figure 2.1.1 from [40].

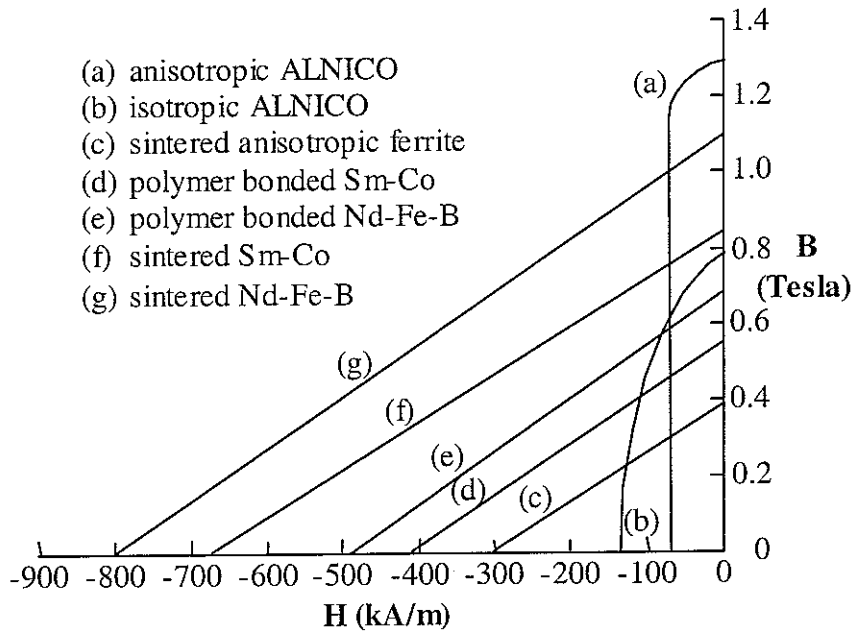

Figure 2.1.1: *Typical B/H curves in the demagnetisation region [40]*

Since temperature robustness and demagnetisation field due to high electrical currents play a role the knee in the demagnetisation curve should be at negative values for B since it moves to the right for higher temperatures [44]. Hence materials (a) and (b) should not be used. NdFeB magnets turn out to be most advantageous because of their high *B*-field.

Figure 2.1.2 shows the saturation curve and maximum saturation values for different ferromagnetic materials [66] that could be used to close the magnetic circuit. Although saturation differences converge for high magnetic fields rather steel or even steel alloys optimised for magnetic circuits (e.g. [67]) instead of cast iron should be used.

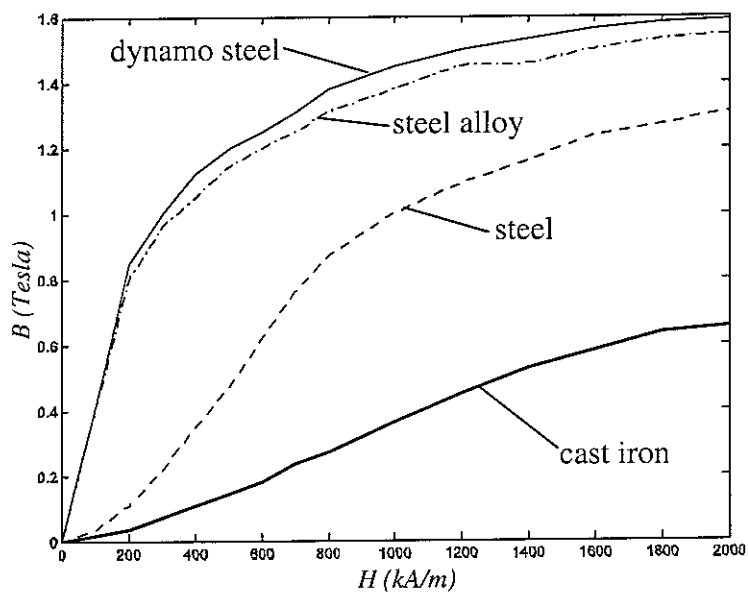

Figure 2.1.2: *Magnetisation characteristics of different ferromaterials [66]*

Moreover the chosen magnetic material should be used close to its saturation point. Hence the magnetic circuit should be designed in such a way that a) the saturation field at the inner side of the air gap: B_{gi}=1.2T, b) the saturation field at the outer side of the air gap: B_{go}=1T, c) the saturation field in the outer iron B_w=1.2T and that c) leakage is minimized. In order to reduce the direct, short circuit, of the magnetic field from the upper part of the magnet to its lower part through air without passing via the magnetic circuit the height of the permanent magnet b should be much greater than the air gap length s e.g. $b>3s$.

Due to the chosen material of the permanent magnet the actuator temperature should not increase beyond about 80°C. Since common coil insulation material may withstand [68] higher temperature up to 155°C the heating of the permanent magnet rather is the high temperature limit and not the degradation of the wire insulation.

This gives an upper limit on the dissipated, electrical power and hence on the actuator electrical, input power. A lower limit is given by the necessary power for active vibration control that, following [69], is independent from the degree of active damping for broadband excitation. For example for active vibration control of a 0.5m^2 plate using piezoelectric actuators [70] gives a required power of 5W.

The dissipation in the electrical circuit also depends on the specific resistivity of the coil wire material. Due to their availability and high conductivity either enamelled copper or aluminium wire should be used. For simplicity and manufacturability reasons the coil should be wound using common wire winding methods.

Furthermore the air gap and the permanent magnet have to be protected from tiny metal chips that, when stuck together in a large quantity, may block the actuator movement or damage the wire. A coating on the permanent magnet does protect it from scratches due to moving chips and adds corrosion resistance. A better protection is provided by a tight cover either just of the air gap or even better of the whole actuator as discussed in Section 4.3. The cover should be lightweight, not ferromagnetic and stiff enough so that resonance frequencies lie outside of the control bandwidth. Aluminium and its alloys are materials that fulfil these requirements.

The actuator coil should be driven so that the influence of the magnetic circuit on the input signal is minimized. Therefore a current drive amplifier with a large bandwidth should be used in order to drive a primary driving coil. An additional, secondary coil can be used to add damping to the actuator movement at resonance or to measure the relative vibration velocity.

2.2 Inertial actuator requirements

In addition to electrodynamic requirements that are related to the force generation mechanism special requirements follow from the use of the actuator as an inertial device i.e. as an actuator that generates a force on a mechanical structure relative to a defined moving reaction mass. There is a special relation between the generated actuation force and the force transmitted on the mechanical structure that gives a lower limit on the actuator bandwidth. An upper limit is given by internal actuator resonance frequencies and is to be balanced with application bandwidth requirements. Since the actuator should be usable for active structural acoustic control (ASAC) [9] of lightweight, mechanical structures there are also tough weight requirements in order to compete with piezoelectric actuators.

2.2.1 Transmitted force

An inertial actuator generates a force F_a on a mechanical structure and reacts against a mass M that is connected to the mechanical structure by a spring K also including damping D as shown in Figure 1.1. When the mass vibrates harmonically at a vibration velocity $\dot{x}$ the total transmitted force on the structure becomes $F_t = j\omega M\dot{x}$ or

$$\frac{F_t}{F_a} = \frac{j\omega M}{j\omega M + K/j\omega + D} \tag{2.1}$$

if $\left(Mj\omega + K/j\omega + D\right)\dot{x} = F_a$. Figure 2.2.1 shows the actuator force as function of the transmitted force on the plate without considering vibration feedback via the plate as is described by equation (2.1) for parameters compiled in Table 2.1. Below a resonance peak at $\omega_1 = \sqrt{K/M}$ the actuator does not transmit a significant force on the structure, whereas for higher frequencies the transmitted force F_t tends to the generated actuator force F_a. Hence the natural frequency of the actuator mass on a spring constitutes a lower frequency limit.

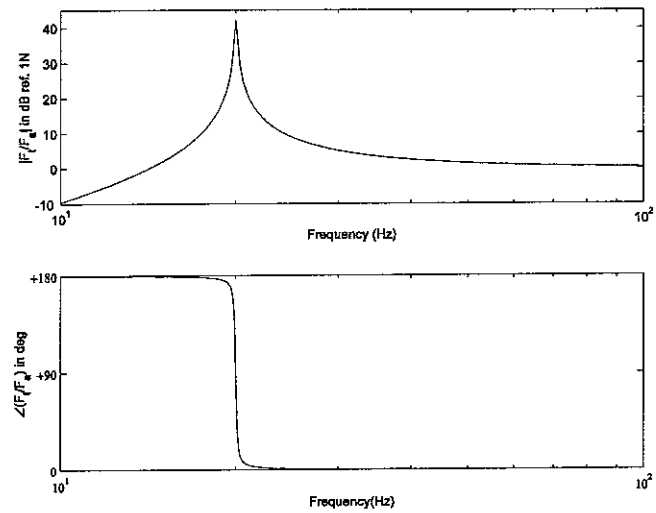

Figure 2.2.1: Bode plot of the frequency response function (FRF) between the actuation force F_a and the transmitted force F_t

In order to obtain an estimate of the necessary forces at the application of noise reduction at a lightweight panel, the panel is excited by a shaker with a white noise force with bandwidth 100 Hz that is measured by an accelerometer located at the connection point of the shaker with the panel and the radiated sound pressure level (SPL) is measured with a microphone at a distance of about 0.5m from the plate. Figure 2.2.2 shows a plot of the measured SPL versus the excitation force. When assuming linearity and especially that a similar force is needed to suppress radiated sound as it is to generate the sound an actuator force of 4N is necessary to control a radiated broadband sound of about 85 dB SPL.

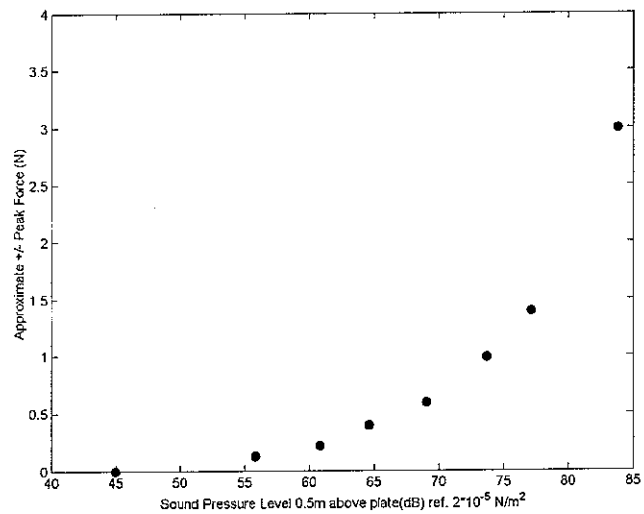

Figure 2.2.2: *Measured excitation force as function of the SPL measured 0.5m above a clamped 0.414m x 0.314m panel at white noise excitation 0 to 100 Hz*

Table 2.1: *Parameter values used for simulations in Figure 2.2.1*

Parameter	Value	Description
K	315.83 N/m	Suspension stiffness
D	0.0199Ns/m	Damping coefficient
M	0.02 kg	Inertial mass

2.2.2 Lower frequency bandwidth limit

Section 2.2.1 illustrated the lower frequency limit. The maximum allowable lower frequency limit is determined by the application. Figure 2.2.3 shows the measured FRF between an excitation force and the vibration velocity at the same location of a simply supported 0.414m x 0.314m x 0.001m plate. The natural frequency of the first mode ω_{11} appears at about 55 Hz which is the lower limit of the application bandwidth. Simulations for an ideally clamped beam indicate a resonance frequency of the first mode at about 70Hz. In order to be able to control this structural resonance frequency following [11] the actuator resonance frequency should be as low as possible or as highly damped as possible. Choosing an actuator frequency at one third to one fifth of the structural frequency seems to be reasonably low so that a sufficiently damped actuator with a resonance frequency below 20Hz should be able to control plate modes.

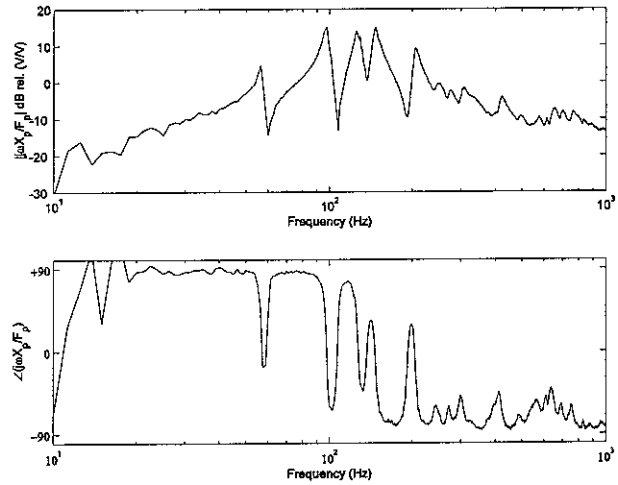

Figure 2.2.3: *Measured FRF between primary excitation force and collocated velocity of a 0.414x0.314x0.001m^3 aluminium plate*

2.2.3 Upper frequency bandwidth limit

On the one hand the upper frequency bandwidth limit is given by the application. The usually considered ASAC bandwidth lies below 2 kHz (see literature summary in [12]). In particular low frequency active noise control is especially important since high frequency noise control can be coped with using passive materials that have good absorption characteristics at higher frequencies [1]. Additionally a large amount and weight of absorption material is necessary because of the large wavelength at lower frequencies [71]. A control bandwidth of up to 1kHz is considered to be sufficient for this application. On the other hand internal actuator resonance frequencies could reduce the usable bandwidth considerably. Hence the suspension of the inertial actuator mass M, the cover or any other mechanical component should not introduce additional resonance frequencies in the frequency range until 1kHz or components with a resonance frequency in this frequency range should have a small weight. Components that do not lie directly in the load path are not very critical. Together with the lower frequency limit this requirement implies low suspension stiffness in vertical direction K_{ver}, but a high stiffness in all other directions especially in the horizontal direction K_{hor}, for bending and torsion. In particular $(K_{ver}/M)^{0.5}=\omega_1<<\omega_{11}$ and $(K_{hor}/M)^{0.5}>2\pi 2000$Hz. The coil should be linked to the structure as directly as possible in order to prevent excitation of additional

resonances. For physical robustness reasons and since the actuator might be used in rough vibration environment the suspension should be simple so that an additional positioning sensor and electronics for e.g. electromagnetic suspension should not be used since these electronics may also limit the bandwidth [69]. In order to save weight and space a compact design maybe with integration of suspension and cover i.e. a membrane is desired.

2.2.4 Maximum weight

At the considered application, a lightweight, flexible plate, four electrodynamic actuators should replace 16 piezoelectric moment actuators with a weight of about 16x2.4g=38.4g. Additionally 16 point velocity sensors are used with a weight of about 16*2g=32g. The total weight of 70.4g for the whole systems means that a competitive system of four electrodynamic actuators with integrated sensor should not exceed a weight of about 70.4g/4=17.6g or about 20g per electrodynamic actuator. Theoretically the main component adding weight is the reaction mass so that in the following theoretical considerations the weight of auxiliary parts is neglected. The approximate volume is not severely limited with requirements in the region of 0.03 x 0.03 x 0.03 m^3 so that the actuator is easily applicable in a laboratory environment.

2.2.5 Maximum stroke

Tougher requirements are given for the maximum stroke d since it directly determines the maximum transmissible force on the structure via $F_{tmax}=M\omega^2 d$. Moreover Equation (2.1) indicates that the generated actuation force F_a limits the transmitted force at frequencies beyond the actuator resonance frequency ω_1. Hence when assuming that the actuator is in stroke saturation at the actuator resonance frequency the plot in Figure 2.2.4 represents the maximum transmitted force as a function of frequency. From Figure 2.2.4 it is obvious that for an optimum actuator design the lower frequency bandwidth limit should be at the knee of the curve at the so called (saturation) break frequency ω_b [72]. The break frequency ω_b is given by $\omega_b = \sqrt{F_a/(Md)}$ and should be equal to the first mode resonance frequency of the plate $\omega_{11}=\omega_b$. With F_a=4N from Section 2.2.1, ω_{11}=55Hz or 70Hz from Section 2.2.2, M=0.02kg from Section 2.2.3 d=0.0017m or 0.001m. Hence a maximum stroke of about 1mm with a safety margin up to 2mm should be sufficient for this application.

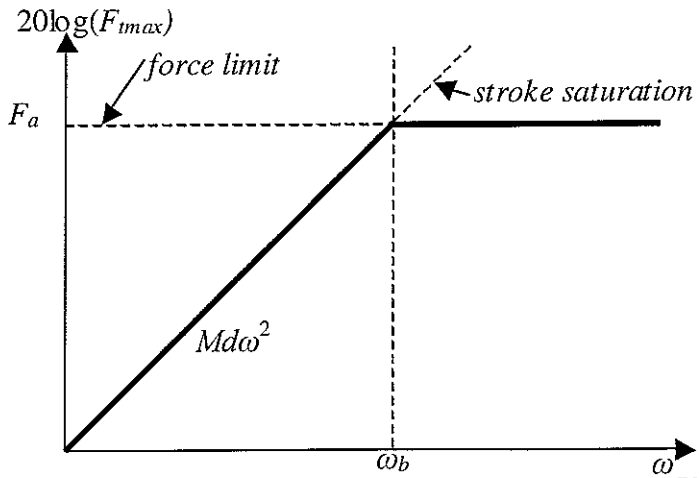

Figure 2.2.4: *Force Saturation Curve, +/- d maximum stroke [72]*

2.3 Requirements for self-sensing control

As an option the actuator should allow self-sensing vibration damping in order to be able to compare it to control using the internal velocity sensor. In [12] trade-offs between first control bandwidth and amplitude and second power dissipation and robustness are identified in a self-sensing vibration control system. Appropriate values are to be chosen for the actuator design in order to allow sensible application of a self-sensing vibration control system.

Trade-off 1: inductance - transducer coefficient

Figure 2.3.1 depicts a bode plot of the FRF between the actuator driving voltage and the vibration velocity at an electrodynamic shaker from [12]. Measurements are represented by a solid line and simulations by a dashed line. Damping is aimed at the resonance frequency at 100Hz that shows the typical 180° phase shift. An additional phase shift of -90° is visible in the frequency range between about 200 Hz and 6 kHz due to the self-inductance of the coil. The third characteristic phase shift of –180° due to the accelerometer resonance frequency is of no further interest.

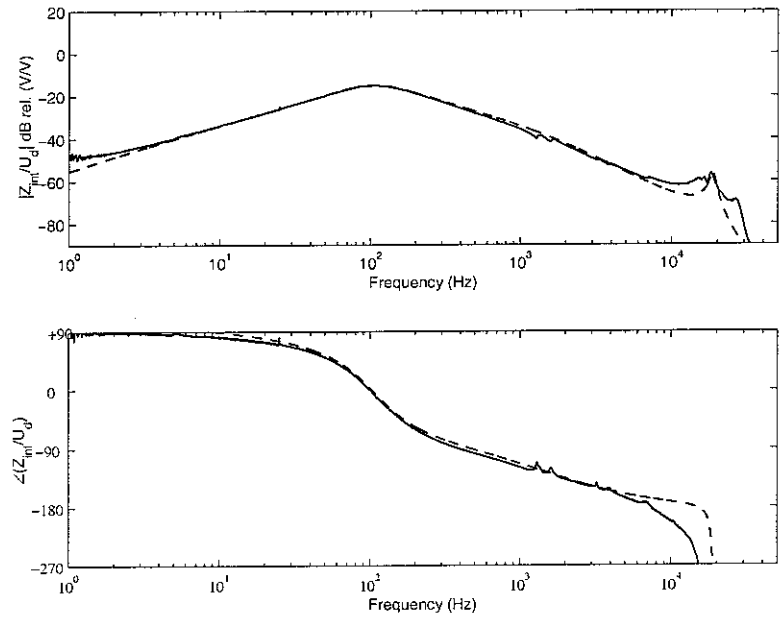

Figure 2.3.1: *Bode plot of the measured (solid line) and simulated (dotted line) FRF from the source voltage U_d to the measured velocity $\dot{X}_r$ [12]*

The frequency range in which damping can be added using self-sensing control is increased when the -90° phase shift is moved towards higher frequencies. This is equivalent to reducing the inductance value L. The value of the transducer coefficient Ψ determines whether critical damping is possible. Following [62] critical damping is possible for single degree of freedom (SDOF) system if $L < \frac{\Psi^2}{M\omega_d^2}$ where $\omega_d = \omega_1\sqrt{1-\xi^2}$ is the damped natural frequency with the non-dimensional damping ratio $\xi = D/\left(2\sqrt{KM}\right)$. On the one hand the self-inductance for a

solenoidal coil of height h, radius r with N turns and relative permeability of the material inside the coil μ_r is given by $L = N^2 \pi r^2 \mu_r / h$ [73]. On the other hand the transducer coefficient for a solenoidal coil immersed in a magnetic field of strength B_g is $\Psi = B_g 2\pi r N$ so that for critical damping $\mu_r < \frac{h\pi 4 B_g^2}{M \omega_d^2}$. In real systems, however, in order to be able to obtain a high B_g materials in the magnetic circuit with a high μ_r are to be chosen if not a strong permanent magnet is available so that smaller μ_r values are acceptable. This trade-off in the choice of the magnetic circuit also underlines the importance of choosing strong permanent magnets, a low mass and a low inertial resonance frequency ω_1. Additionally a tall coil is advantageous.

Trade-off 2: power consumption - robustness

In order to reduce electrical power dissipation the coil resistance should be small. But simulations of the relevant root locus plot depicted in Figure 2.3.2 from [12] indicate that for a small resistance R value also small positive current feedback gains G already lead to instability. Precision power resistors hence are needed in order to allow a robust control circuit. Small resistor variations due to temperature changes might destabilize the control scheme if small resistor values are chosen. A trade-off could possibly be avoided using an adaptive control algorithm so that small driving coil resistance values are acceptable.

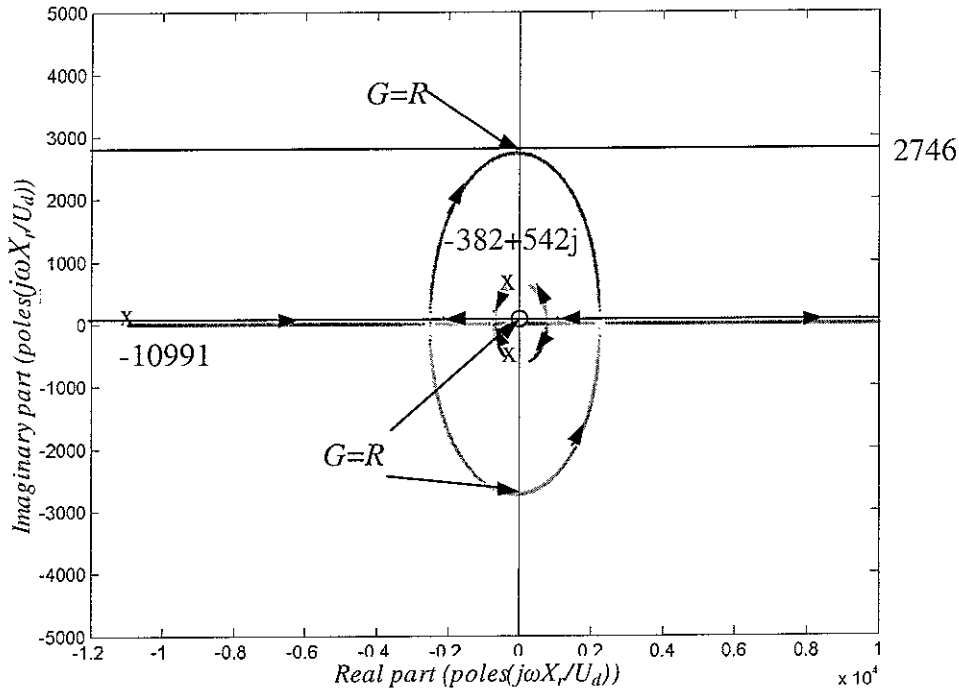

Figure 2.3.2: *Root locus plot of the FRF disturbance voltage U_d to measured velocity $\dot{X}_r$ for positive current feedback gains G = 1 to 2000; x open loop poles; zoom at origin [12]*

3. ELECTRODYNAMIC DESIGN PARAMETERS

A number of magnetic circuit configurations have been proposed for electrodynamic actuators. A preliminary evaluation already gives hints about their advantages and drawbacks. Since material and machining costs are not a criterion, assembly and total mass considerations determine the preliminary design choice. A maximisation of the actuator force as function of the actuator mass is aimed at using relevant equations and approximations. Some magnetic circuit design approaches are based on maximizing the magnetic field in the air gap without regarding the possible amount of wiring in the air gap. In this section it is shown that this design approach is not interesting if a constant power input is considered since there is a trade-off between a strong magnetic field in the air gap and the possible amount of wires. However, the power input cannot be determined beforehand because a lot of thermal variables are not known; it can only be determined by measurements at the actual system. Hence, a large uncertainty in all the following considerations remains. A more detailed magnetic circuit design and geometry optimisation is carried out using an electromagnetic FEA.

From the seven general options depicted in Figure 3.1 for a linear, electrodynamic actuator only option 6 is considered since it seems to allow a high force and a lightweight design. Option 1 is able to generate a strong permanent magnetic field, but a rather high magnetic volume is needed and high leakage is anticipated since permanent magnets may not concentrate the magnetic field generated by other permanent magnets. They behave like air with a permeability of 1 relative to additional permanent magnets in the circuit. This option is also not considered because of the potentially difficult assembly and the attraction of small particles to the magnets. In comparison to option 1 option 2 should have less leakage and is

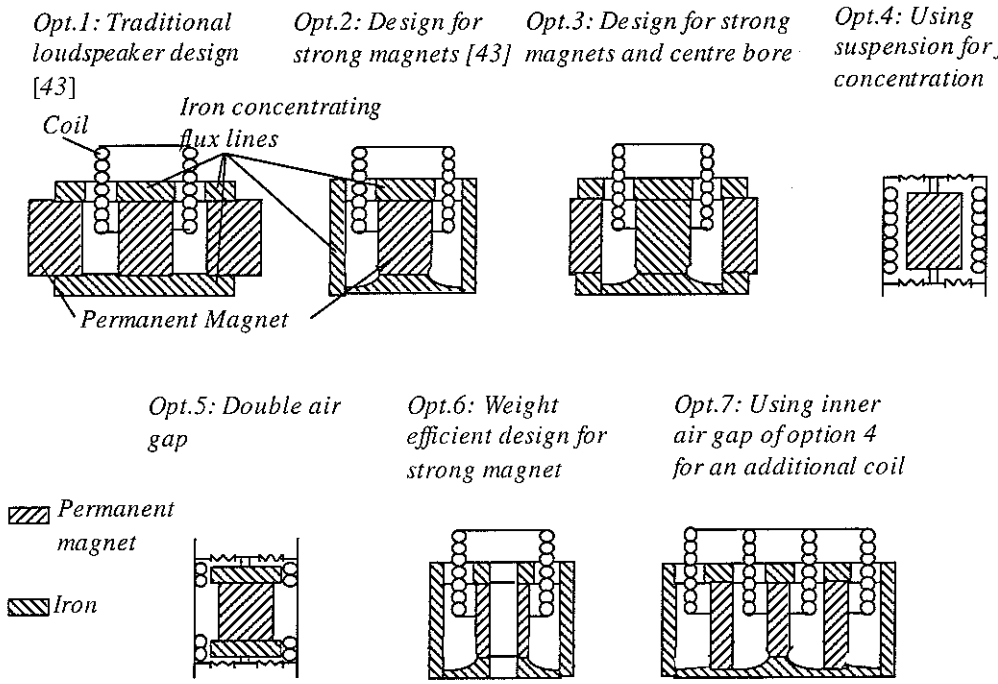

Figure 3.1: *Different options for the geometry of the magnetic circuit*

easier to assemble. However, weight is still not minimized and a special guide is to be foreseen if the assembly is to move in vertical direction. At option 3 a permanent magnet at the outer ring leads to high leakage. This option is interesting if the space at the inner part of the magnetic circuit should be used for other functionalities. In comparison to option 2 a

larger permanent magnet volume is possible, since its diameter is increased. Relative to option 6 it is only advantageous if a hole in the permanent magnet reduces the generated magnetic field significantly. It is assumed that a small hole does not reduce the field significantly so that option 6 is preferred relative to option 3. Option 4 has high leakage because the magnetic field is not concentrated in the coil, but in the suspension and in the cover that is used as the outer iron. Option 5 has less leakage than option 4 since additional iron disks concentrate the field. The coil is also only used where the magnetic field is highly concentrated and the cover is additionally used as an outer iron yoke leading to further weight reduction. Nevertheless design 5 has high leakage and the double air gap just seems to be interesting for rather tall permanent magnets. The effect of additional magnetic sources is difficult to evaluate in option 7. As mentioned before they should behave as air for the magnetic field generated by other permanent magnets. Hence high leakage is predicted. Moreover unequal saturation leads to different flux in the inner and outer air gaps. Because of the complicated assembly option 7 also is not first choice. Finally Option 6 allows a bigger coil diameter at a given weight and hence more wire in the same air gap length provided the hole does not reduce the field generation of a permanent magnet at constant volume. Since a lightweight actuator with a high force, that uses a strong permanent magnet, is demanded option 6 is chosen for further investigation.

3.1 Governing equations of the electrodynamic system

The equilibrium in a magnetic circuit is determined by the characteristics of the permanent magnet and the geometric properties of the magnetically connected parts. Design options 2 and 6 are parameterised using the geometric parameters depicted in Figure 3.1.1. For option 2 the diameter of the hole in the permanent magnet A_i=0. A is the outer diameter of the permanent magnet of height b. h_g is the height of the inner iron, h_{gl} is the height of the outer iron yoke and D_o is its outer diameter. Its inner diameter is determined by the width of the air gap s and the thickness t of the protrusion. These parameters determine the load line of the magnetic B-field and magnetic H-field plot in Figure 3.1.2. The equilibrium B-field in the magnetic circuit is determined by the value at the intersection of the load line with the

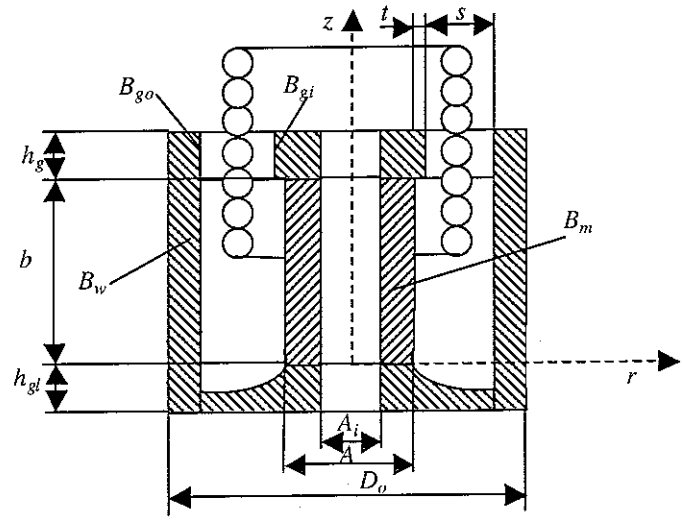

Figure 3.1.1: *Electrodynamic shaker design using a strong permanent magnet, options 2 & 6*

demagnetisation curve of the used permanent magnet from Section 2.1. At constant power input the actuation force depends on the B-field that is given at certain points of the magnetic circuit and the wire geometry in the air gap. The actuator mass is also a function of geometric

parameters so that the relationship between actuator force and mass can be determined for a wide range of geometric parameters. Based on this plot a parameter combination compatible with the actuator force (F_a>4N) and mass (m<0.02kg) requirements is chosen.

3.1.1 Equations of the electromagnetic circuit

Following Figure 2.1.1 the magnetic B-field - H-field characteristics of a Nd-Fe-B permanent magnet is described by

$$B_m = B_r - \frac{B_r}{H_l} H_m \tag{3.1}$$

with B_r and H_l as shown in Figure 3.1.2 and depending on the actually chosen alloy. The angle α of the load curve of the added magnetic circuit relative to the H-axis is given by

$$\tan(\alpha) = \frac{H_{lo}}{B_{lo}} = \frac{qA_m s}{pA_g b\mu_0} \tag{3.2}$$

where the second part results from the application of Ampere's circuit law to the permanent magnet and the air gap. A_m is the cross section of the permanent magnet, b its height, A_g the cross section of the air gap and s its length. q and p are unknown loss coefficients associated to the shape and configuration of air gap and permanent magnet. They are determined by experiments, experience or they can be avoided using a FEA as presented in Section 3.2. Expressing these general parameters in terms of the parameters in Figure 3.1.1 and using Equations (3.1) and (3.2) gives the magnetic field B_m generated by the permanent magnet at the equilibrium

$$B_m = \frac{B_r}{1 + \dfrac{B_r q\left(A^2 - A_i^2\right) s}{4H_l p h_g (A + 2t) b\mu_0}}. \tag{3.3}$$

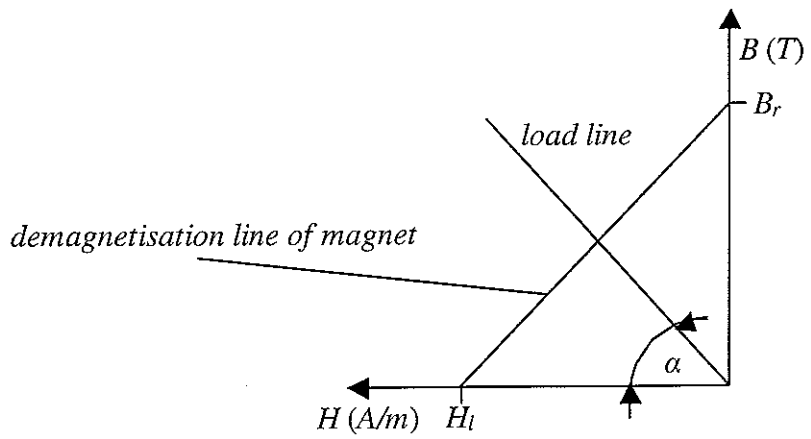

Figure 3.1.2: *Equilibrium of the magnetic circuit between the magnet and the closing elements modelled by the load line [44]*

Assuming that the magnetic flux Φ is constant in the whole circuit and homogeneous in each individual part of the actuator as illustrated in Figure 3.1.1 the magnetic B-field in the outer iron B_w, at the outer diameter of the air gap B_{go}, in the permanent magnet B_m and at the inner diameter of the air gap B_{gi} are related via

$$\Phi = \frac{B_w \pi \left(D_o^2 - \left(A+2t+2s\right)^2\right)}{4} = \frac{B_m \pi \left(A^2 - A_i^2\right)}{4} = B_{go} h_g \pi \left(A+2t+2s\right) = B_{gi} h_g \pi \left(A+2t\right) \quad (3.4)$$

where h_g is the height of the air gap. From Equation (3.4) the outer iron diameter becomes

$$D_o = \sqrt{B_m / B_w \left(A^2 - A_i^2\right) + \left(A+2t+2s\right)^2} \quad (3.5)$$

and the maximum allowable air gap is

$$s_{max} = 0.5\left(B_{gi}/B_{go}\left(A+2t\right) - A - 2t\right) \quad (3.6)$$

in order to guarantee the strength of the magnetic field B_{gi} and B_{go} in the air gap. Moreover the lower part of the actuator iron should have the same cross section as the outer wall in order to allow the same magnetic B-field provided the same magnetic flux goes through the cross section so that the wall thickness of the lower actuator iron should be

$$h_{gl} = \left(D_o^2 - \left(A+2s+2t\right)^2\right) / 4A. \quad (3.7)$$

Since no further assumptions are made regarding the magnetic B-field in the air gap for simplicity a linear distribution illustrated in Figure 3.1.3 and described by

$$B_g = \frac{B_{gi}\left(A+2t\right)}{A+2t+s} = B_m \frac{A^2 - A_i^2}{4h_g\left(A+2t+s\right)} \quad (3.8)$$

is assumed. A FEA in Section 3.3 allows a more detailed investigation of this assumption.

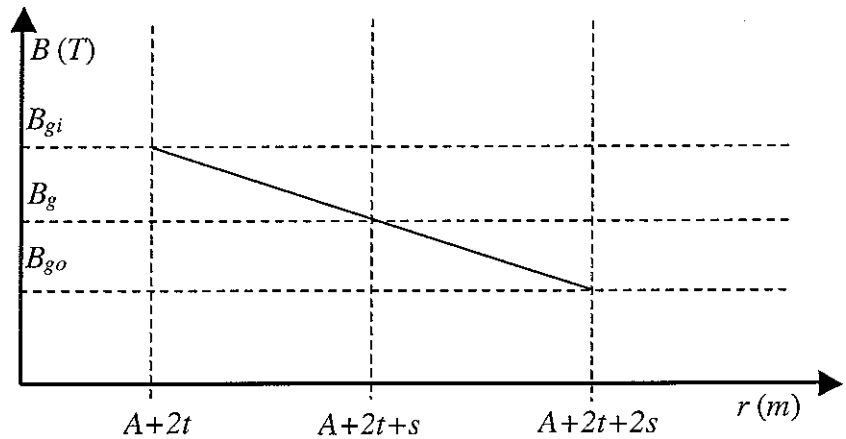

Figure 3.1.3: *Assumption of magnetic field in air gap*

Hence the magnetic field in the air gap B_g is given by Equation (3.8) together with Equation (3.3) as a function of the actuator geometric parameters and material properties of the permanent magnet if the magnetic fields B_{gi} and B_{go} do not saturate. If

$$B_{go} = \frac{\left(A^2 - A_i^2\right)B_r\left(H_l p\pi h_g\left(A+2t\right)B\mu_0\right)}{4h_g\left(A+2s+2t\right)\left(H_l p\pi h_g\left(A+2t\right)B\mu_0 + B_r qs\left(A^2 - A_i^2\right)\pi/4\right)} \geq B_{gosat} \quad (3.9)$$

or

$$B_{gi} = \frac{\left(A^2 - A_i^2\right)B_r\left(H_l p\pi h_g\left(A+2t\right)B\mu_0\right)}{4h_g\left(A+2t\right)\left(H_l p\pi h_g\left(A+2t\right)B\mu_0 + B_r qs\left(A^2 - A_i^2\right)\pi/4\right)} \geq B_{gisat} \quad (3.10)$$

the magnetic field saturates in the iron and then the saturated values B_{gosat}=1Tesla and B_{gisat}=1.2Tesla are taken to determine the actuator force as is presented in the next Section 3.1.2. Additionally the demagnetisation field

$$H_{dem} = \sqrt{\frac{P}{\rho_{wi}}}h_g \frac{\sqrt{\dfrac{s}{2F_{\max}m/\omega_b^2 + h_g}}}{\sqrt{\pi\left(A+2t+s\right)}} + \frac{H_l B_r q\pi\left(A^2 - A_i^2\right)s}{4\left(H_l p h_g\left(A+2t\right)\pi B\mu_0 + B_r q\pi\left(A^2 - A_i^2\right)s/4\right)} \quad (3.11)$$

due to an applied current at electrical input power P is determined and should be smaller than H_l so that the permanent magnet is not demagnetised. Another evaluation criterion for the magnetic circuit is the magnetic energy product $H_m B_m$

$$H_m B_m = \left(\frac{B_r p h_g\left(A+2t\right)\pi B\mu_0}{p h_g\left(A+2t\right)\pi B\mu_0 + B_r / H_l q\pi s\left(A^2 - A_i^2\right)/4}\right)^2 \frac{q\pi s\left(A^2 - A_i^2\right)/4}{p h_g\left(A+2t\right)\pi B\mu_0} \quad (3.12)$$

at the equilibrium point. It should be close to the maximum value of the magnetic material e.g. HB_{max}=300kJ for NdFeB from [40].

3.1.2 Non-linear cost function and constraints

The actuation force to be maximised at constant power input P is given by [82] to

$$F_a = B_g I l_{cg} \quad (3.13)$$

where I is the coil current and l_{cg} is the length of the coil wire in the air gap. The dissipated electric power at low frequencies is

$$P = I^2 R \quad (3.14)$$

when the inductance value is neglected and R is the coil resistance. The latter one is given by

$$R = \frac{\rho_{wi} l_c}{S} = \frac{\rho_{wi} l_c l_{cg}}{V_{cg}} \tag{3.15}$$

where ρ_{wi} is the specific resistivity of the wire, l_c is the length of the coil and S is the cross section of the coil wire. The latter is given by the ratio of the volume of the coil wire V_{cg} and the length of the coil wire in the gap l_{cg}. Equations (3.14) and (3.15) result in

$I = \sqrt{P}\sqrt{V_{cg}/\left(\rho_{wi} l_c l_{cg}\right)}$ and together with (3.13)

$$F_a = B_g \left(\frac{P}{\rho_{wi}}\right)^{\frac{1}{2}} \left(\frac{l_{cg}}{l_c}\right)^{\frac{1}{2}} \left(V_{cg}\right)^{\frac{1}{2}} \tag{3.16}$$

where B_g is given by Equations (3.3) and (3.8). The coil geometry with n windings in radial r-direction is approximated by an intermediate coil of wire diameter d_w in the centre of the air gap that has N windings in vertical z-direction whereof N_g windings are in the air gap. Since for weight reduction the coil height h_c is chosen to be bigger than the gap height in a so called long coil configuration the height of the coil in the air gap is approximately given by the air gap height h_g. Then the length of the coil and its height in the air gap are

$$l_{cg}=\pi(A+2t+s)N_g n \text{ and } h_g=d_w N_g \tag{3.17}$$

respectively and its total length and height are

$$l_c=\pi(A+2t+s)Nn+l_{con} \text{ and } h_c=d_w N=2d+h_g, \tag{3.18}$$

respectively, where the length of connection wire $l_{con}=0$ is neglected. The stroke maximum $d = F_a/\left(M\omega_b^2\right)$ is given by requirements in Section 2.2.5. The ratio of Equation (3.17) and (3.18) determines the term under the square root in Equation (3.16)

$$\frac{l_{cg}}{l_c} = \frac{N_g}{N} = \frac{h_g}{2d + h_g}. \tag{3.19}$$

When assuming that the hole air gap is filled with wire the volume of the wire in the air gap

$$V_{cg} = \sqrt{h_g \pi(A + 2t + s)s}\,. \tag{3.20}$$

Using Equations (3.3), (3.8), (3.19) and (3.20) in Equation (3.16) gives the actuator force

$$F_a = \frac{B_r H_l p h_g \left(A+2t\right) b \mu_0 \left(A^2 - A_i^2\right)}{4 H_l p h_g \left(A+2t\right) b \mu_0 + B_r q \left(A^2 - A_i^2\right)} s \sqrt{\frac{P}{\rho_{wi}}} \sqrt{\frac{1}{2F_a/\left(M\omega_b^2\right) + h_g}} \sqrt{\frac{\pi s}{\left(A+2t+s\right)}} \tag{3.21}$$

that can be considered as a non-linear cost function to be maximised. Requirements give constraints on this function. For example the iron saturates so that maximum values for the B-

field in the magnetic circuit are given by B_{gi}<=1.2T and B_{go}<=1T. Moreover the equilibrium should be in the second quadrant i.e. $0<H_m<H_l$ in order to prevent irreversible changes of the permanent magnet. Since leakage in this model is only considered by the constant coefficients p and q a further restriction should be placed on the air gap size. It is assumed that only for $s \le 0.5(1.2(A+2t)-A-2t)$ these coefficients are valid. Moreover the permanent magnet should be tall enough i.e. $b>3s$ so that directly closing the magnetic circuit via the surrounding air is reduced. The pertinence of these assumptions on the magnetic field and especially the parameters s, b, B_{gi}, B_{go} and B_w are checked during a finite element analysis that is presented in Section 3.3.

A further constraint is on the actuator mass

$$m = \rho_{mag}\pi\left(A^2 - A_i^2\right)b/4 + \rho_{fe}\left(\left((A+2t)^2 - A_i^2\right)\pi h_g/4 + \left(\pi(2t+2s)/4 + \left(A^2 - A_i^2\right)\pi/(16A) + \left(b+2h_g\right)\pi/4\right)\left(D_o^2 - (A+2t+2s)^2\right)\right)$$

that should not exceed m=0.02kg. ρ_{mag} is the mass density of the permanent magnet and ρ_{fe} is the mass density of the core material. The wire weight is neglected since only the weight of the moving reaction mass is of interest.

3.2 Optimal set of electrodynamic parameters

Due to the non-linear shape of the cost function linear optimisation procedures cannot be applied. Therefore the cost function is calculated respecting constraints for reasonable parameter sets in the parameter space permanent magnet diameter A, diameter of bore in permanent magnet A_i, gap height h_g, gap width s and height of permanent magnet b as in Figure 3.1.1 leading to forces in the order of 4 N and mass values in the order of 0.02 kg. Material properties and other assumed parameter values are compiled in Table 3.1. Copper is chosen as wire material since Equation (3.16) implies a low resistivity to be advantageous. Simulations using different permanent magnet materials underline the correct choice of the material of the permanent magnet. Figure 3.2.1 shows the calculated possible combinations of actuator force F_a and inertial actuator mass m for a selected parameter variation where A_i is chosen to be 0. Each point in the graph is a design point associated to a parameter set (A, A_i, h_g, s, b). The influence of a parameter on the design is determined by varying one parameter while fixing the others.

By increasing the air gap height h_g the design points shift to the right and upwards to higher forces and masses. Increasing the air gap length leads to design points shifted to the left to lower weights. Hence varying air gap height and air gap length has opposite effects and increasing air gap height or decreasing air gap length has a similar effect until a certain limit when the magnetic field close to the gap is no longer saturated. Increasing the height of the magnet b leads to an increase in weight and force due to the stronger magnetic field until the saturation point is reached. Beyond a certain magnet height the design requirement m<0.02 kg cannot be fulfilled. By increasing the outer diameter A design points move to increased weight whereas the opposite effect takes place with increasing inner diameter A_i.

Table 3.1: *Parameter values for simulations leading to Figures 3.2.1 and 3.2.2*

Parameter	Value	Unit	Description
B_{gi}	1.2	Tesla	Saturation B-field at inner side of air gap
B_{go}	1.2	Tesla	Saturation B-field at outer side of air gap
B_w	1.2	Tesla	Saturation B-field in wall of outer iron
t	0.0005	m	Overhang of inner iron into air gap
q	1.1	-	Leakage factor
p	2	-	Leakage factor
F_{max}	4	N	Required peak actuation force
ω_b	$2\pi 70$	rad/s	Saturation break frequency
P	1.25	W	Peak power input to actuator
ρ_{fe}	7800	kg/m^3	Mass density of iron
μ_0	$4\pi 10^{-7}$	-	Permeability of free space
ρ_{cu}	0.017	$m\Omega mm$	Electric resistivity of copper
ρ_{mcu}	8900	kg/m^3	Mass density of copper
ρ_{al}	0.0303	$m\Omega mm$	Electric resistivity of aluminium
ρ_{mal}	2700	kg/m^3	Mass density of aluminium
H_{l1}	800000	A/m	Maximum coercitive magnetic field intensity of Nd-Fe-B
B_{r1}	1	Tesla	Maximum remanent magnetic field of Nd-Fe-Be magnets
μ_{r1}	1.04	-	Recoil permeability of Nd-Fe-B magnets
ρ_{mag1}	7400	kg/m^3	Mass density of Nd-Fe-B magnets
H_{l2}	180000	A/m	Maximum coercitive magnetic field intensity of ferrites
B_{r2}	0.35	Tesla	Maximum remanent magnetic field of ferrites
μ_{r2}	1.05	-	Recoil permeability of ferrites
ρ_{mag2}	4900	kg/m^3	Mass density of ferrite
H_{l3}	40000	A/m	Maximum coercitive magnetic field intensity of AlNiCo
B_{r3}	1.35	Tesla	Maximum remanent magnetic field of AlNiCo
μ_{r3}	1.9	-	Recoil permeability of AlNiCo
ρ_{mag3}	4900	kg/m^3	Mass density of AlNiCo
H_{l4}	620000	A/m	Maximum coercitive magnetic field intensity of SmCoBM18
B_{r4}	0.85	Tesla	Maximum remanent magnetic field of SmCoBM18
μ_{r4}	1.09	-	Recoil permeability of SmCoBM18
ρ_{mag4}	8300	kg/m^3	Mass density of SmCoBM18
H_{l5}	940000	A/m	Maximum coercitive magnetic field intensity of NdFBBM38
B_{r5}	1.21	Tesla	Maximum remanent magnetic field of NdFBBM38
μ_{r5}	1.02	-	Recoil permeability of NdFBBM38
ρ_{mag5}	7400	kg/m^3	Mass density of NdFBBM38
A	10-20	mm	Diameter of permanent magnet
A_i	$<A$-4	mm	Diameter of centre hole in permanent magnet
hg	1-5	mm	Air gap height
s	1.5-s_{ma}	mm	Air gap width
b	3s-10	mm	Permanent magnet height

In general two major constraints are obvious for the given parameters outer diameter of permanent magnet A and height of the permanent magnet b: The first constraint is due to insufficient flux in the gap because of a high air gap width or height. The second constraint is

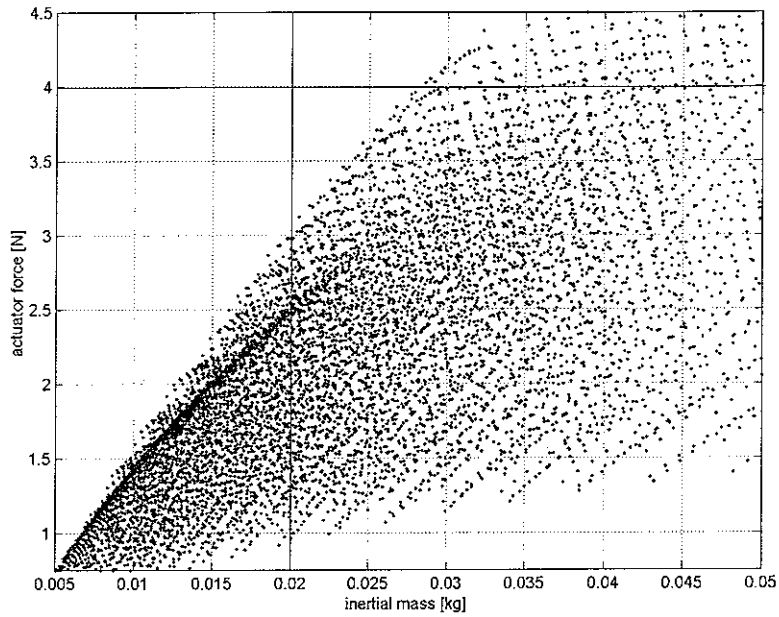

Figure 3.2.1: *Actuator force – inertial mass combinations for different parameter sets (A, A_i, h_g, s, b) following Figure 3.1.1. for A_i=0*

due to insufficient copper wire in the air gap because of a small air gap volume. Therefore optimal air gap values are obtained when the flux just saturates in the air gap and the maximum amount of copper is used. The limit to the left in the graph is given by the limited amount of copper wire in the air gap. The limit to the top is given by the magnetic field in the air gap that decreases when the air gap length s surpasses a maximum value. Using a stronger permanent magnet i.e. material the magnetic field saturation in the air gap can be pushed to higher air gap length s. Therefore in the design the strongest available magnetic material NdFeB is assumed. A way to increase the amount of copper wire in the air gap with all other parameters fixed is to increase the diameter A. Then introducing a bore with a diameter A_i, so that a ring magnet as in design option 6 is created, can compensate the increased weight. Figure 3.2.2 shows design points as a combination of actuator force F_a and actuator mass m when also varying the inner diameter A_i. In comparison to Figure 3.2.1 only small reduction in weight at a given force or increase in force at a given weight is observable. Moreover more uncertainties are added to the design as inner magnetic leakage and magnet strength might vary. Outer diameters A move to higher values.

From the graphs it is obvious that the requirements 4N and 0.02kg cannot be achieved simultaneously when using either of the designs with the assumed power input. As design option 6 with a hole might be more advantageous due to its heat properties, so that a higher input power could be used, a design with a smaller force, but fulfilling the weight requirement is chosen as one version to be investigated in detail by a FEA. The two other versions chosen from design option 2 and 6 give sufficient force, but they are 50% too heavy. They differ in their outer diameter that allow different kinds of suspension as demonstrated in Section 4. For this choice it is implicitly assumed that the force requirement is a stronger requirement than the weight requirement.

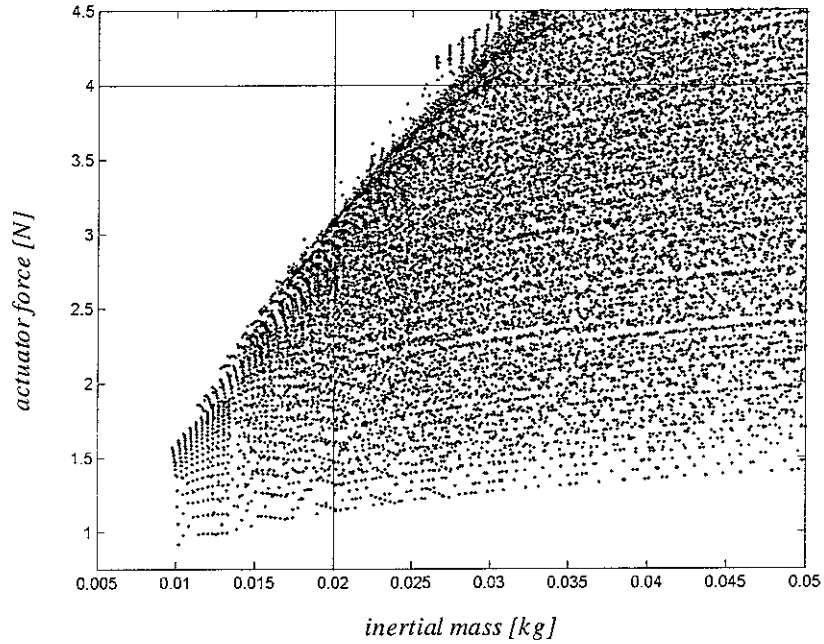

Figure 3.2.2: *Actuator force – inertial mass combinations for different parameter sets (A, A_i, h_g, s, b) as in Figure 3.1.1 for* A_i?0

The exactitude of the presented analysis is limited by the exact knowledge of the maximum allowable gap length that permits a reasonable field in the air gap and the leakage in the air gap that imposes limits on the magnet height. Additionally parameters q and p are taken from the literature as empirical values specific to each design. These assumptions are checked in a finite element analysis of the three preliminarily chosen designs.

3.3 Verification of assumptions using FEA

Parameter values as of Figure 3.1.1 are compiled in Table 3.2 for three designs based on the parameter analysis in Section 3.2. Designs 1 and 3 reach the required actuation force of 4N, but their inertial mass is 50% higher. Design 2 leads to an acceptable mass, but the actuation force is too low. The magnetic energy product of the three designs $H_m B_m$ is rather low in comparison to a maximum of 300000J [40] as the working point is chosen to lie at high B-field values so that a rather high demagnetisation margin corresponding to a small demagnetisation field H_d is available. Hence a high current can be input at room temperature without demagnetising the permanent magnet. All three designs assume saturation of the magnetic field in the whole iron and a linear distribution of the magnetic field in the air gap. For designs 2 and 3 it is also assumed that the inner hole in the magnet does not significantly influence the strength of the permanent magnet. In the following a finite element analysis (FEA) of the magnetic field in the iron and the permanent magnet is carried out. First it is used to check whether the magnetic field in the iron yoke saturates homogeneously and the magnetic field in the air gap behaves linearly. Second ways are investigated to reduce the mass of the magnetic circuit without significantly reducing the magnetic field in the air gap and measures to increase the amount of magnetic field in the air gap are examined. Results are presented at the example of design 2.

Table 3.2: *Parameters of chosen magnetic circuit design (dimensions in mm)*

	A	A_i	h_g	s	B	D_o	B_{go}(T)	B_{gi}(T)	m(g)	F_a(N)	$H_m B_m$(J)	H_d(A/m)	h_{gl}
1	15	0	2.9	1.6	4.8	23.5	0.996	1.195	31.8	3.92	171810	174380	3.1
2	15	8	2.1	1.6	4.8	22.4	0.986	1.183	19.9	2.82	170520	172680	2.2
3	25	20	1.8	2	6	32.9	>1	>1.2	30	4.05	170880	173140	1.9

Figure 3.3.1 shows the distribution of the magnetic field in a cross section of one half of the modified design 2. In comparison to Figure 3.1.1 an additional chamfer of 0.3mm is added at

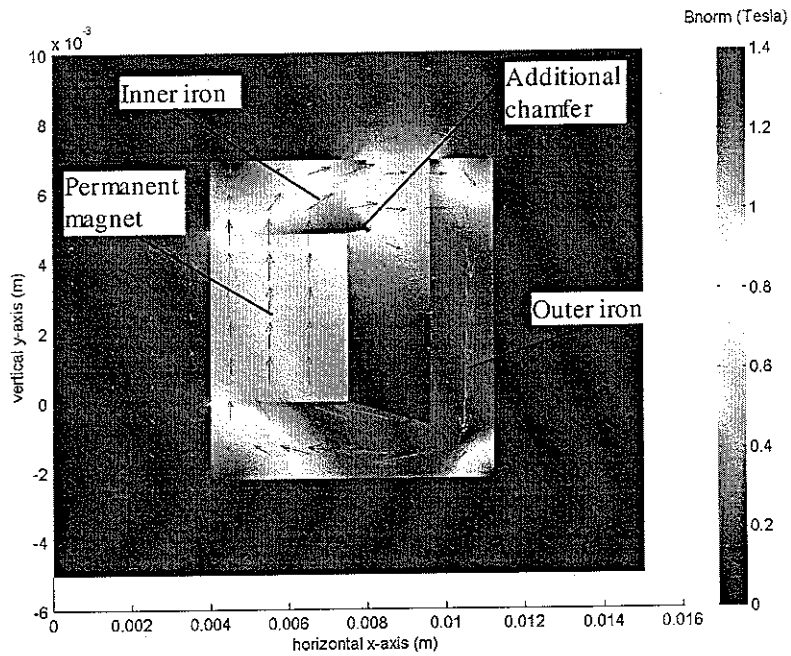

Figure 3.3.1 : *Linear plane simulation, design 2*

the connection of the permanent magnet and inner iron close to the air gap in order to prevent high saturation *B*-fields in this area. The magnetic circuit stretches infinitely in a direction perpendicular to the plane of the figure. A linear relation between the magnetic H-field and the magnetic B-field is assumed and the used material parameters are compiled in Table 3.3. The figure shows that in contrast to assumptions the magnetic circuit does not distribute homogeneously over the regions outer iron, inner iron and permanent magnet. Additionally the magnetic field in the air gap is much smaller than in the surrounding iron, which is also in contradiction to assumptions. The inner hole, however does not seem to greatly influence the magnetic circuit since the magnetic field stays concentrated in the iron parts. There are regions in the corners of the magnetic circuit that do not carry significantly more magnetic field than the surrounding field. Hence, removing these areas from the iron can reduce weight without significantly affecting the magnetic circuit.

Table 3.3: *Parameter values used for FEA simulations*

Parameter	Value	Description
σ_{fe}	$1.03\ 10^7$	Conductivity of iron and perm. magnet
μ_{rpm}	1	Relative permeability of permanent magnet
$M0$	962887.4 Aturns	Magnetisation of permanent magnet
μ_{rfe}	2000	Relative permeability of iron (linear simulations)

In Figure 3.3.2 simulation results are depicted for a cross section of the same design 2, this time assuming an axisymmetric shape of the magnetic circuit. In order to obtain the ring shape of the magnetic circuit the cross section is to be rotated by 360 degrees about the z-axis at r=0. In comparison to Figure 3.3.1 the magnetic field is more inhomogeneous in the iron and its values are reduced in the outer iron since the surface, which the magnetic flux penetrates going outwards, is larger. Moreover there is a strong field concentration in the lower right hand corner of the magnetic circuit in the iron.

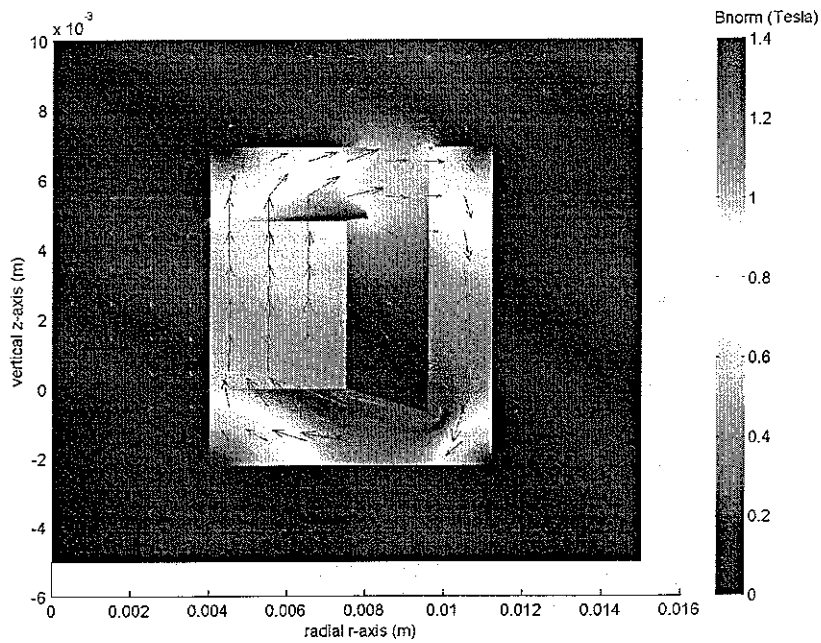

Figure 3.3.2 : *Linear axisymmetric simulation, design 2*

Simulations in Figure 3.3.1 and Figure 3.3.2 are carried out assuming a linear relationship between the magnetic B-field and the magnetic H-field. This assumption is only valid for small values of the magnetic B-field for iron materials. A *B-H* characteristic curve for dynamo steel extrapolated from [66] as depicted in Figure 3.3.3 is used for simulation results depicted in Figure 3.3.4.

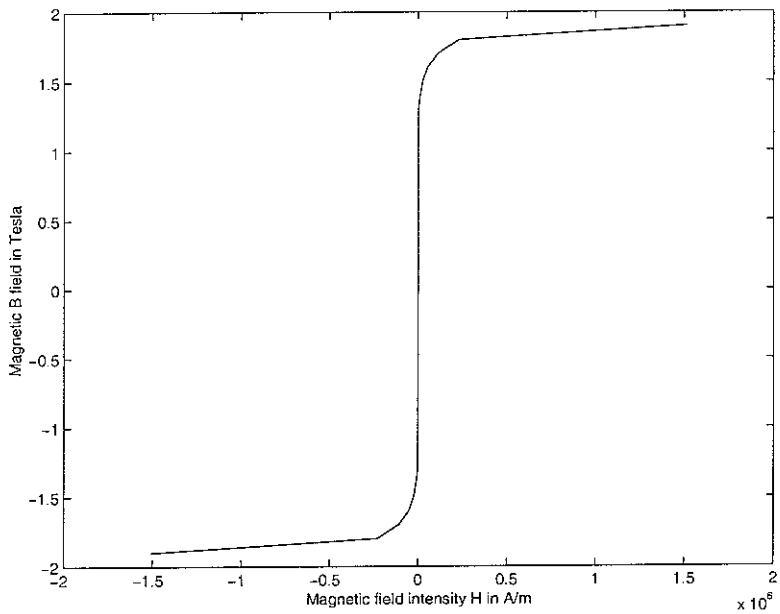

Figure 3.3.3: *Non-linear magnetisation characteristics, extrapolated from [66] for steel*

Moreover for simulations in Figure 3.3.4 less important iron parts are cut off so that weight reduction is achieved. In order to reduce the peak value of the magnetic field in the lower right corner the geometry is also slightly changed in this area. Results show a more homogeneous distribution of the magnetic field in the iron that is close to saturation in most parts. The magnetic field in the air gap, however, does not seem to be significantly increased so that further measures are considered. Figure 3.3.5 shows that horizontal distribution of the

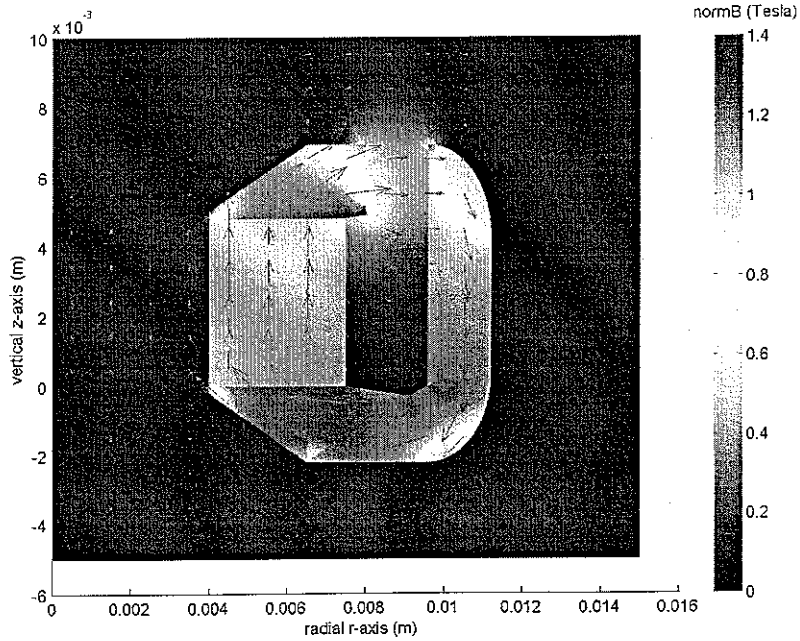

Figure 3.3.4: *Non-linear axisymmetric simulation using optimised geometry, design 2*

magnetic field in the air gap does not vary extremely over the air gap length. It illustrates that a two dimensional simulation and the assumption of a linear material (faint, solid line) overestimates the magnetic field in the air gap by about 40% relative to the non-linear axisymmetric case (dash-dotted line). When optimising the geometry the saturation effect on the magnetic field in the air gap due to the nonlinear material behaviour can be compensated (dashed line). The same is true for the vertical distribution of the magnetic field in the air gap depicted in Figure 3.3.6. Furthermore it shows a relative stable value of the magnetic field in a range of about 2mm. For strokes greater than 1mm a rather large nonlinearity of the actuation force is predicted. In order to increase the magnetic field in the air gap the introduction of an overhang in the air gap also on the side of the outer iron is considered,

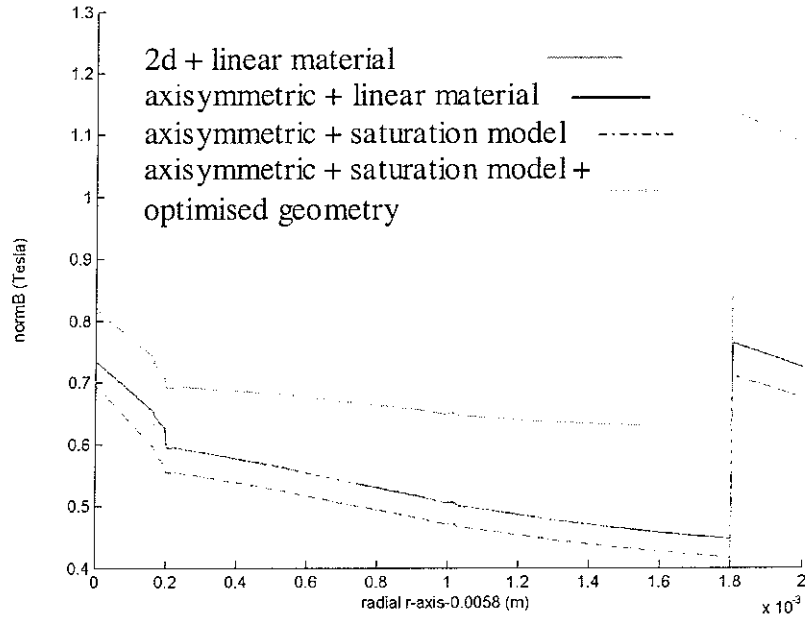

Figure 3.3.5: *Horizontal distribution in the vertical centre of the air gap, design 2*

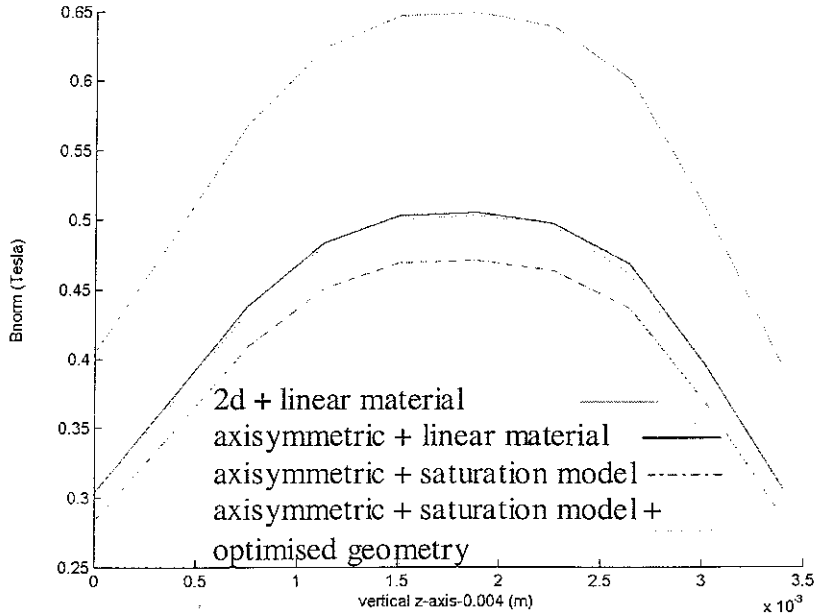

Figure 3.3.6: *Vertical distribution of magnetic field in the horizontal centre of the air gap, design 2*

since then the magnetic field should become more concentrated in the air gap and leakage should be reduced. Figure 3.3.7 shows the influence of the size of the overhang at constant air gap length. The difference between no overhang and 1.5mm overhang at an air gap length of s=1.6mm is rather small although the magnetic field in the outer iron directly at the air gap reduces a lot.

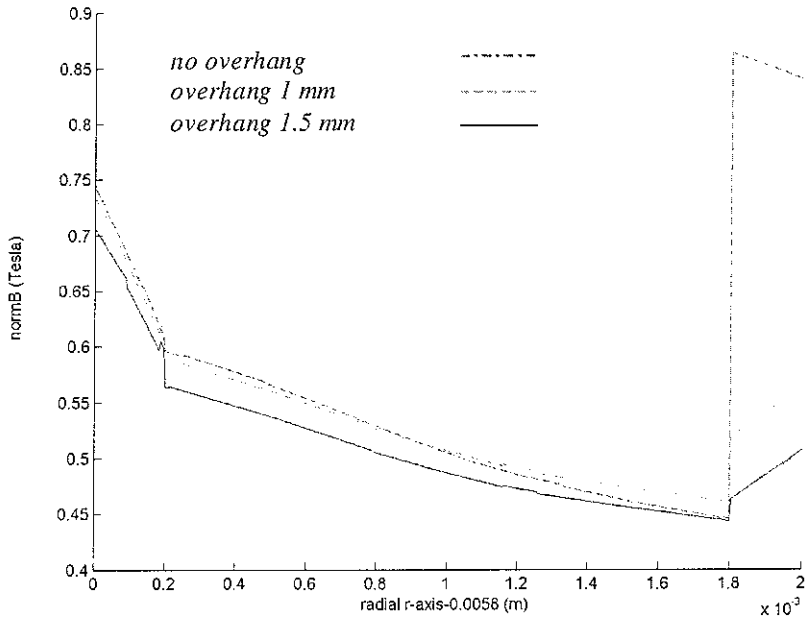

Figure 3.3.7: *Magnetic field in the air gap for different lengths of the outer overhang, design 2*

A large change of the magnetic field in the air gap can be achieved varying the air gap size. Figure 3.3.8 shows that by decreasing the air gap size from 2mm to 1mm in design 1 the magnetic field can be increased from 0.5 T to 0.7 T. For a further increase, even up to the desired saturation value at about 1.2T, a much smaller air gap is required that also affects the amount of wire in the air gap.

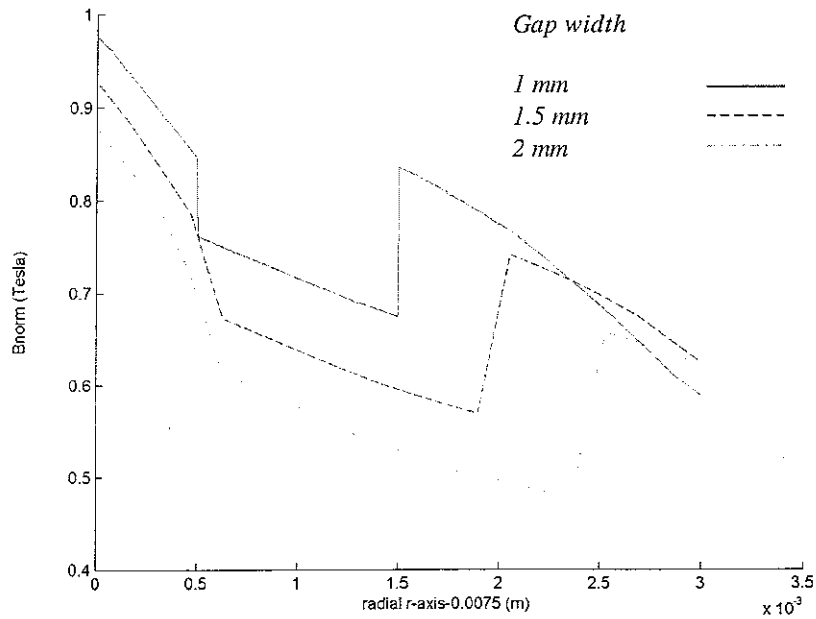

Figure 3.3.8: *Magnetic field in the air gap for different air gap lengths, design* 1

Optimising the geometry for designs 1 to 3 as in Figure 3.3.4 for design 2 leads to a largely reduced mass and more realistic values for the strength of the magnetic field in the air gap. Equations (3.16) to (3.20) of Section 3.2 give the actuation force when using the simulated values of the magnetic field in the air gap. The values are compiled in Table 3.4. Comparing Table 3.2 and Table 3.4. indicates that the magnetic field in the air gap is calculated to be much smaller using FEA than previously assumed and calculated using Equations (3.10)ff. Values for designs 2 and 3 vary much more from the approximate design method probably because of additional leakage inside the ring. A bigger mass reduction is possible when using a design without an inner hole since the outer edges to be cut off constitute a larger proportion of the whole magnetic circuit for smaller diameters. Hence only design 1 without an inner hole is considered in the following where further ways to increase the actuation force are investigated.

Table 3.4: *Maximum force and magnetic B field of designs 1 to 3 for the optimised geometry as in Figure 3.3.4*

Design	B_{go} (T)	B_{gi} (T)	m (g)	F_a (N)
1	0.45	0.58	15.5	1.2639
2	0.42	0.55	19	1.2596
3	0.35	0.45	25.9	1.4056

Increasing the strength of the permanent magnet potentially should increase the magnetic field since the source is enhanced. Figure 3.3.9 shows the result of a FEA of design 1 where the outer iron is replaced by a permanent magnet. In comparison to the values given in Table 3.4. the values of the magnetic field in the air gap are not significantly increased and a more difficult assembly is anticipated because two permanent magnets are to be handled. In fact saturation in the outer iron is decreased and more magnetic flux through air is visible since one permanent magnet acts for the other like air with a relative permeability close to one. Therefore a second permanent magnet is not advantageous.

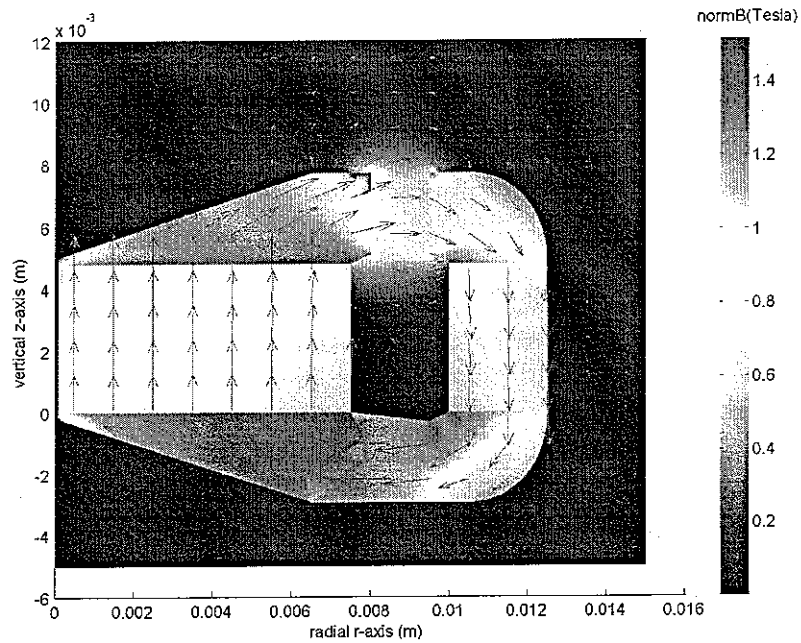

Figure 3.3.9: *Magnetic field when using an additional permanent magnet ring, design 1*

From Figure 3.3.8 we learn that the air gap length s should be much smaller for a sufficient magnetic field. But manufacturing limits for two coils, a former and clearance demand an air gap larger than about 1.5mm. Moreover the figure shows that an increase in the air gap by 25% does only lead to a reduction of the magnetic field by circa 16%. Therefore a rather larger air gap seems to be advantageous for a large force if the current carrying potential of the wire is also considered. In order to quantify these effects a new force mass calculation varying geometric parameters and using Equation (3.16) with a FEA for the calculation of B_g is carried out. Figure 3.3.10 shows the force, averaged magnetic field in the air gap and mass of different parameter combinations where an inner hole of diameter 2mm is assumed for mechanical purposes described in Section 4 and an additional outer permanent magnet is used. The upper points are the actuator force in Newton and the lower points are the magnetic field in the air gap in Tesla. In general at a given weight points with a relatively low magnetic

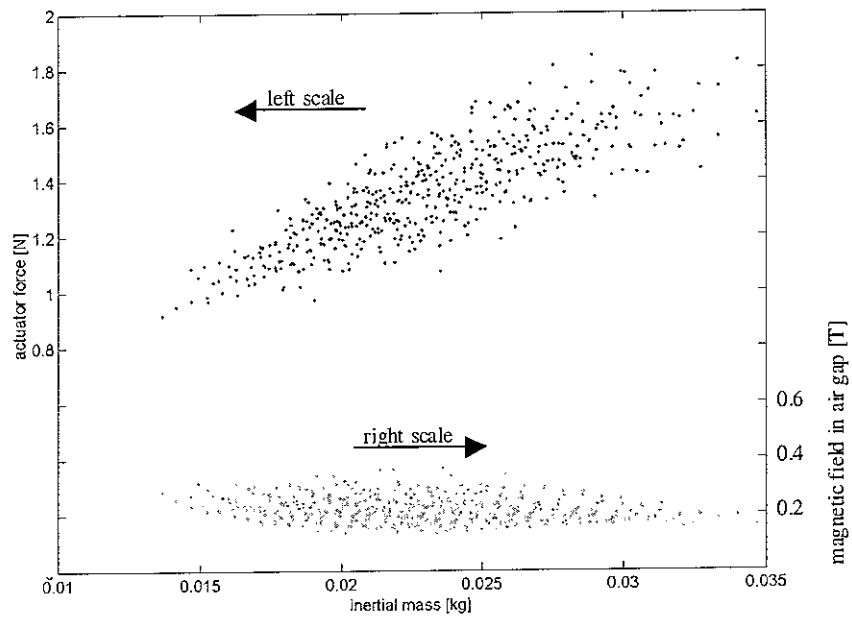

Figure 3.3.10: *Inertial mass vs. actuator force with different parameter combinations (A ,s ,h_g, b, A_i=2mm) using an additional outer permanent magnet ring*

field i.e. 0.3T instead of 1T tend to be associated with a high actuator force. But for lower magnetic field values the actuation force reduces again. Hence there is an optimal parameter combination that gives a maximum force at a given weight and that does not have a maximum magnetic field. A high amount of wire in the air gap compensates for a low magnetic field to give a high actuation force. This analysis, once more, does not include thermal effects that give a limit to the input power at a given air gap, permanent magnet and actuator volume. Figure 3.3.11 shows the same analysis for an actuator without an additional outer permanent magnet ring. In comparison to Figure 3.3.10 actuator forces are even higher for a given weight. Once saturation in the iron is reached a further increase in field source does only increase leakage without significantly affecting the magnetic field in the air gap. The same relation between magnetic field in the air gap and the actuation force at constant weight is also found. As before from Figure 3.3.11 a design whose values are compiled in Table 3.5 is chosen that fulfils the weight requirement on the actuator. Although this requirement is

Table 3.5: *Parameter values of the chosen magnetic circuit design*

Design	A	A_i	h_g	s	b	D_o	B_g (T)	m (g)	F_a (N)	h_{gl}
final	12.5	2	4	3	4.8	23.5	0.2972	20.3	1.6362	2.3

considered as being less important as the requirement on the actuation force it is still given priority due to the uncertainty about the possible input power. Simulations are carried out with an electrical power of P=1.25W (see Table 3.1), but higher values might well be possible leading to a higher actuator force. Moreover it is assumed that scaling up is easier than scaling down due to space considerations and a successful design would give a lower limit.

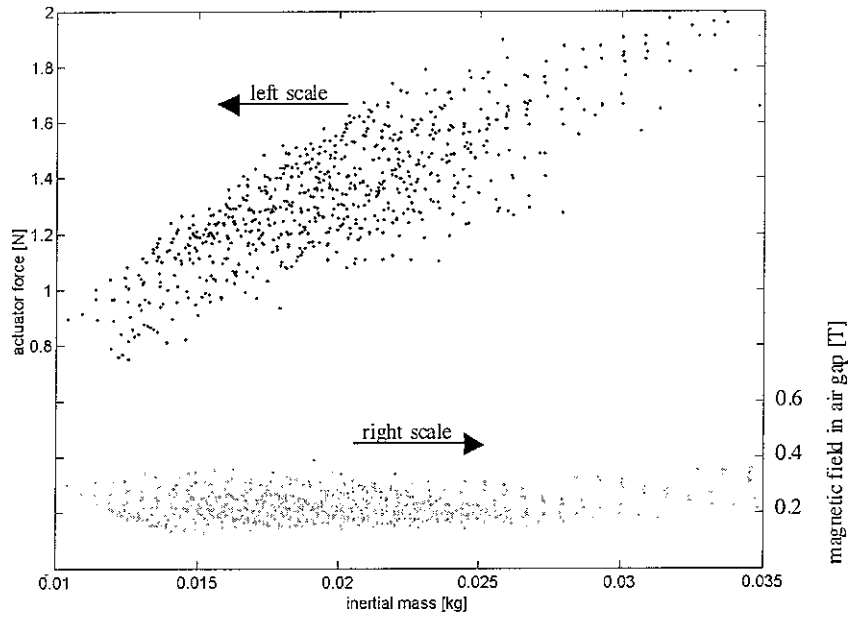

Figure 3.3.11: *Actuator force vs. inertial mass with different parameter combinations (A,s,h_g,b,A_i=2mm) without additional outer permanent magnet ring*

Figure 3.3.12 shows the simulation results of the magnetic field of the chosen design. In the air gap a homogeneous magnet field distributed over a large area with a rather small value results so that also no big change in the transducer coefficient with coil position is estimated.

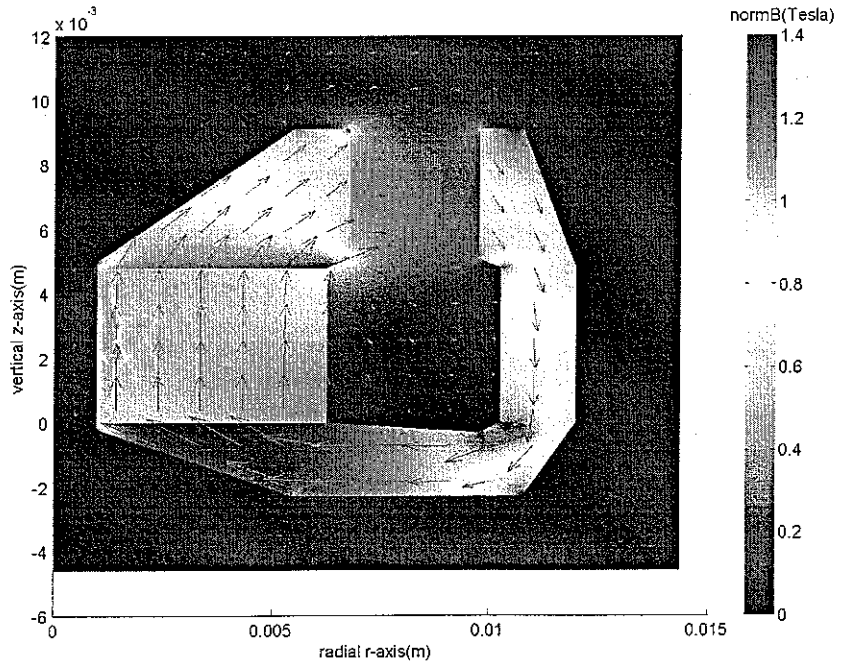

Figure 3.3.12: *Finally chosen magnetic circuit design*

4. INERTIAL ACTUATOR PARAMETERS

As a result of the electromagnetic design illustrated in Section 3 geometric design parameters of the electromagnetic circuit, the value of the inertial mass and an approximation of the maximum actuation force are fixed. For the design of an inertial actuator additionally the suspension of the inertial mass and its vertical guidance are to be determined. Furthermore a cover is necessary for protection and the coil assembly consisting of a primary, driving coil and a secondary measurement coil is to be designed. All these components should fit together so that the actuator can be assembled. First sketches of different combinations allow the assessment of each design version that are compiled from solutions of each function. Finally an appropriate combination of these components is chosen.

4.1 Suspension

The suspension supports the inertial mass statically and dynamically. There should not be a high static deflection so that the actuator can also be used upside down. Its dynamic behaviour should show a low resonance frequency (about 20Hz) of the inertial mass on a spring of about 20g. The required dynamic spring stiffness hence becomes $K=\omega^2 M=316$N/m. Any internal resonance frequency should lie outside the frequency range beyond 1kHz and its weight should be negligible. Moreover the suspension should be soft in vertical and stiff in horizontal direction and thus support the guiding function. It should allow the displacement of the inertial mass by at least +/- 1mm without exceeding the yield strength of the used material. Geometric constraints are given by the geometry of the electromagnetic circuit.

In general there are three places where to fix the suspension to the inertial mass with a vertical spring. The suspension spring could be added at the top of the inertial mass, at the bottom or at both places simultaneously. If it is placed at the top as it is schematically shown on the right hand side on the first line of Figure 4.1.0. the suspension length is increased. The suspension can be added at the bottom of the inertial actuator inside the coil or outside the coil. For vertical springs additional bending moments could be introduced when the springs are too close together inside the coil. Fixing springs with their main extension in horizontal direction (horizontally oriented springs) to the moving mass inside or outside the coils makes a difference in available suspension length. For horizontally oriented springs fixed outside the coil the coil diameter A and the outer diameter of the moving mass D_o limit the radial extension as illustrated in Figure 4.1.0 on the second line on the left side. The coil diameter A limits the suspension length for horizontal springs fixed below the moving mass inside the coil. Moreover assembly questions arise for suspensions fixed to the coil former. For easy assembly suspensions outside the coil are to be preferred. Considering the available suspension length an additional vertical suspension or an inner horizontally oriented suspension are favourable.

Different available vertical and horizontally oriented spring types are compiled in Figure 4.1.1. Some basic considerations allow eliminating some of them. A priori a post-buckling spring, for which the theory is explained in [75], is only linear in a certain range and its effectiveness largely depends on the limiting, maybe varying, geometric conditions. Approximate calculations of metal bellows using formulae given by [76] show that this kind of metal bellows requires a height of about 60mm in order to obtain the required stiffness so that a high stiffness in horizontal direction is not guaranteed and a low internal resonance

frequency in bending appears. Hence post-buckling springs and metal bellows are not considered further. Helical springs require pre-tension and therefore are also not favoured.

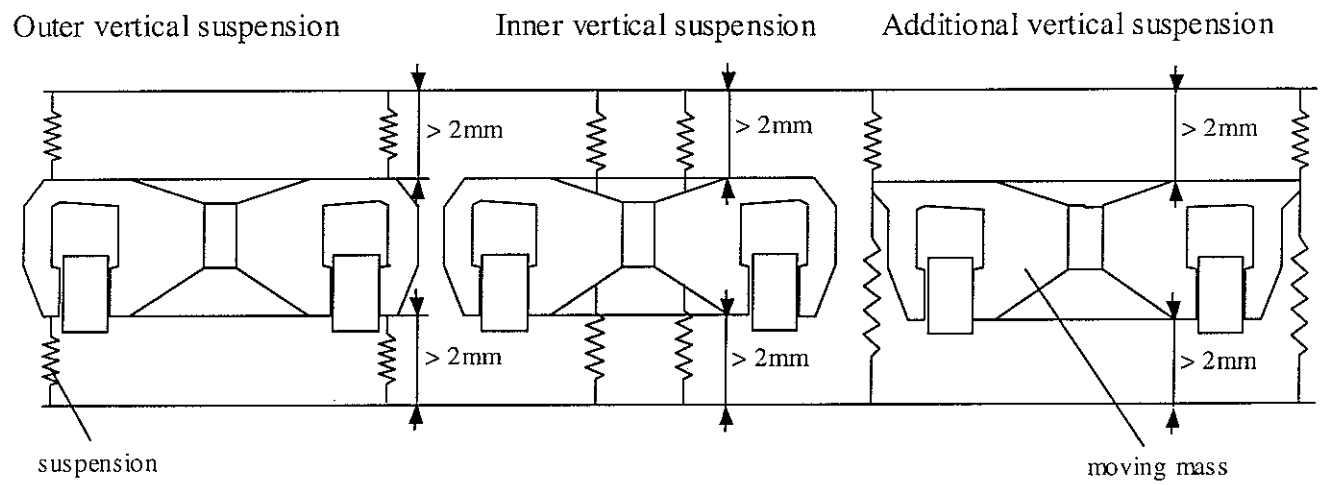

Figure 4.1.0: *Position of the suspension relative to the moving mass*

The choice between ring spring, leaf spring and membrane depends on machining issues, available geometry, mass, resonance frequencies and the yield strength of the used material. Therefore the maximum stress in the spring, its mass and approximate, internal resonance frequencies are calculated as a function of the spring length. The chosen material is phosphor bronze CuSn6 which does not interfere with the magnetic field of the inertial actuator and that has a high yield strength compared to other bronze materials. Since only certain springs with certain dimensions are possible at the positions discussed beforehand a choice of an advantageous spring is possible. For example a ring spring can only be used at the sides of the inertial mass so that the spring radius R is limited to about R= 0.005 to 0.01m. When approximately assuming a circular cross section and three ring springs to support the moving mass their maximum internal stress is given by [77]

$$\sigma_d = \frac{0.318R\left(I_d 4/\pi\right)^{0.25} 0.2}{3I_d} \qquad (4.1),$$

where $I_d = \frac{3R^3k}{20E3}$ is the moment of inertia with required spring stiffness k=316N/m for three ring springs and Young's modulus E=1.4×10^{11}N/m^2.

A leaf spring can first be used below the inertial mass so that its length is at maximum R=0.0055m, although spring assembly is more complicated. Second a horizontally oriented leaf spring can be used above the inertial mass, so that a suspension length of maximum R=0.0115m is possible. Three clamped-guided leaf springs as on the second line on the left in Figure 4.1.1 have a maximum stress of

$$\sigma_b = \frac{0.2R\left(I_b 4/\pi\right)^{0.25}}{3I_b} \tag{4.2}$$

with $I_b = \frac{R^3k}{12E3}$. Two hinged-hinged leaf springs as on the second line in Figure 4.1.1 the second schematic from the left are exposed to a maximum stress of

$$\sigma_c = \frac{0.2R\left(I_c 4/\pi\right)^{0.25}}{2I_c} \tag{4.3}$$

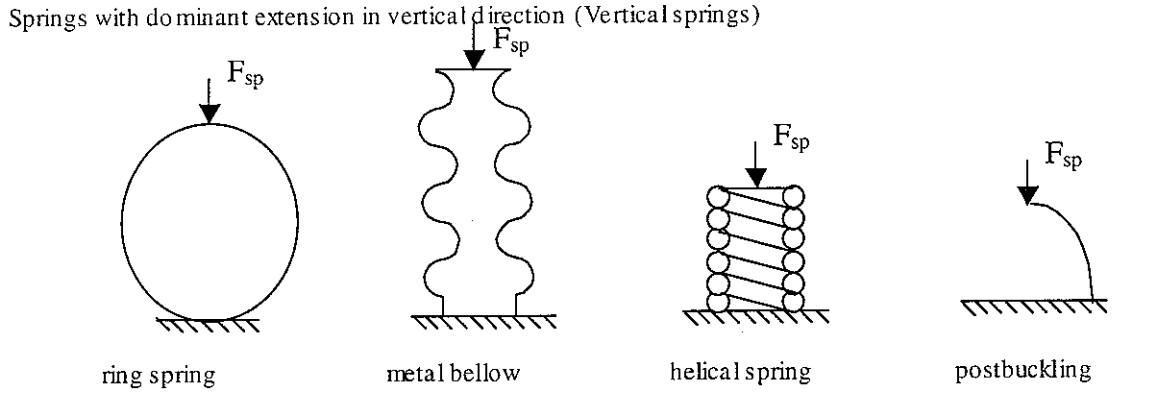

Figure 4.1.1: *Different options for the suspension of the moving mass*

where $I_c = \frac{(2R)^3 k}{48E2}$. A leaf spring with three leaves as on the second line the second sketch from the right in Figure 4.1.1 approximately sees a maximum stress of

$$\sigma_e = \frac{0.2(2\pi R/3)(I_e 4/\pi)^{0.25}}{3I_e} \tag{4.4}$$

with $I_e = \frac{(2\pi R/3)^3 k}{12E3}$ whereas the maximum stress in a leaf spring with two leaves as on the second line of Figure 4.1.1 the last sketch on the right is approximately

$$\sigma_f = \frac{0.2(2\pi R/2)(I_f 4/\pi)^{0.25}}{2I_f} \tag{4.5}$$

with $I_f = \frac{(2\pi R/2)^3 k}{12E2}$. For comparison three ideal cantilever beams would have a maximum stress of

$$\sigma_a = \frac{0.2R(I_a 4/\pi)^{0.25}}{3I_a} \tag{4.6}$$

with $I_a = \frac{R^3 k}{3E3}$. But due to the necessary guidance of the mass this boundary condition is not realizable in practice. A helical spring can be used above and below the inertial mass limiting the spring length to either about R=0.0055m or R=0.0115m. Following formulae in [81] the stress in the spring windings decreases with increasing winding number so that the case of one winding gives an upper limit with a maximum stress of

$$\sigma_g = \frac{0.2R(I_g 2/\pi)^{0.25}}{I_g} \tag{4.7}$$

where $I_g = \frac{2\pi R^3 k 2.6}{E}$. Figure 4.1.2 depicts the maximum bending or shear stress for the different springs as function of the spring dimension R. Helical springs have the smallest internal stress at all spring lengths followed by the ring springs. But helical springs are loaded in torsion with lower material yield strength than for bending and they require pre-stress. A guided beam and hinged-hinged beams have the largest internal stress. The star and the cross in Figure 4.1.2 indicate maximum stress in the spring calculated with a FEA of a 2 leaves spring and a ring spring with dimensions fitting to the magnetic circuit design. Although the radius of the ring spring is smaller than the length of the two leaves spring the maximum stress in the ring spring is smaller.

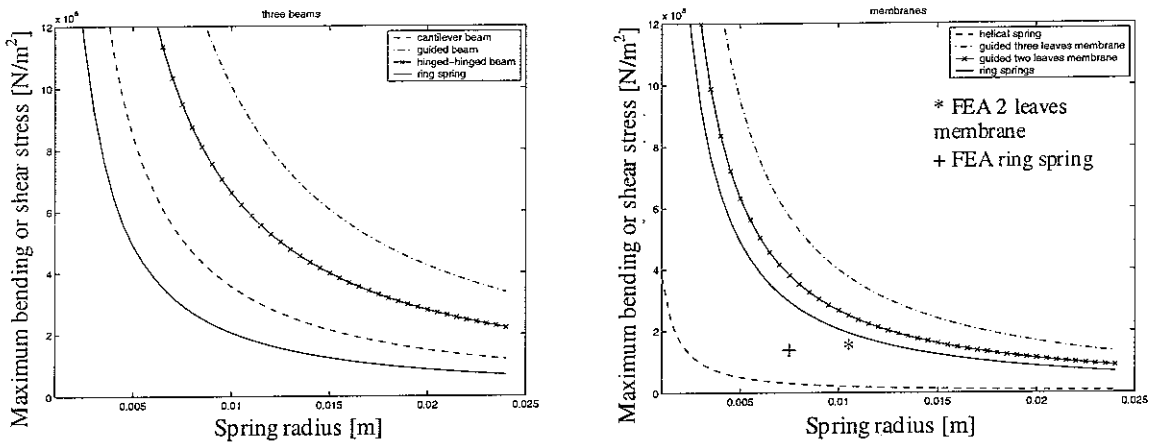

Figure 4.1.2: *Internal stress at 316N/m suspension stiffness as function of spring radius and for various spring configurations*

Figure 4.1.3 shows calculated, internal resonance frequencies using the desired stiffness of 316N/m, a spring mass assuming shapes as of Figure 4.1.1, a mass density for CuSn6 of ρ=8700kg/m^3 and formulae from [78]. The ring springs show the lowest internal resonance frequency in comparison to the beam versions, but their lowest internal resonance frequency is in the same range as a two leaves spring and a bit lower than the resonance frequency of a three leaves spring. Helical springs have the lowest internal resonance frequency. For the realizable dimensions R all values of the resonance frequency lie far above the resonance frequency 20Hz of the inertial mass of 0.02kg supported by a spring of stiffness 316N/m. No spring does lead to internal resonance frequencies beyond 1kHz at dimensions that are compatible with the maximum yield strength of 340MPa for phosphor bronze [79].

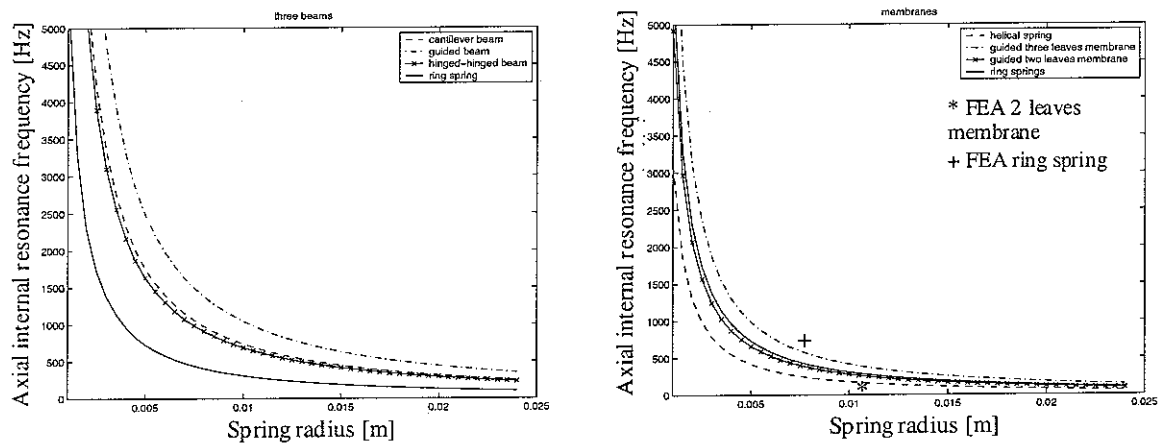

Figure 4.1.3: *Resonance frequency of various spring configurations as function of spring radius*

Finally Figure 4.1.4 depicts the mass of different spring versions. Guided beams have the lowest weight and helical springs show the highest weight. But even the highest weight, except for the helical springs, is below 0.0005 kg and negligible relative to the weight of the inertial mass.

In conclusion based on the internal resonance frequency and the mass criterion helical springs are eliminated as they lie too close to the 20Hz resonance frequency at a relatively high weight. For the remaining springs since no internal resonance frequency lies beyond the desired frequency bandwidth limit of 1kHz and, except for the helical spring, also far above

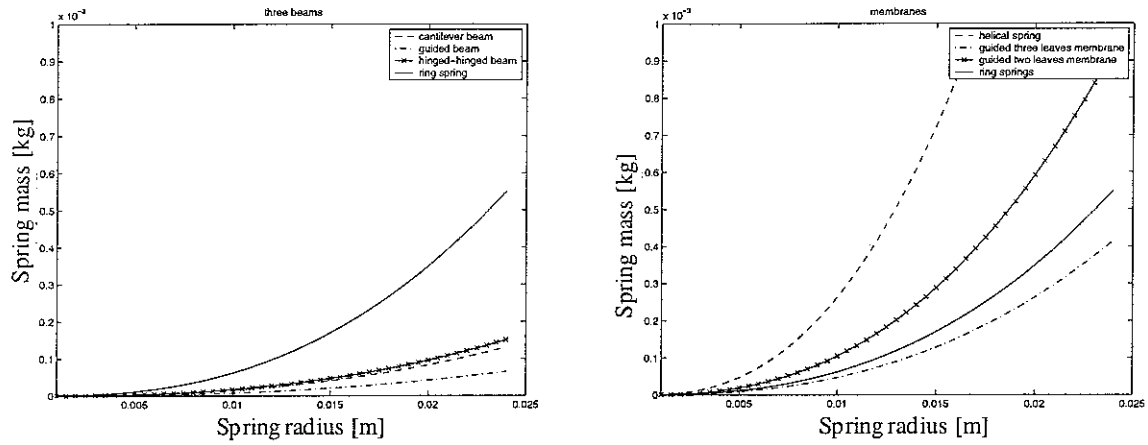

Figure 4.1.4: *Mass of various spring configurations as function of spring radius*

the 20Hz resonance frequency the resonance frequency is no decisive criterion. Especially since the mass is negligible for all remaining spring versions no major influence of the internal resonance frequency of the overall dynamic behaviour is anticipated. Therefore the maximum stress in the material becomes the criterion on which to choose an appropriate spring version. Based on this criterion ring springs are chosen as appropriate springs with the lowest internal stress of the remaining spring versions.

In order to verify the approximate internal resonance frequencies of Figure 4.1.3 and the available displacements at acceptable stresses dynamic and static FEA have been carried out on some mentioned spring types and additional ones from [55]. The first four calculated resonance frequencies are compiled in Table 4.1 for each spring type. In contrast to Figure 4.1.4 the resonance frequencies of the ring springs lie much higher since finite element (FE) simulations assume clamping of the ring at two sides. Simulations indicate that boundary conditions and even the amount of clamping play an important role for this type of spring. The other membrane like springs show first resonance frequencies in a comparable range above the 20Hz critical resonance frequency, but below the 1kHz bandwidth limit.

Table 4.1: *First four resonance frequencies of various spring versions in Hz*

Spring	1^{st} res. freq.	2^{nd} res. freq.	3^{rd} res. freq.	4^{th} res. freq.
Ring	652	855	2263	2341
Two leaves	187	749	1540	2643
Trefoil	254.56	362.34	362.43	759.39
Spiral	165	290	309	395

Figure 4.1.5 shows the displacement of a two leaves spring with appropriate dimensions that is exposed to a load of 0.2N at the centre. The required vertical displacement of +/- 0.001m can be reached, but high stresses up to 1000MPa appear around sharp angles that can only partially reduced by reducing the angle sharpness.

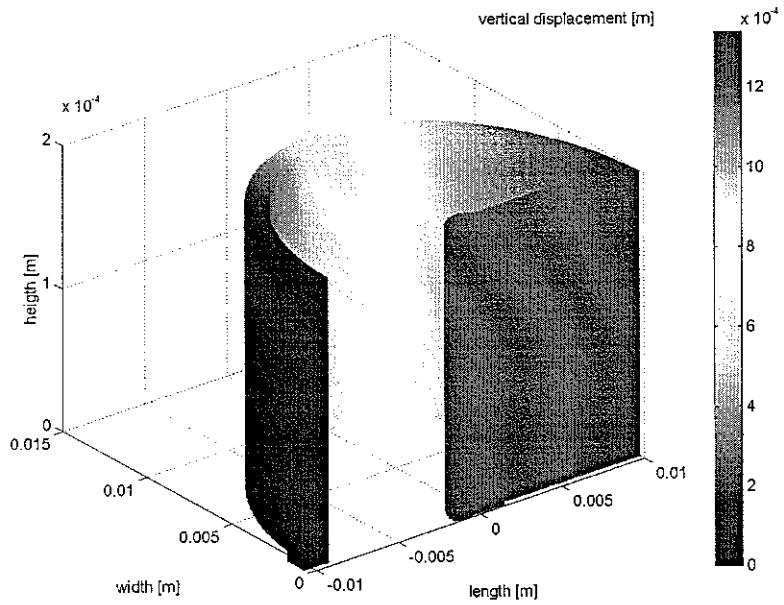

Figure 4.1.5: *Deformation in a leaf spring subject to axial load of 0.2N in the centre; only half of the spring that is symmetric about its length-axis is shown*

Figure 4.1.6 shows a trefoil membrane from [55] that may reach the required displacement, but also only with high stresses, indicated by the spring colour, up to 1200MPa at sharp edges. Although sharp edges could be further reduced a quite complicated deformation shape seems to be sensitive to horizontal shocks.

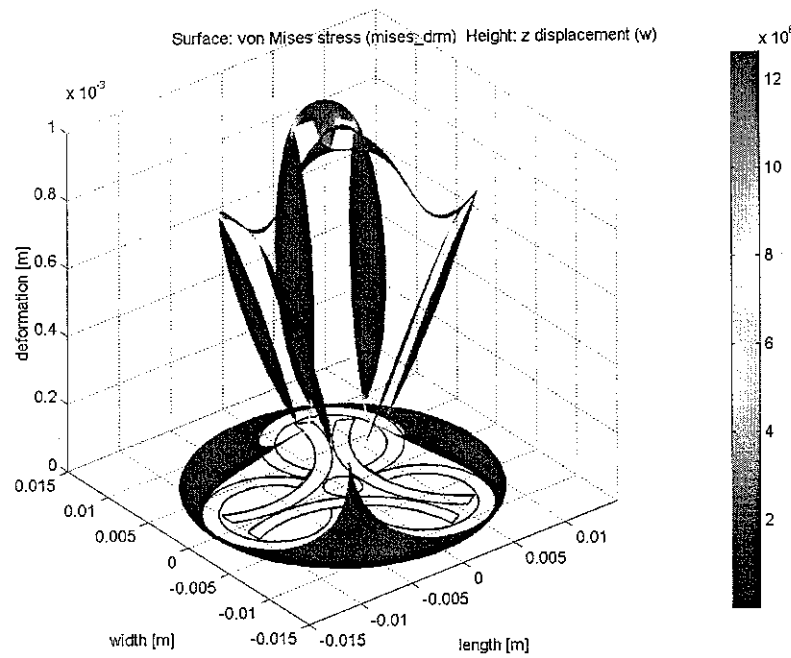

Figure 4.1.6: *Von Mises stress and deformation in a leaf spring subject to axial load of 0.2N in the centre*

Also a sensitive static deformation shape of a spiral membrane spring is depicted in Figure 4.1.7. The number of spiral windings cannot be reduced since stiffness would increase. As the membranes before also high internal stresses over 1000MPa are simulated.

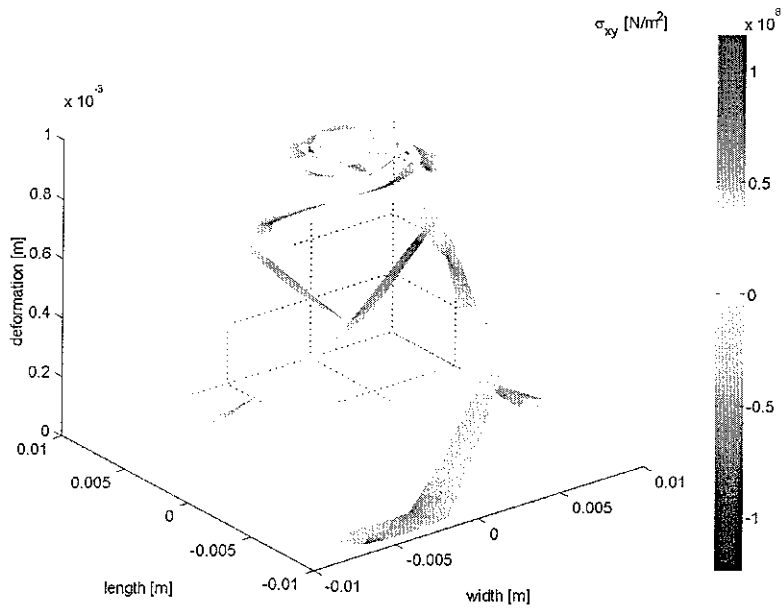

Figure 4.1.7: *Stress and deformation in a leaf spring subject to axial load of 0.2N at the centre hole*

These FEAs also show the advantage of the ring spring version with low internal stress and rather high internal resonance frequencies that can be adjusted by varying the boundary conditions. If other constraints forbad adding ring springs this analysis shows that two leaves springs would be a good second choice.

4.2 Guides

Since the moving mass should displace with a rather large stroke of at least +/-1mm also at high frequencies a guide of the mass in vertical direction is necessary. It additionally avoids moment excitation and hence excitation of rotational resonance frequencies if chosen appropriately. Stiffness in horizontal direction is increased using a vertical guide. Figure 4.2.1 shows different basic guide possibilities.

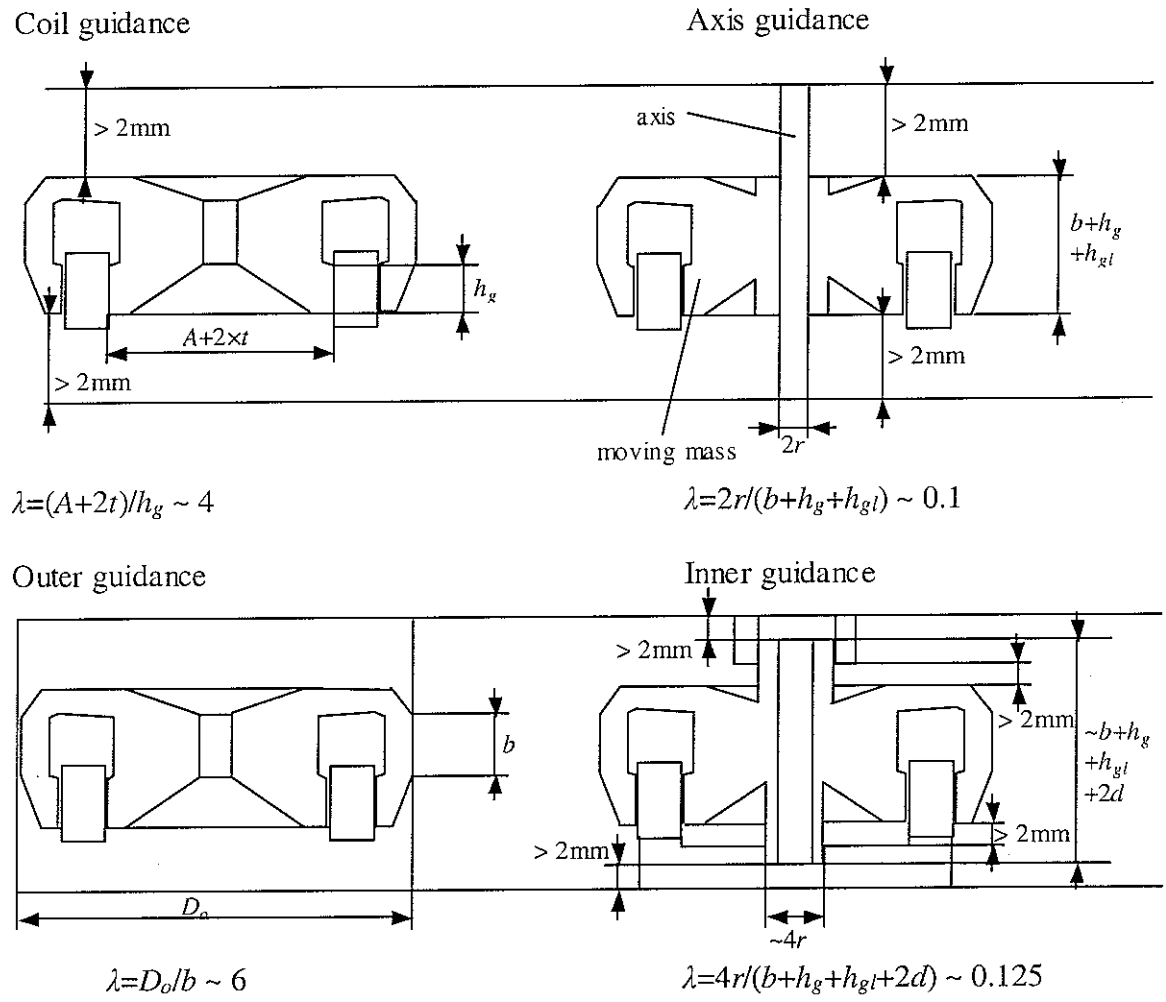

Figure 4.2.1: *Position of the guidance relative to the moving mass*

The coil can be used for guidance, an additional axis of radius r can be introduced for guidance, the mass can be guided at its outer diameter or additional protrusions could be used to guide the mass at its inner diameter. In order to evaluate these four possibilities a guidance factor λ as ratio of the guide diameter and the guide length is introduced. It should be smaller than one indicating a long guidance length over a small diameter so that a possible rotation of the mass is minimized. For the given magnetic circuit dimensions the guidance factor is evaluated in Figure 4.2.1 for the four different choices. Guidance at the outer diameter is worst because of the small height – diameter ratio of the magnetic circuit. Although the guide might be integrated with the sealing function discussed in Section 4.3 cover weight potentially is increased in addition to the bad guidance factor. Using the coil as guidance is also not advantageous because of the small guidance length. Hence an additional guide probably

would have to be introduced. A guide within the coil diameter has a small λ factor, but it is not compatible with a suspension inside the coil and there might be problems to align the upper and lower cover part. Finally an additional axis has the smallest λ factor and if the radius of the axis r is chosen small enough it will not interfere with an inner suspension. However the longer the axis, the higher the internal stress due to a bending moment when the mass does not move ideally vertically. Additionally the maximum surface pressure due to the bushing that the material can resist gives a lower limit on the diameter of the axis. Figure 4.2.2 shows the upper limit on the axis length due to the yield strength of the axis (solid line) and the lower limit on the axis radius due to the surface pressure of the bushing (dashed line) for a steel axis subject to the static load of the inertial mass in the centre. A lead bronze commonly proposed for bushings has been assumed as bushing material. Note the different scales for the axis length, which indicates that a large range of axis lengths and radii are possible. An axis of about 20mm length with a radius of 0.00075m should statically support the load. This is also a standardized radius of ISO 2338 pins. Stainless steel is chosen since austenitic steel influences a magnetic field less than ferritic steel.

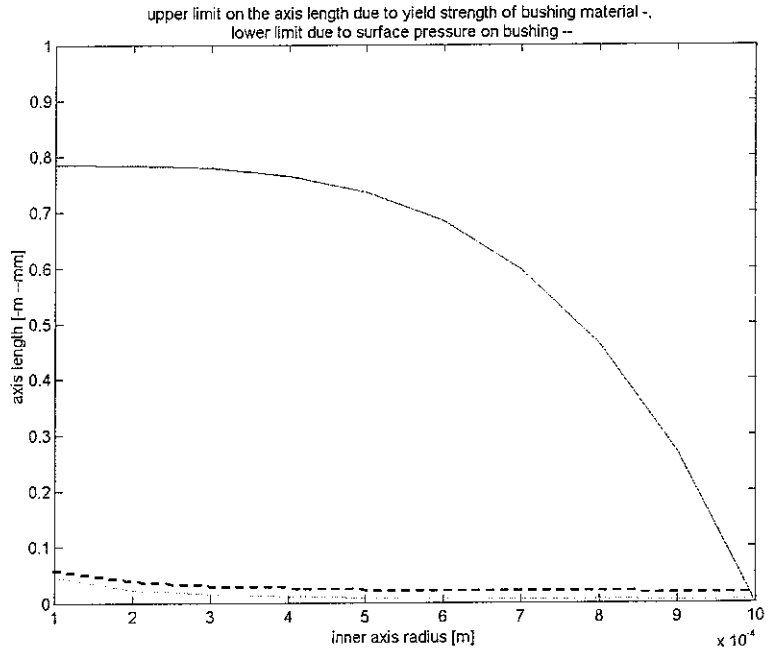

Figure 4.2.2: *Limits on axis length due to yield strength of axis material and surface pressure on bushing*

4.3 Cover

Since small particles might block the air gap an external housing is to prevent the introduction of small metal chips into the actuator. Figure 4.3.1 shows different cover designs with internal axis. Designs with inner guidance can be easily imagined in the same way. A complete housing gives the biggest insurance that no metal chips are introduced in the housing. A seal at the outer diameter of the inertial mass might be combined with the guidance function but complete sealing is not guaranteed and the inertial mass might be blocked if it is slightly rotated. Inversely the cover might be connected to the moving mass, but the same limits as before are valid. As an advantage the ratio moving mass / total actuator mass is increased since the cover is added to the moving mass. Reducing the gap by decreasing the sealing diameter is not advantageous since then the direct force path from the coil to the environment

is destroyed and disturbing moments are introduced. Additionally there is less space to place the axis so that the actuator potentially becomes taller.

A dynamic FEA of a complete cover has been carried out and it shows that using an internal guidance axis to support the top of the cover increases stiffness of the housing. An increase of the first cover resonance frequency from 6kHz to 9kHz is also observed. Aluminium has been assumed as the cover material because of its relatively high yield strength at low weight and its non-ferromagnetic properties.

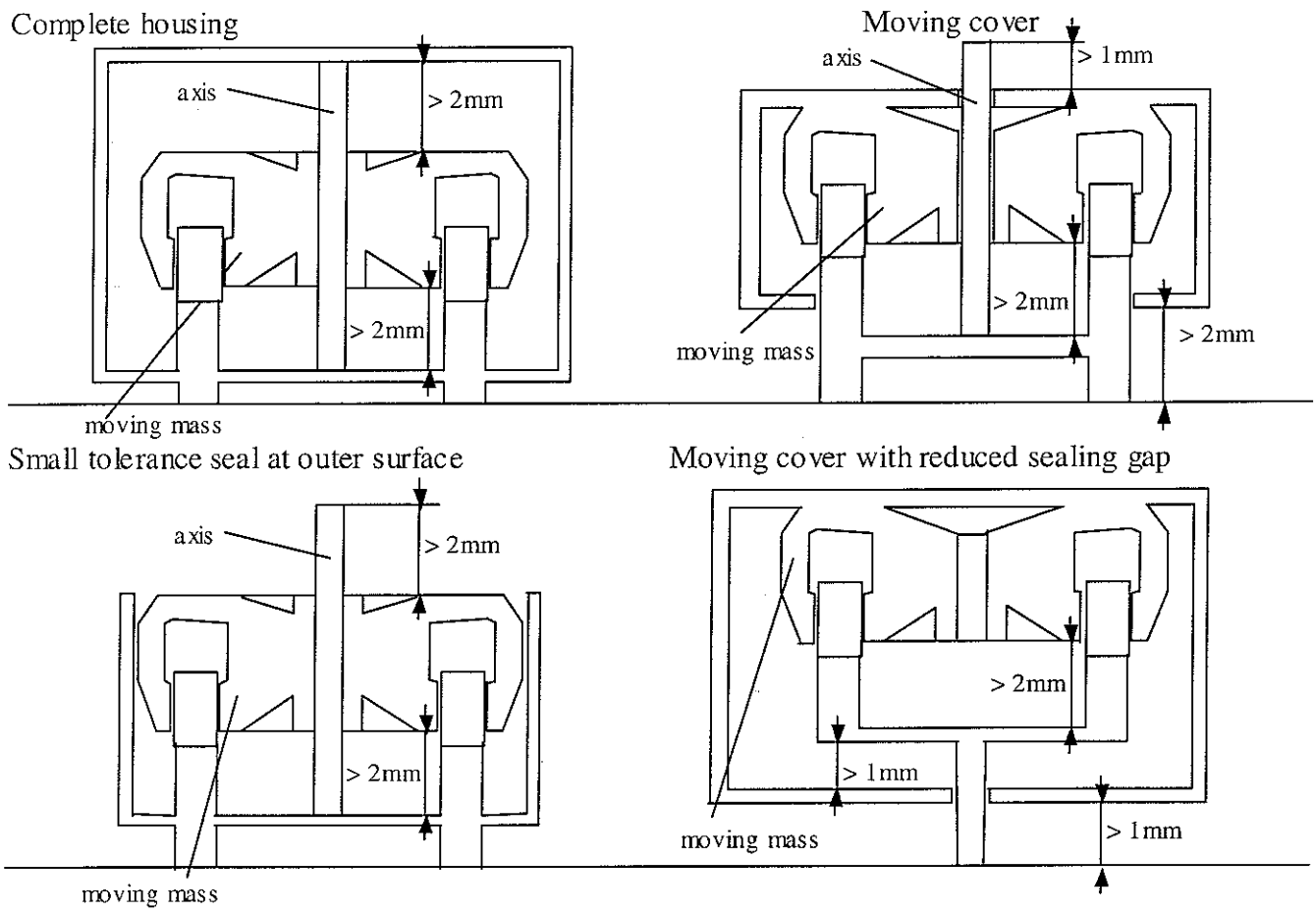

Figure 4.3.1: *Different housing options*

4.4 Driving and measurement coil

An important part to guarantee the functionality of the electrodynamic actuator is the driving coil that carries the current for the force generation following Equation (3.13). Since it also is a conducting wire moving in a magnetic field following Ampere's law a voltage will be induced in the wire. This induced voltage or back electromagnetic force (EMF) can be used to sense the velocity of the moving mass relative to the cover. Feedback of this voltage can then be used for adding damping to the lightly damped mode of the moving mass on a spring or other observable modes of the actuator or an attached structure. When using the voltage induced in the driving coil a trade-off between a strong transducer coefficient in order to easily drive the mass and to easily detect the induced electromagnetic force (EMF) appears that leads to a reduced bandwidth as illustrated in [12] and mentioned in Section 2.3. When

instead using a secondary coil that is optimised for sensing together with the primary coil that is optimised for driving as illustrated in Figure 4.4.0 sensing and control bandwidth should be increased. First the choice of driving coil parameters is presented; second the design of the measurement coil is described. A coupling transformer effect between both coils is predicted.

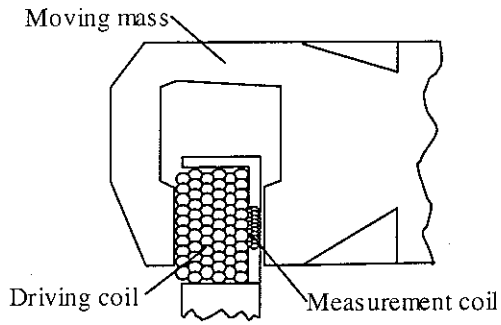

Figure 4.4.0: *Cross section sketch of moving mass and coils*

The wire diameter of the driving coil should be chosen so that a maximum actuation force is generated on the moving mass. Using Equations (3.13)-(3.15) and Equation (3.18) the actuation force as a function of the wire diameter d_w is

$$F_a = B_g I l_{cg} = B_g \sqrt{\frac{P\pi}{4\rho_{wi}}} \left[d_w \sqrt{\pi(A+2t+s)Nn + l_{con}} - \frac{d_w l_{con}}{\sqrt{\pi(A+2t+s)Nn + l_{con}}} \right] \qquad (4.4.1)$$

where $N=(h_g+2d)/d_w$ is the number of wire layers in vertical direction and $n=((s\text{-}tol)/d_w-1)2/\sqrt{3}+1$ is the number of wire layers in horizontal direction including a constant for the thickness of the coil former and gap clearance tol=0.0005m. This constant is determined by manufacturing considerations. Figure 4.4.1 shows the actuation force (solid line) from Equation 4.4.1 as function of the wire diameter for the chosen magnetic circuit design whose parameters are compiled in Table 3.5 and a power input of P=5W.

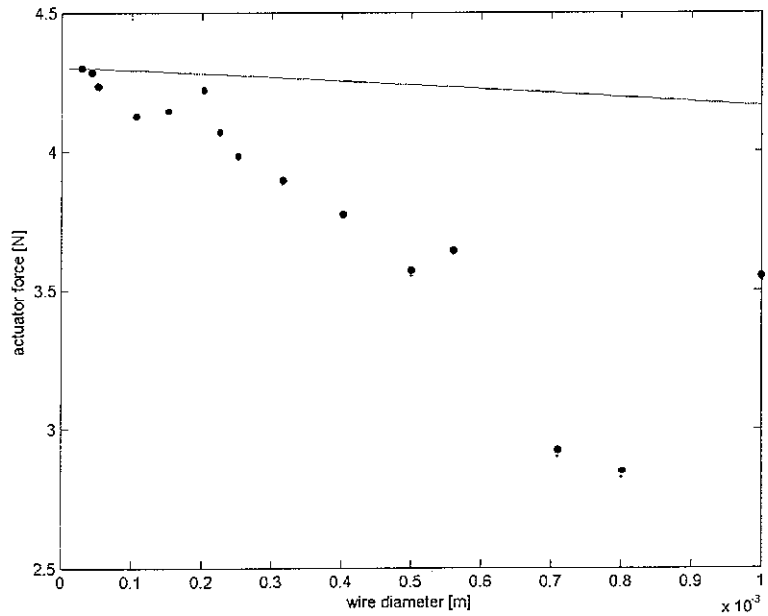

Figure 4.4.1: *Actuator force as function of driving coil diameter assuming either ideal filling of air gap (line -) or constant air gap for selected wire diameters (dots '.')*

The actuation force is maximum at d_w=0 that is not a realizable value. Figure 4.4.1 indicates that the smallest, possible wire diameter should be chosen. First manufacturers just provide discrete wire diameters (0.025, 0.042, 0.052, 0.105, 0.15, 0.2, 0.224, 0.25, 0.315, 0.4, 0.5) $\times 10^{-3}$ m. Second the number of coil windings in vertical N and horizontal n direction has to be an even number greater than zero so that the wire may be easily conducted out of the air gap. Additionally it is estimated that the manufacturing method limits the number of horizontal layers to n<10. For the chosen particular design this limit is verified to lie rather at 5 than at 10 as illustrated in Section 5. Finally since common power supplies should be used the current is limited to about 2A. A more decisive limit is given by the possible electrical input power that can only precisely be determined at the built device. The actuation force for the given wire dimensions at constant air gap and even number wire turns is depicted in Figure 4.4.1 where the corresponding points are lower than the continuous distribution with completely filled air gap as a certain space in the gap is not filled with wire. Figure 4.4.2 shows the number of windings of the available wire diameters that fit into the air gap. Since no more than 10 layers should be used in horizontal direction a minimum wire diameter of 0.25mm is recommended.

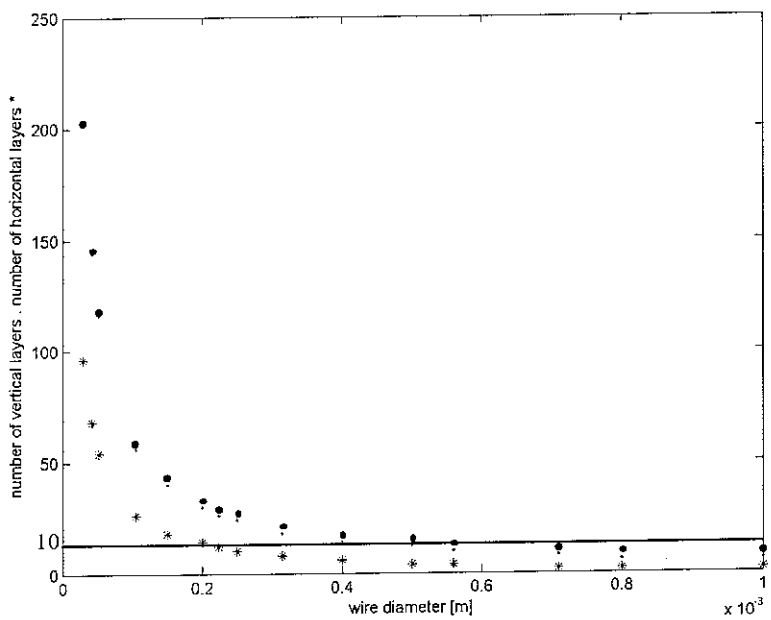

Figure 4.4.2: *Number of windings as function of discrete driving coil diameter, number of vertical layers (dots .), number of horizontal layers (stars *)*

Figure 4.4.3 shows the coil current as a function of the wire diameter at a power input of 5 W. Since the electric circuit is to be implemented with common laboratory equipment no more than 2A should be input so that the thickest usable wire diameter is 0.35mm. A thermal limit due to the heating of the coil wire that may destroy the wire insulation beyond 155°C is not yet considered here. As mentioned before the thermal limit due to the heating of the permanent magnet to 80°C also limits the maximum input power and hence the actuation force; but it can only correctly be determined ex post at a prototype.

In conclusion a wire diameter of 0.315×10^{-3}m with 18 vertical and 8 horizontal windings is chosen for the driving coil based on the manufacturing constraint and the maximum allowable current.

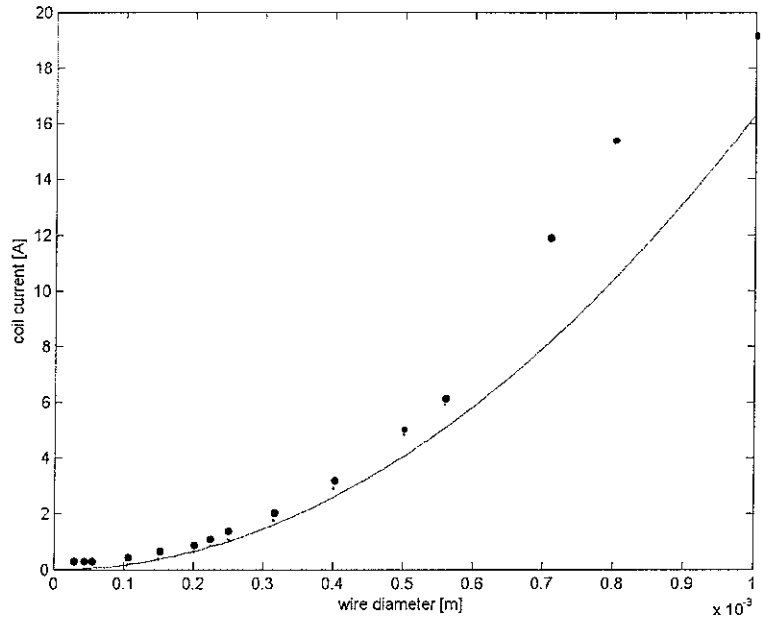

Figure 4.4.3: *Coil current at 5W power input as function of driving coil diameter, either assuming complete filling of air gap (line-) or constant air gap for selected wire diameters (dots .)*

In order to be able to measure the relative velocity up to very high frequencies without compensators the electrical cut-off frequency should be as high as possible [12]. The electrical cut-off frequency is given by

$$\omega_e = R_s / L_s \tag{4.4.2}$$

where the self-inductance of the measurement coil at a current I_s

$$L_s = \frac{(N_s n_s)^2 \Psi_{11}}{I_s} \tag{4.4.3}$$

depends on the integral of the magnetic field in one coil winding $\Psi_{11} = \int BdA$ where the index s indicates secondary coil values. Hence the electrical cut-off frequency is approximately given by

$$\omega_e = \frac{4\rho_{wi}\left((A+2t+s)N_s n_s + l_{con}\right)}{(N_s n_s)^2 \Psi_{11}(1A) d_w^2 \pi}. \tag{4.4.4}$$

Ψ_{11} can be estimated using a FEA of the magnetic model where a current is input to the coil and the resultant integral of the magnetic field over the coil windings is calculated. Despite considering saturation properties of the iron core no dependence on the input current

amplitude of Ψ_{11} is observed. Equation (4.4.4) indicates that the wire diameter and the amount of windings should be as small as possible for a high electrical cut-off frequency. Limits are given by the available space for a measurement coil and fabrication constraints since the driving coil cannot be completely wound only on the measurement coil with the used manufacturing method. Therefore the vertical space for the measurement coil is smaller than the space for the driving coil. A minimum of only 2 layers in horizontal direction should be used for the measurement coil. Values of 0.03 mm, 0.042 mm, 0.052 mm and 0.15 mm are available for the measurement wire diameter and because of manufacturing considerations a wire diameter of 0.052 mm with 2 layers horizontally and 38 layers vertically is chosen.

In addition to the induced voltage effect there is the direct coupling transformer effect between the two coil windings. When using formulae from [73] it can be shown that the current I_p in the primary coil is approximately linked to a voltage U_s in the secondary coil by

$$U_s = \frac{N_s n_s A_s \mu N_p n_p}{h_p} j\omega I_p \tag{4.4.5}$$

where $N_s n_s$ is the number of windings of the secondary coil, $A_s=\pi(A+s+2t)^2/4$ is the cross section of one winding, $N_p n_p$ is the number of windings of the primary coil, h_p is the height of the primary coil and $\mu=\mu_r 4\pi 10^{-7}$ is the permeability of the magnetic circuit that contributes to the coupling. This transformer voltage compares to the voltage U_{inds} induced in the secondary coil due to the movement of the inertial mass with a maximum stroke of d=0.001m

$$U_{inds} = \pi\left(A+2t+s\right) N_s n_s B_g j\omega d \tag{4.4.6}$$

where B_g=0.2972T is the magnetic field in the air gap given in Table 3.5. With $\mu_r \approx 1$ for the permanent magnet $U_{inds}>U_s$ if

$$I_p < \frac{4 B_g h_p d}{\left(A+2t+s\right)\mu N_p n_p} = 2.39A \tag{4.4.7}.$$

This is in coherence with the constraint for the maximum current in the primary coil I_p<2A used before so that a sufficient induced voltage signal is expected.

4.5 Design Combinations

In the design steps described in Sections 4.1 to 4.3 several possibilities turned out to be able to give a solution for a certain functionality if regarded separately. A combination of these solutions might not be possible so that in the following combinations of feasible solutions are compiled, investigated for their feasibility and evaluated regarding their fulfilment of requirements. Figure 4.5.1 schematically compiles the investigated solutions for the functions suspension (S) from Section 4.1, spring (Sp) from Section 4.1, vertical guide (G) from Section 4.1 and cover (Co) from Section 4.3. Solutions that have already been eliminated are crossed out. A total of 2^4 =16 combinations is available; but an additional suspension (S3) cannot be combined with a 2 leaves membrane spring (Sp8) and an inner suspension (S5) cannot be

Function	1	2	3	4	5	6	7	8
Suspension (S) from Section 4.1	Vertical			Horizontal				
	Outer 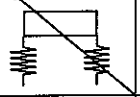	Inner 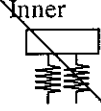	Additional 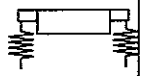	Outer 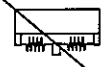	Inner 			
Spring (Sp) from Section 4.1	Vertical				Horizontal			
	Ring spring	Metal bellow	Helical spring	Post buckling	3 clamped-guided springs	2 hinged-hinged springs	3 leaves membrane	2 leaves membrane
Vertical guide (G) from Section 4.2	Coil 	Axis 	Outer 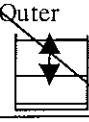	Inner 				
Cover (Co) from Section 4.3	Complete housing	Moving cover outer	Moving cover inner	At outer surface				

Figure 4.5.1: *Compilation of required functionality and possible solutions*

combined with a vertical ring spring (Sp1). If an additional suspension (S3) is used it has to be thoroughly guided so that it can only be combined with an inner axis as vertical guide (G2). Hence 16 combinations reduce to 6 versions. Sketches as for example shown in Figure 4.5.2 for the not recommendable combination S4 Sp5 G2 Co1 allow assessing the remaining combinations.

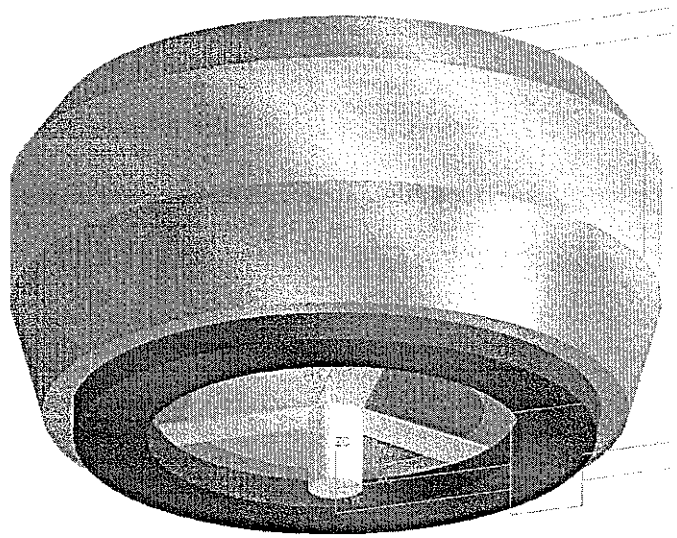

Figure 4.5.2a: *Sketch of not optimal version S4 Sp5 G2 Co1, bottom view*

Table 4.5.1 summarizes the results of a subjective evaluation and shows that only a combination of an additional suspension (S3), ring springs (Sp1), an axis as vertical guide (G2) and a complete housing (Co1), named version 1, seems to be acceptable. A sketch of version 1 is shown in Figure 4.5.3 and a more detailed dynamic FEA is presented in the following.

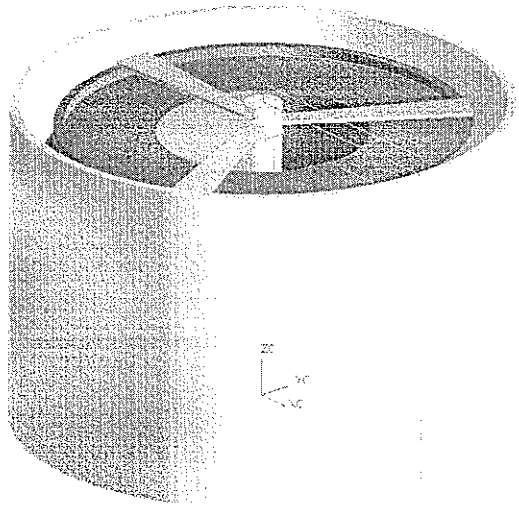

Figure 4.5.2b: *Sketch of not optimal version S4 Sp5 G2 Co1, top view*

Table 4.5.1: *Evaluation of possible design combinations, versions 1 to 6*

No	combination	evaluation	comment
1	S3 Sp1 G2 Co1	OK	no interference
2	S3 Sp1 G2 Co3	-	axis and moving inner cover interfere
3	S5 Sp8 G2 Co1	-	axis and inner spring interfere
4	S5 Sp8 G2 Co3	--	axis, inner spring and cover interfere
5	S5 Sp8 G4 Co1	-	inner spring and inner guide interfere
6	S5 Sp8 G4 Co3	--	inner spring, guide and cover interfere

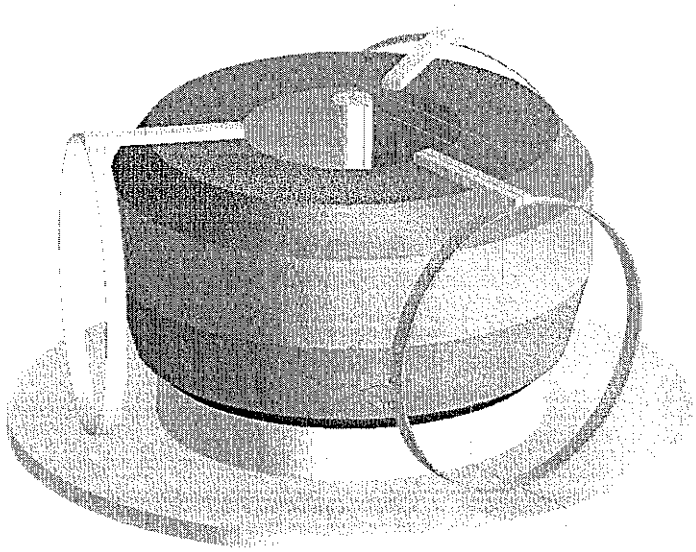

Figure 4.5.3: *Sketch of actuator version 1 (S3 Sp1 G2 Co1), complete housing not shown*

4.6 Mechanical design validation using FEA

The previous section has described the choice of the actuator shape depicted in Figure 4.5.3. After choosing appropriate dimensions a verification of the dynamic behaviour of the spring-mass system is carried out. Following Figure 4.1.2 a ring spring height of $2\times r$=0.015m gives the required stiffness at a stress in the material close to the yield strength of 340MPa with a safety of 10%. Since the chosen material CuSn6 is a ductile material slightly higher stresses do not lead to rupture, but to plastic deformation. Therefore they can be overloaded during a short time period. This spring height is also compatible to the total height of the magnetic circuit h=0.0114m implied by Table 3.5 and the desired stroke of d=0.001m. A horizontal distance of 0.5mm of the additional springs to the moving mass is considered to be sufficient. The ring springs could be soldered to the moving mass and clamped to the cover. Figure 4.6.1 shows the non-deformed (without finite element grid) and the simulated deformed shape (with finite element grid) at the first calculated natural frequency of 16.72Hz when it is assumed that there is an ideal stiff connection at the bottom of the ring springs to the ground and the inner axis does not constrain the movement to the vertical direction. The moving mass is modelled by 2-dimensional shell elements of thickness 0.0091m and material properties of steel. The ring springs are connected to the moving mass via 0.5mm thick beams also modelled as 2-dimensional shell elements. The ring springs are modelled as 0.1mm thick 2-dimensional shell elements with the material properties of phosphor bronze (CuSn6). The calculated natural frequency gives an upper limit due to a finite number of elements being used. 3-dimensional elements are not used since simulations results strongly depend on the number of elements. Figure 4.6.1. shows the importance of the guidance function of the axis that prevents the shown mode from being excited since it is desirable that the first mode is the vertical vibration mode of the moving mass on a spring with no horizontal displacement. Figure 4.6.2 shows the second mode shape at a frequency of 16.837Hz that also is not desirable since it is not the pure vertical mode. This mode could also be prevented from being excited constraining the inner edge of the moving mass in horizontal direction by using an internal axis.

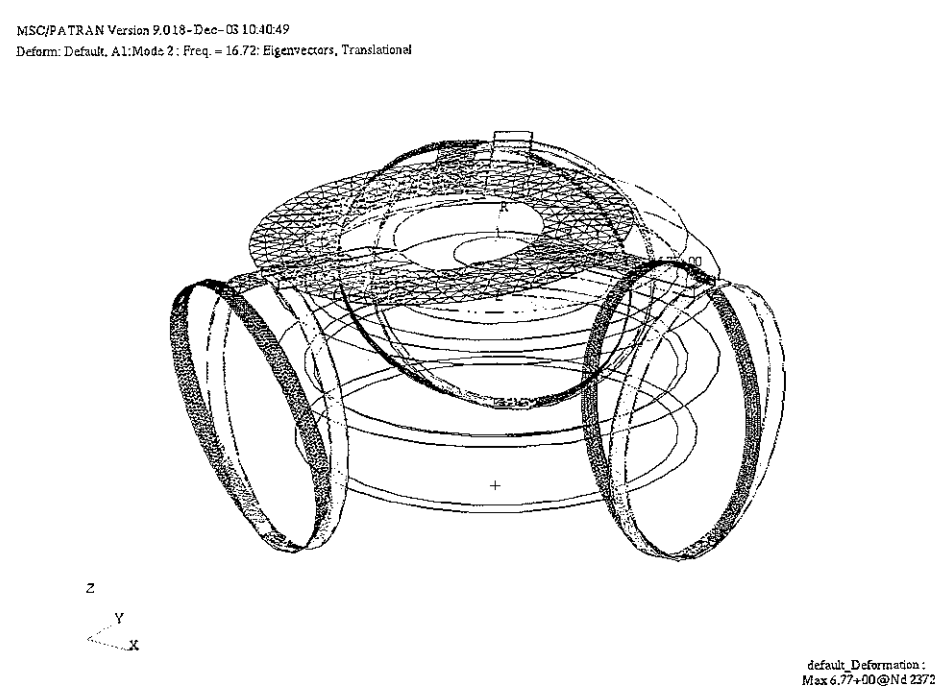

Figure 4.6.1: *1st simulated modal shape of the ring spring type actuator if centre is not constraint; dark: deformed shape; light: not deformed shape*

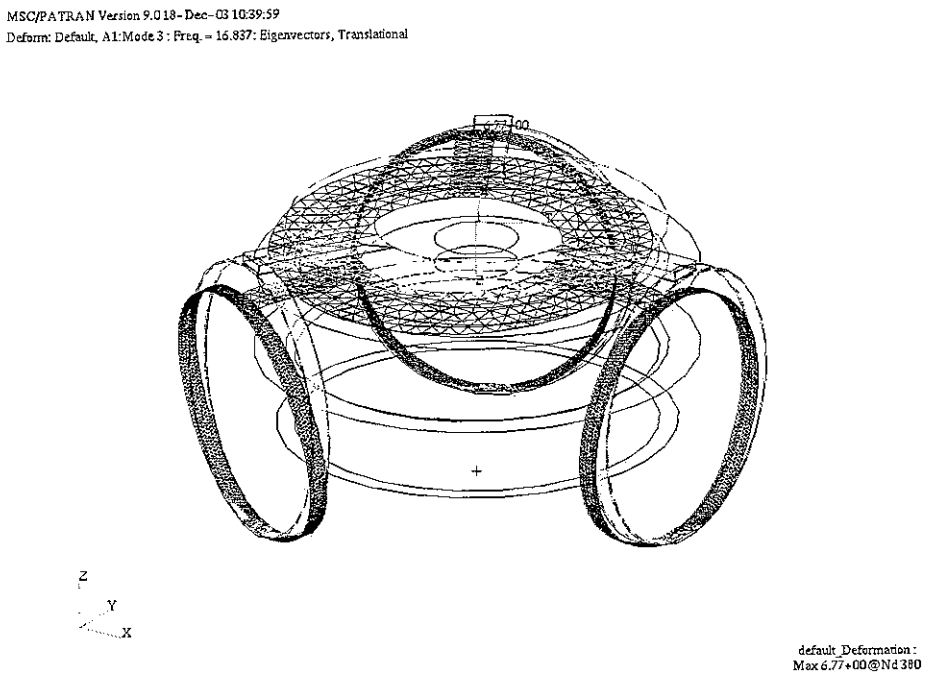

Figure 4.6.2: *2nd simulated modal shape of the ring spring type actuator if centre is not constraint; dark: deformed shape; light: not deformed shape*

Figure 4.6.3 shows the mode shape of the desired mode with only vertical displacement. With 29.806Hz it lies above the predicted 20Hz with stiffness values calculated with formulae from [77]. It is assumed that the difference is due to the boundary condition of the ring spring connection to the ground that is not a single element in the FEA; but it includes a number of elements so that stiffness is increased in the simulated model.

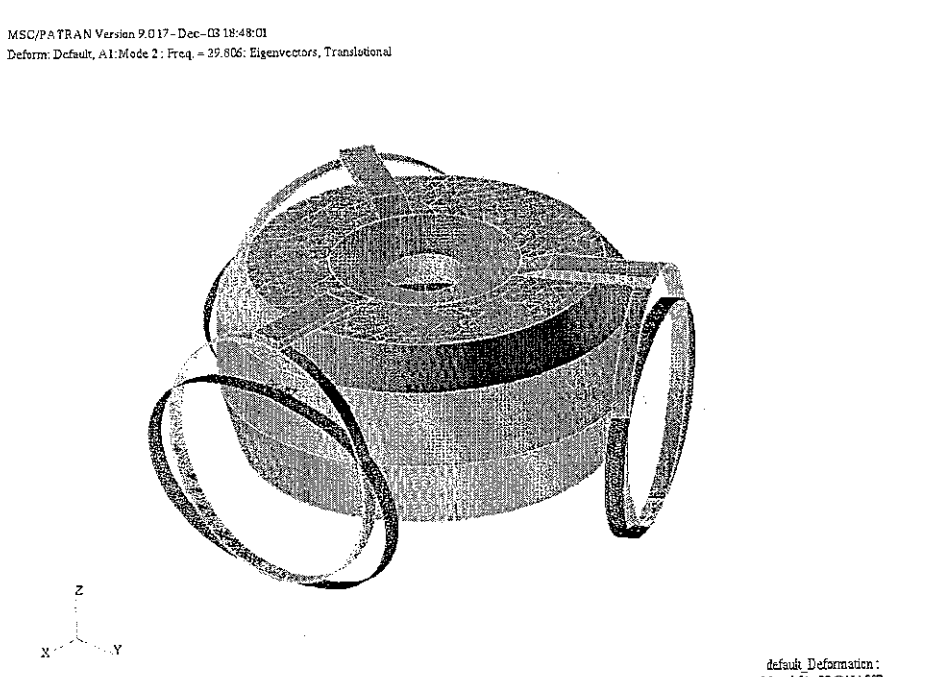

Figure 4.6.3: *3rd simulated modal shape of the ring spring type actuator if centre is not constraint or 1st natural frequency if centre is constraint to move in z direction ; dark: deformed shape; light: not deformed shape*

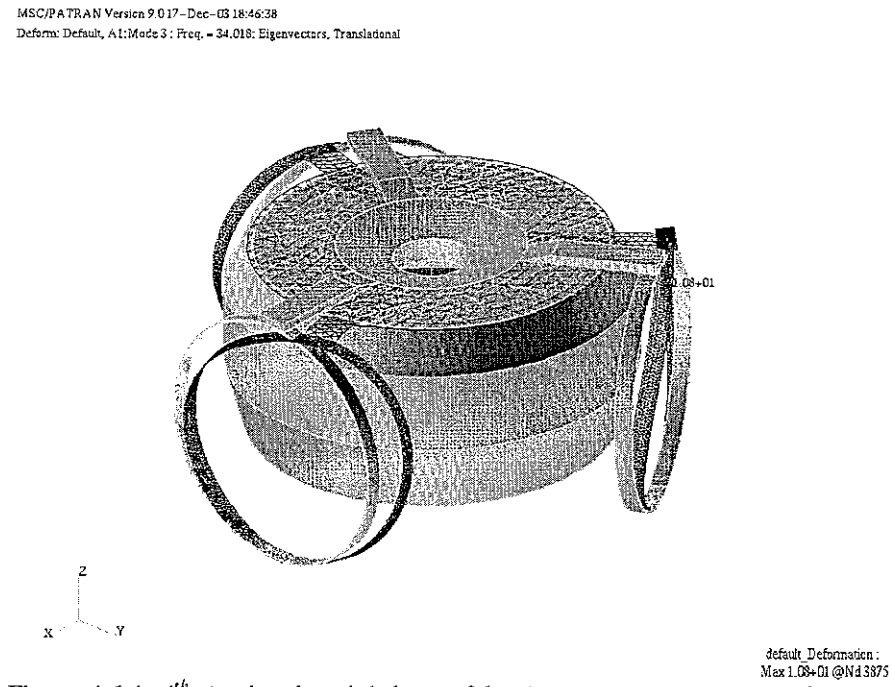

Figure 4.6.4: *4th simulated modal shape of the ring spring type actuator if centre is not constraint or 2nd mode shape if centre is constraint to move in z direction ; dark: deformed shape; light: not deformed shape*

The next higher 4th mode at about 34Hz whose mode shape is shown in Figure 4.6.4 is extremely problematic since it is a rotational mode around the vertical axis that should not be observable by the internal velocity sensor. Moreover it is also not prevented by an internal axis. Hence, it is hoped that this mode is not excited by a mere vertical disturbance of the actuator as is verified in Section 6. Figure 4.6.5 and 4.6.6 show mode shapes of higher order modes that probably can be prevented from being excited using an internal axis.

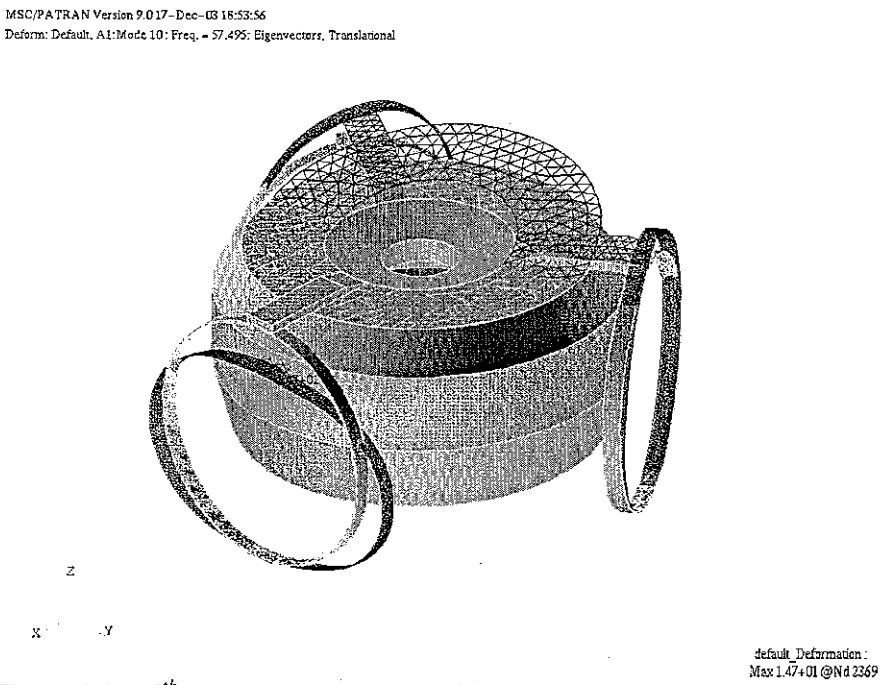

Figure 4.6.5: *5th simulated modal shape of the ring spring type actuator if centre is not constraint; dark: deformed shape; light: not deformed shape*

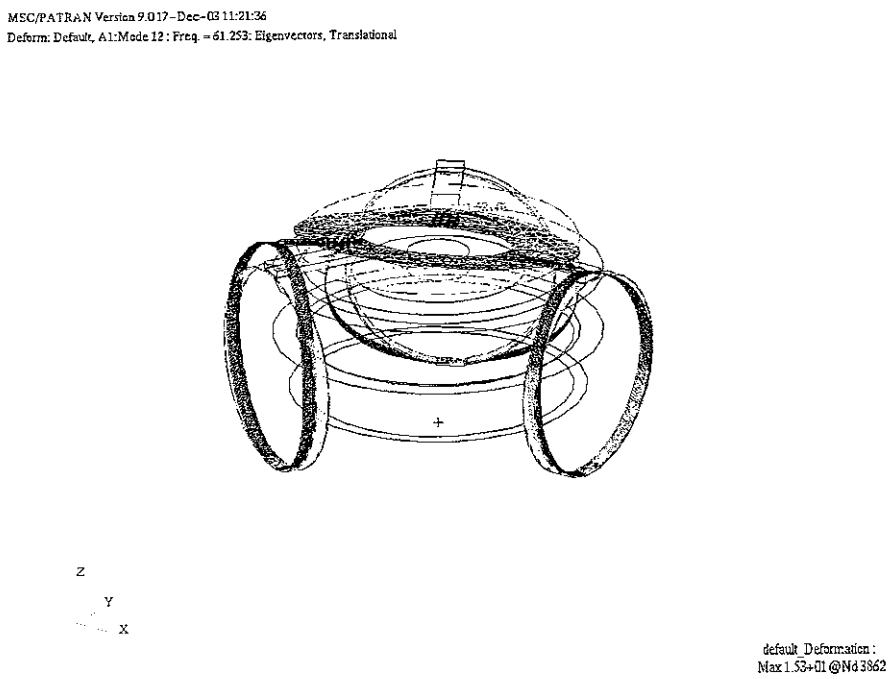

Figure 4.6.6: *6^{th} simulated natural frequency of the ring spring type actuator if centre is not constraint; dark: deformed shape; light: not deformed shape*

Figure 4.6.7 shows the mode shape of the lowest internal spring mode. In comparison to a FEA of a single ring spring alone mentioned in Table 4.1 these resonance frequencies appear at much higher frequencies beyond the bandwidth limit of 1kHz and should not play an important role due to the low weight of the ring springs. There are no resonance frequencies simulated in the frequency range from 62Hz to 1700 Hz so that a large frequency bandwidth without internal resonance frequencies is predicted for the actuator when the rotational modes can be prevented from being excited by using an internal axis. The pure vertical mode, depicted in Figure 4.6.3, and the rotational mode in Figure 4.6.4 should still be shifted to lower frequencies.

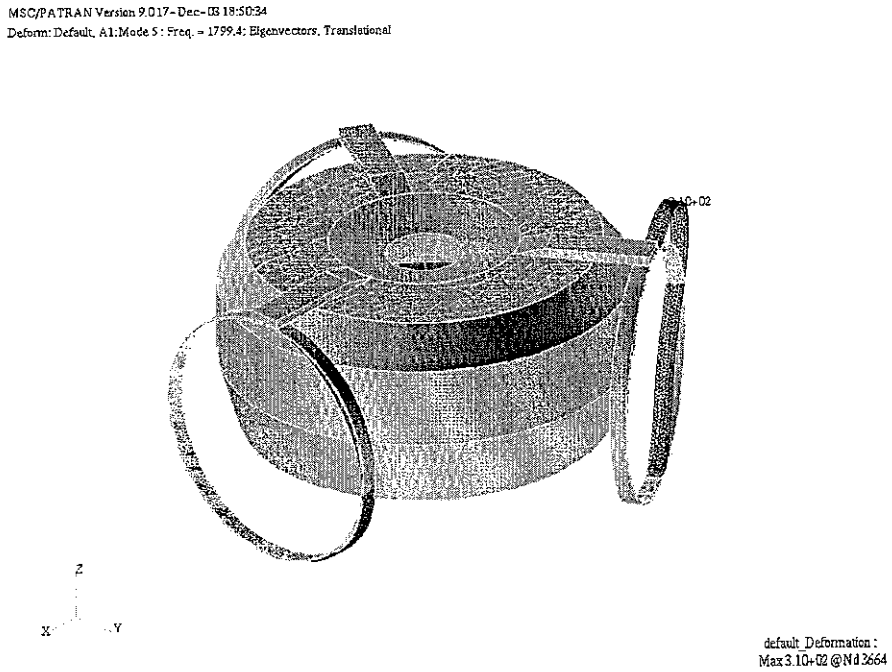

Figure 4.6.7: *7^{th} simulated modal shape of the ring spring type actuator if centre is not constraint or 3^{rd} mode shape if centre is constraint to move in z direction ; dark: deformed shape; light: not deformed shape*

One way to do this could be changing the boundary conditions of the ring springs to the ground. The following figures show mode shapes that are obtained by just connecting one element at the bottom of the ring springs to the ground and by preventing the elements inside the moving mass ring to move in radial direction. The ring springs are now modelled by 1mm thick elements of width 0.1mm. Figure 4.6.8 shows the mode shape of the first natural frequency at about 3.7Hz that now is the rotational mode around the vertical axis.

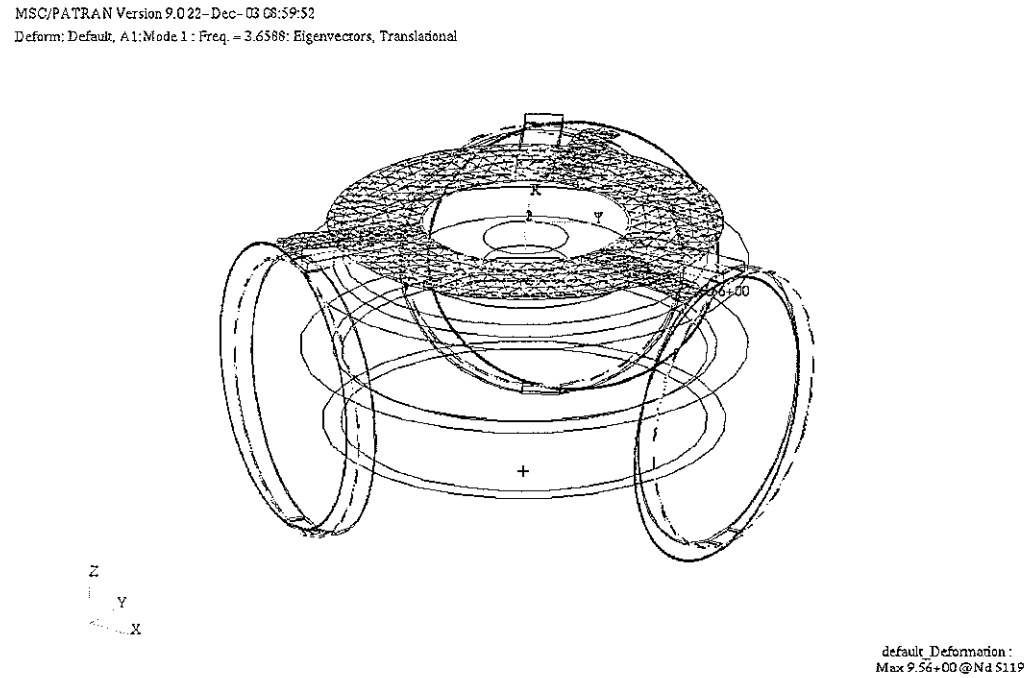

Figure 4.6.8: *1st simulated modal shape of the ring spring type actuator if centre is constraint and ring springs are weakly connected; dark: deformed shape; light: not deformed shape*

The second mode shape shown in Figure 4.6.9 that lies at about 25Hz is the desired vertical displacement mode. Its resonance frequency is reduced from about 30Hz and the rotational mode does not play a role any long due to its low frequency. Because of the obvious

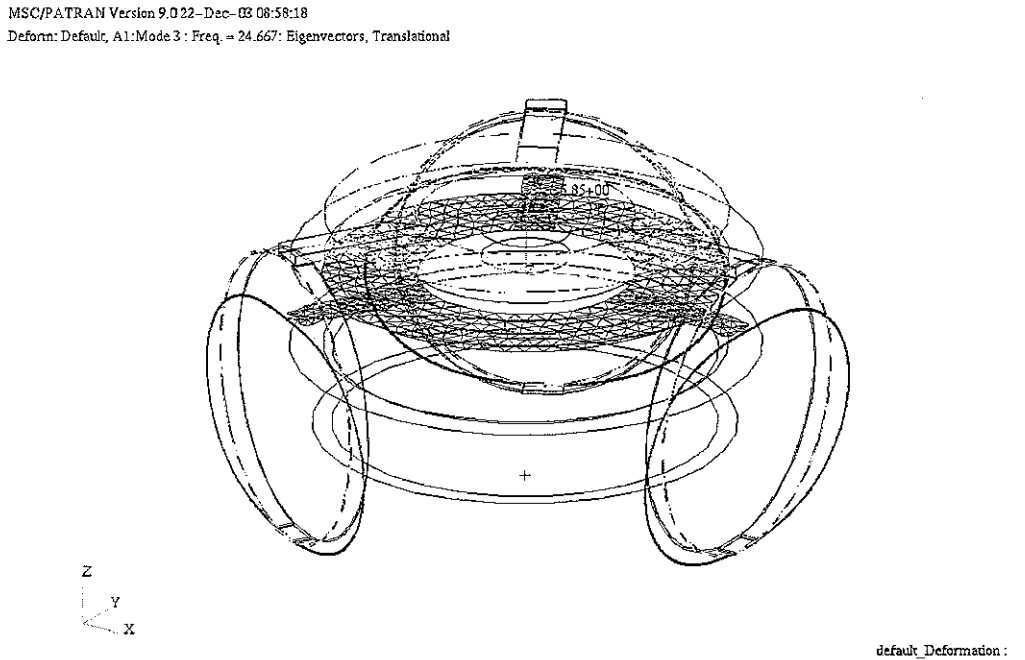

Figure 4.6.9: *2nd simulated modal shape of the ring spring type actuator if centre is constraint and ring springs are weakly connected; dark: deformed shape; light: not deformed shape*

importance of the boundary conditions at the connection point of the ring springs to the cover different designs of the ring clamps are realized (see two different drawings S-2 in the annex) in order to have an easy means to change the resonance frequency of the vertical mode. Figure 4.6.10 and Figure 4.6.11 show higher order mode shapes at internal spring resonance frequencies. They now lie within the bandwidth of 1kHz, but they are of small concern due to the small spring weight.

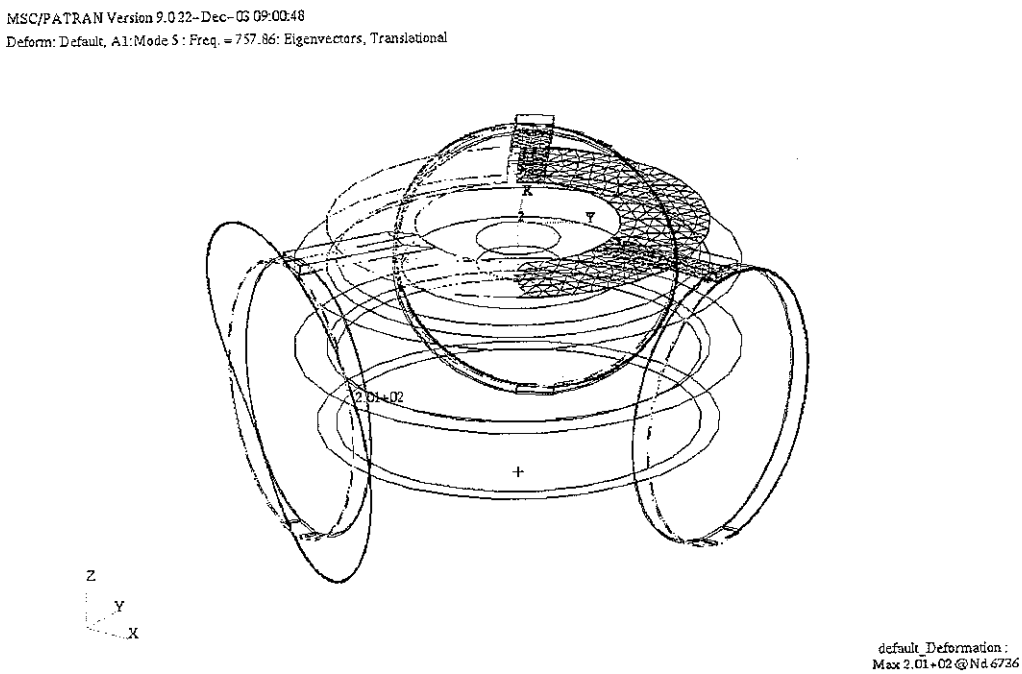

Figure 4.6.10: *3rd simulated modal shape of the ring spring type actuator if centre is constrain and ring springs are weakly connected; dark: deformed shape; light: not deformed shape*

The dynamic behaviour of the chosen design seems to be adequate so that manufacturing drawings that are compiled in the annex are drawn. The following section details procedures carried out and problems encountered during the manufacturing process.

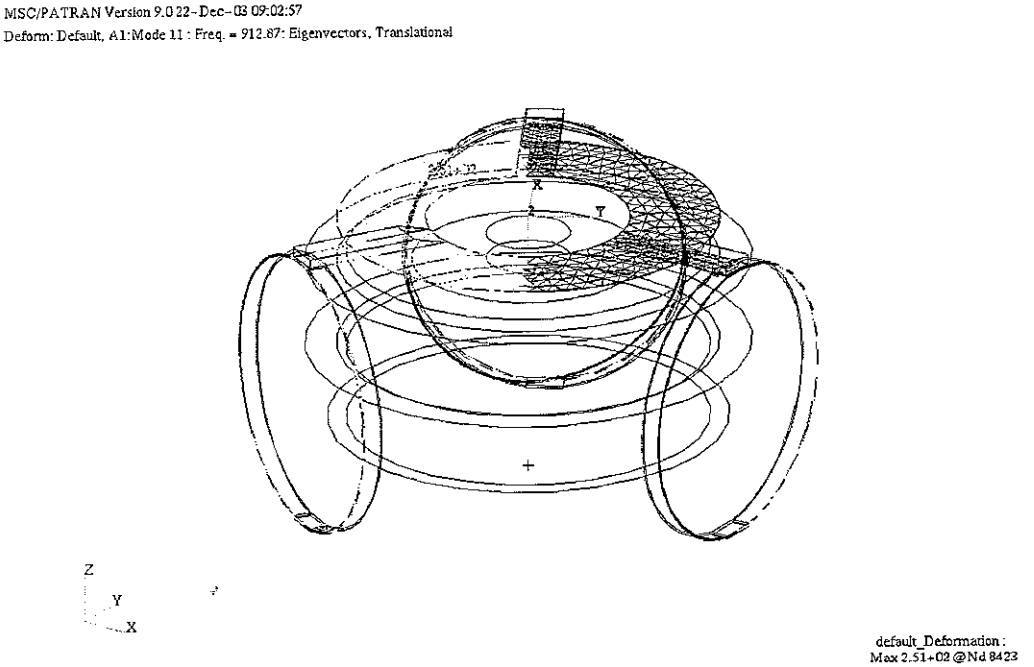

Figure 4.6.11: *6th simulated modal shape of the ring spring type actuator if centre is constraint and ring springs are weakly connected; dark: deformed shape; light: not deformed shape*

5. MANUFACTURING PROCESS

An exploded view of the actuator as result of the computer aided design (CAD) using findings from Section 4 and especially from Figure 4.5.3 is depicted in Figure 5.1.

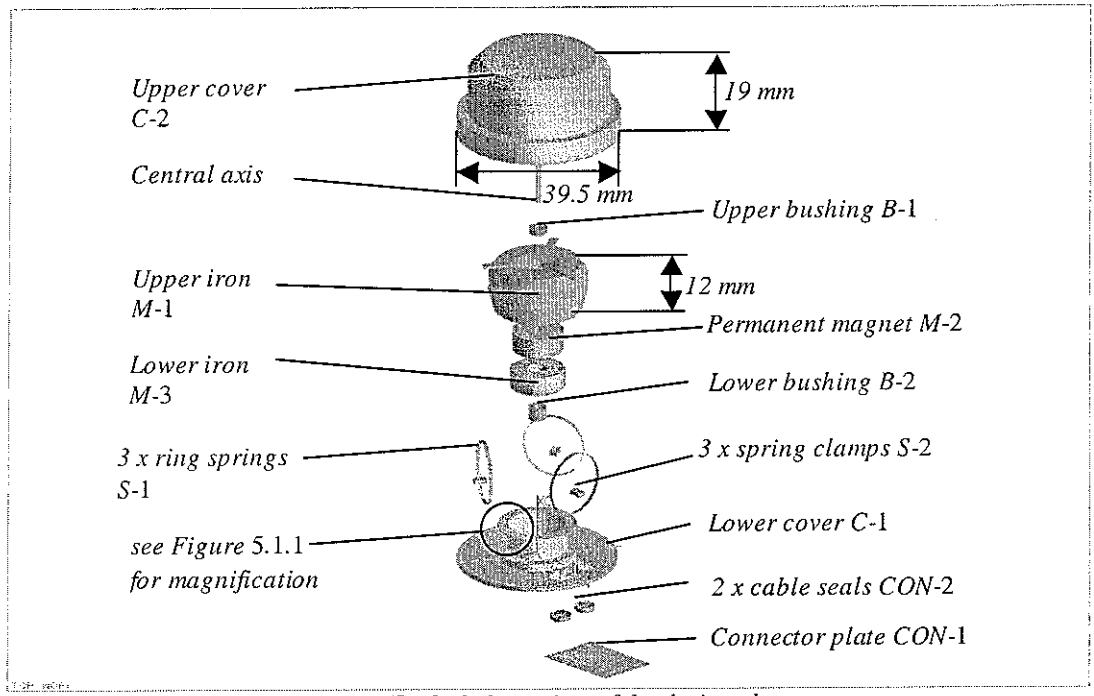

Figure 5.1a: *Exploded top view of the designed actuator*

This Section 5 illustrates the necessary steps and practical considerations in order to obtain a prototype starting from the CAD results. Detailed drawings of the actuator design are compiled in the annex. Manufacturing steps are illustrated with photographs. First tolerances have to be chosen adequately in order to fulfil functions. Second these tolerances necessitate

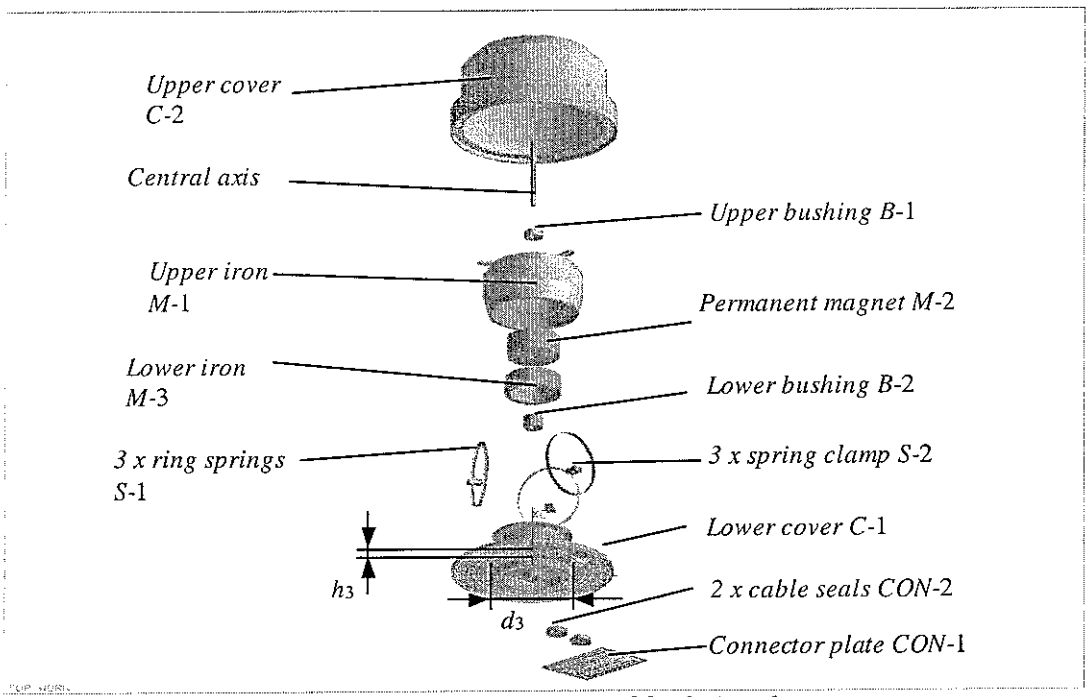

Figure 5.1b: *Exploded bottom view of the designed actuator*

special care during the manufacturing process so that for example special tools are manufactured for the machining of the cover. Third a special tool whose drawings are attached in the annex has been designed and manufactured in order to wind coils on a standard lathe. Special considerations are necessary in order to protect the small measurement wire from the big driving wire during this winding process. Fourth a device to form the ring springs is implemented that allows simultaneous forming and soldering of a ring spring to the moving mass. For the final assembly poly-tetra-fluor-ethane (PTFE) cylinders are machined in order to allow accurately centring the permanent magnet and the inner iron.

5.1. Tolerance

Special care is required for the design of the air gap since it directly affects performance. A maximum amount of copper is to be introduced in the air gap as presented in Section 4.4. Moreover a secondary coil is included. A former that transmits the actuation force to the connected structure carries the two coils and is integrated into the additional lower cover. Since an axis is used that closely guides the former in the air gap small air gap tolerances can be chosen. However, due to the uncertainties of the winding process the final shape of the air gap is reached by a final machining described in Section 5.5. Figure 5.1.1 shows the dimensions and chosen tolerances in horizontal direction so that the driving coil with 18x8 wires and a coil diameter of 0.315mm and the measurement coil with 2x38 wires and a coil diameter of 0.052mm fit into the air gap. A minimum former thickness of 0.1mm is provided that is estimated to be the lower limit that can be machined with a common lathe. The measurement coil is in a gap below the driving coil so that it is centred, protected from the driving coil and it has the smallest diameter possible for a small coupling effect as illustrated by Equation 4.4.7.

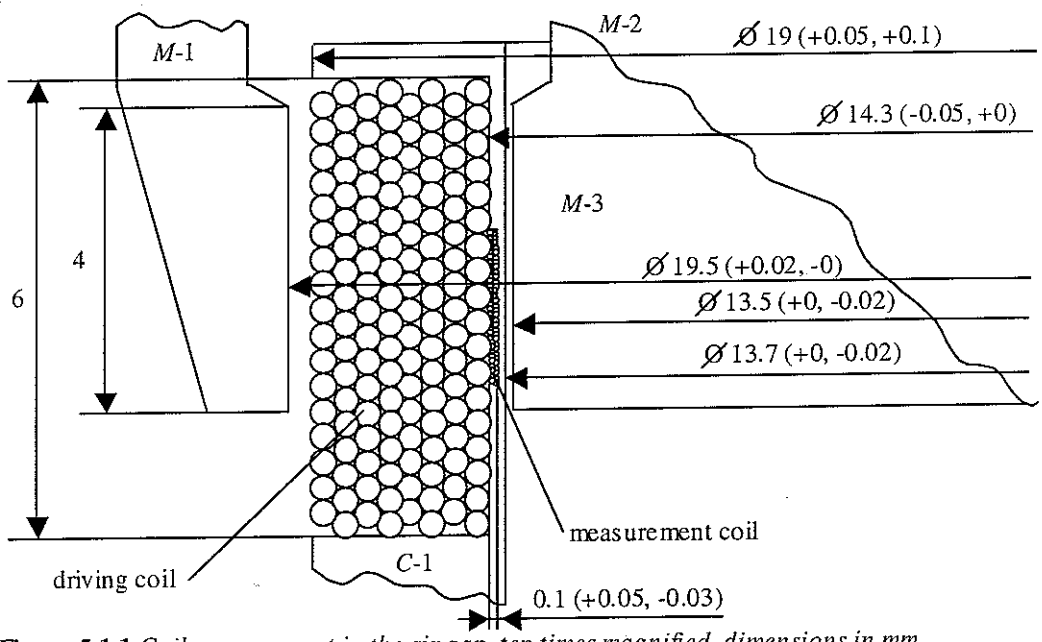

Figure 5.1.1 *Coil arrangement in the air gap, ten times magnified, dimensions in mm*

An ISO 2228 stainless steel pin that is used as the guiding axis has a manufacturing tolerance of 1.5 m6 (+0.002, +0.009). For simplicity it is pressed in the lower cover and guided in the upper cover. In order to be able to easily press it a hole of 1.5 (+0.002, +0.009) is used. For guidance in the upper cover a hole of 1.5 (+0.01, +0) is foreseen. Both holes have an active

surface until a depth of 1.5mm so that a pin of length 16mm fits between the two covers as can be seen from drawings *C*-1 and *C*-2. If demounting of the upper cover is required the upper hole can pierce the upper cover.

On their inner side the bushings guide the axis of 1.5m6 so that a tolerance of 1.5 (+0.028, +0.015) is used. On the outer side they are press fitted into the iron of the magnetic circuit (*M*-1 or *M*-3) so that a tolerance of 4.5 (+0.01, +0.004) is chosen. Additionally in order to be able to easily mount the bushings well centred they should have an area of depth 0.3mm with a tolerance of 4.5 (+0, -0.01) at the outer diameter. In order to guarantee a stable fit of the bushings in the iron a low viscosity epoxy glue can additionally be applied.

The lower and the upper cover should well fit together so that no small particles can penetrate into the housing. Then additionally easy centring results. A tolerance of 38.5 (+0.01, +0) is foreseen on the upper cover and a tolerance of 38.5 (+0,-0.01) on the lower cover.

Two Teflon (PTFE) parts are used to guide measurement and driving coil wires through the lower cover to the outside. PTFE is chosen because of its surface properties so that the wires are not damaged. The Teflon parts (CON-2) are to be press-fitted into the lower cover resulting in a tolerance of 5 (+0.016, +0.008) on the outer diameter of CON-2 and a tolerance of 5 (+0.012, -0) on the inner diameter of the holes in the lower cover.

5.2. Cover

Because of the tight tolerances and the thin wall thickness of the former as is illustrated in Figure 5.1.1 special care is required for manufacturing. Figure 5.2.1 shows the lower cover part *C*-1 during machining of the small groove for the measurement wire. The part is clamped on the left hand side in the chuck of a lathe. The PTFE cylinder on the right hand side is used to clamp the part when the clamping cylinder on the left hand side is removed once the coil is wound. It also stabilizes the cylinder with 0.1mm wall thickness during machining of the groove for the measurement wire and during winding of the coil. Once the coil is wound and glued the former itself should have sufficient stability on its own.

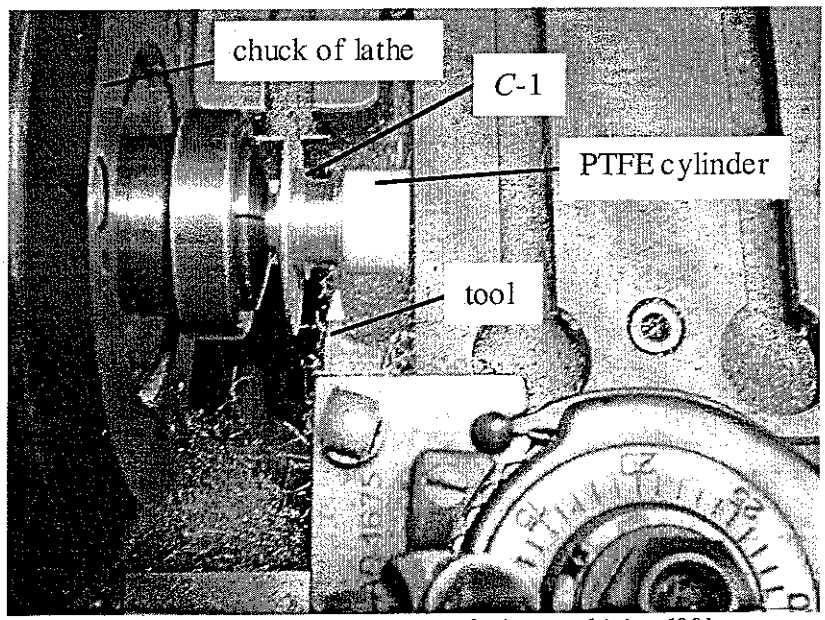

Figure 5.2.1: *Lower cover part during machining [80]*

Figure 5.2.2 shows a selection of tools that are manufactured to drill the hole for press fitting the axis into the lower cover and the hole in the upper cover to guide the axis. A DIN 6325 steel pin of length 32mm is ground to the required dimensions. The aluminium cylinder in Figure 5.2.2 is used to guide the tool horizontally and one of the tools is actually used to machine the guiding hole in the aluminium cylinder.

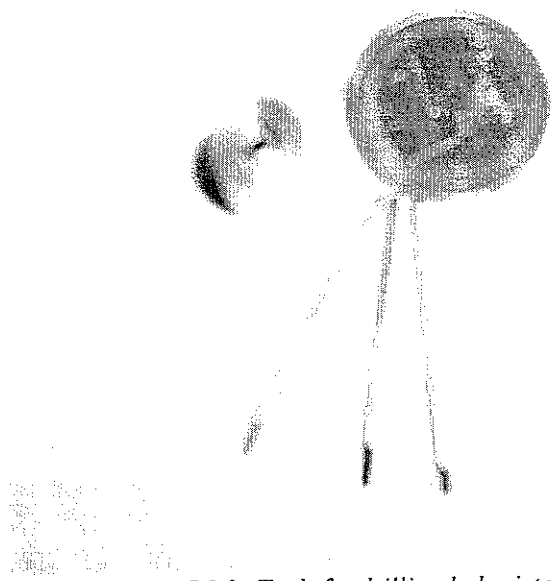

Figure 5.2.2: *Tools for drilling holes into the lower cover*

Figure 5.2.3 shows the boring of the diameter 5 holes in the lower cover *C*-1 in which the two *CON*-2 parts are press-fitted. Alternatively a special Teflon cylindrical part is used to hold the lower cover part so that the 0.3mm holes for the wire outlet can be drilled into the press-fitted *CON*-2 parts. Figure 5.2.4 shows the procedure to drill the six diameter 1.2mm holes at 60 degrees distance that is also used to drill the M1 threads into the upper cover. A special disk with graduation shown in Figure 5.2.5 is used to determine the exact 60 degrees distance.

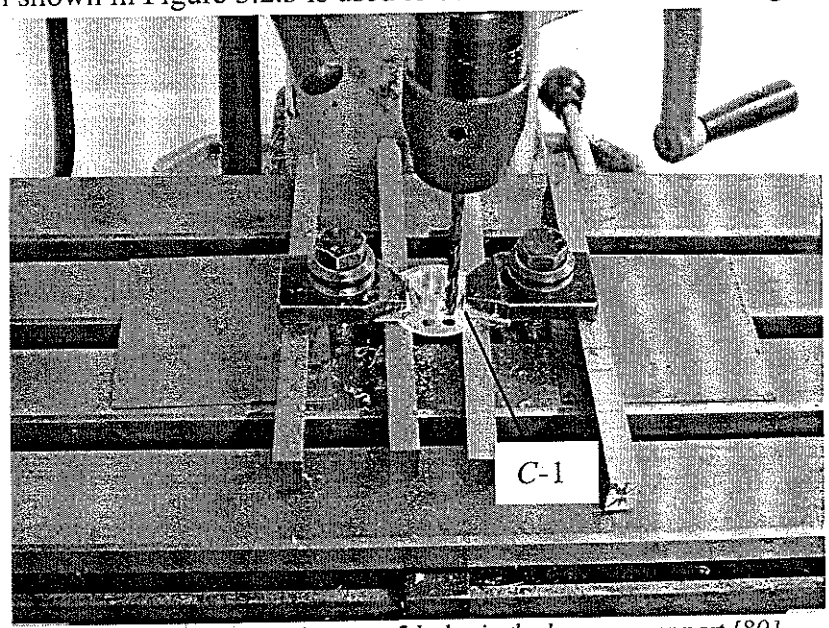

Figure 5.2.3: *Boring diameter 5 holes in the lower cover part [80]*

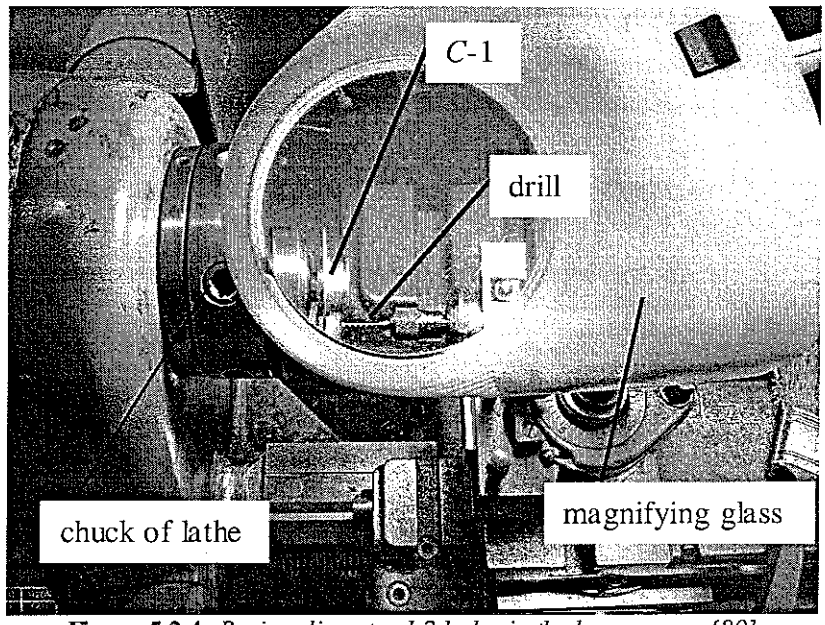

Figure 5.2.4: *Boring diameter 1.2 holes in the lower cover [80]*

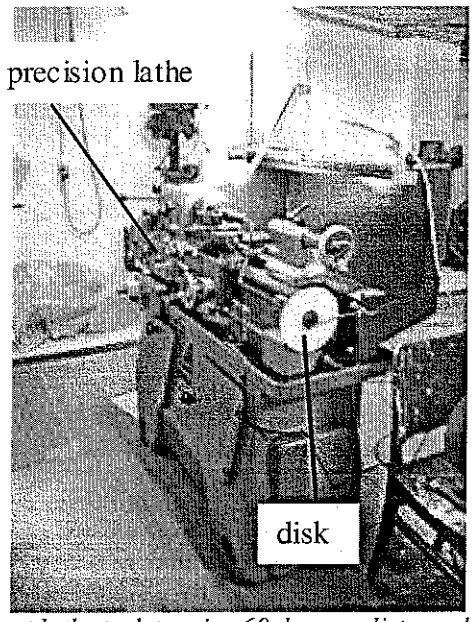

Figure 5.2.5: *Disk at lathe to determine 60 degrees distance between holes [80]*

5.3. Coil winding

In order to be able to wind coils on a common lathe a special coil-winding device depicted in Figure 5.3.1 with drawings in the annex has been designed and built. The screw is used to adjust the friction force and hence the tension in the coil wire during winding so that there is limited control over the density of the coil package. A soft Teflon inlet with minimum friction is used to guide the wire.

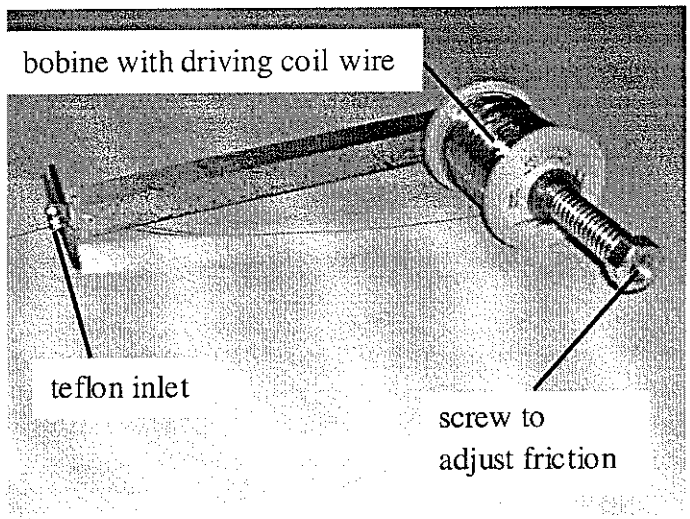

Figure 5.3.1: *Coil winding device to be used at a common lathe*

The coil winding is first carried out at a test part with the same dimensions as the former of the lower cover part in order to determine practical problems during the procedure and acquire the necessary skills. The same part is also used to approximately determine the coil coupling without influence of the magnetic circuit in Section 6.3. Figure 5.3.2 shows the test part during winding of the driving coil. A plastic stick can be used to increase the density of the coil package when it is wound manually. For more than four layers winding by turning the lathe chunk manually instead of using the lathe advance at very low speeds is recommended because it allows easier control of crossing wires. Wires should not cross in order to prevent compensation of the driving magnetic field during operation.

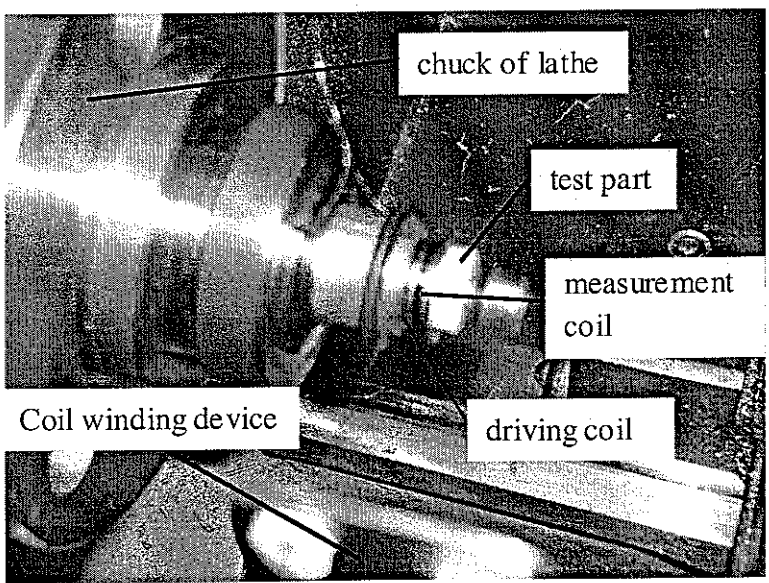

Figure 5.3.2: *Winding of the driving coil at a test part*

During the test winding it has been found out that the big wire of the driving coil damages the tiny wire of the measurement coil as is shown in Figure 5.3.3. Therefore grooves are machined in part *C*-1 with an electro discharge machine (EDM) as depicted in Figure 5.3.4

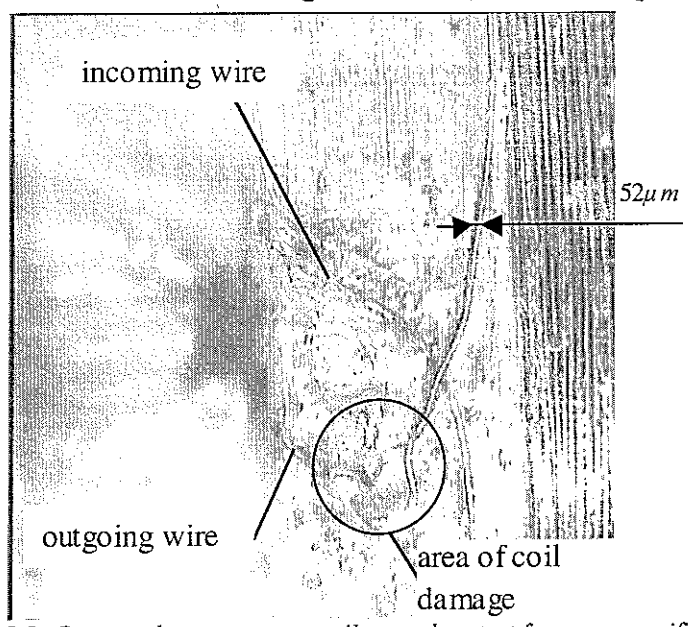

Figure 5.3.3: *Damaged measurement coil wound on test former, magnified by light microscope*

that allow protecting the small wire. These grooves are not included in drawing *C*-1. Additionally before winding the big wire the small wire is wound and glued into the main groove with two connecting ends sticking out at a length of about 0.1m each. Then those two ends are put into the grooves for additional protection and glued again so that the used low viscosity epoxy glue (see data sheet in the annex) provides additional protection. The procedure is repeated on the real part. After having wound and glued the big wire of the driving coil, where some drops of the glue are sufficient, the ends are soldered to 0.3mm diameter metal pins that pierce the Teflon parts. In order to be able to solder the measurement wire its insulation is to be etched away. Salicylic acid generated by an Aspirin® when exposed to the 350° C of a soldering iron is a convenient etching agent.

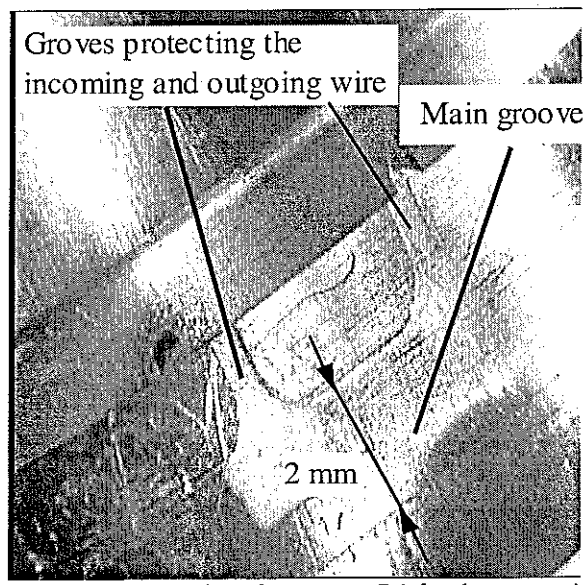

Figure 5.3.4: *Grooves machined into part C-1 for the protection of the measurement wire, magnified by light microscope*

5.4. Ring springs

Bronze strips are manufactured using a wire electro discharge machine (wire-EDM). Special care is to be taken to correctly choose manufacturing parameters and to ensure good positioning of the raw material that is clamped between two 1mm aluminium plates. That way manufacturing errors due to vibrating raw material as depicted in Figure 5.4.1 are avoided.

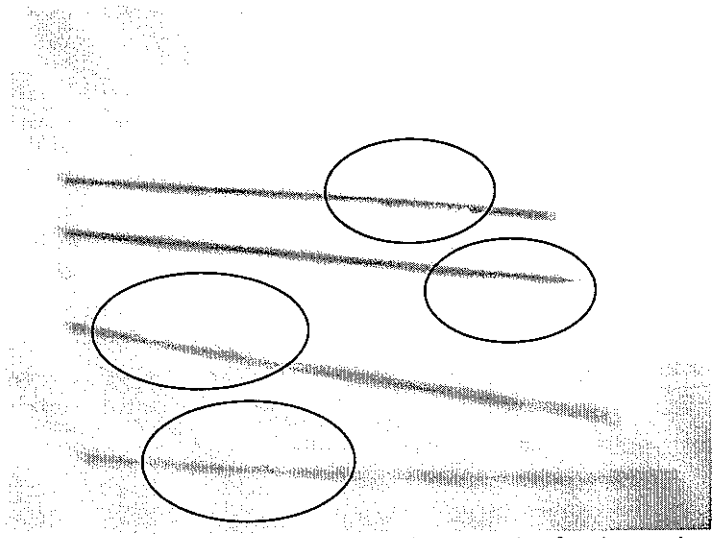

Figure 5.4.1: *Manufacturing error at bronze strips for ring spring*

Alternatively strips can also be manufactured with common manual cutting tools. This is the only manufacturing option if another material like DIN 17222 Ck101 spring steel is chosen in order to profit from the increased yield strength. In addition to an increased safety factor the dynamic behaviour of steel parts is more widely known than the one of bronze parts. Figure 5.4.2 gives the maximum allowable stress σ_H in a DIN2093 steel with E_{st}=206×10^9*Pa* at N load cycles and lower stress σ_u as well as peak stress σ_o. Three ring springs should statically support the moving mass resulting in a static moment [77]

$$M_{st}=0.318\times r\times M/3\times 9.81\text{m/s}^2=1.6\times10^{-4}\text{Nm} \tag{5.4.1}$$

in a single ring spring. In order for the resulting static stress to be smaller than R_m/S_{st} where R_m=*640*MPa is the yield strength of the material and S_{st}=1.5 is a safety factor from [81] the spring width is to be chosen to be superior to

$$b_{sp} \geq \frac{M_{st}6}{h^2 S_s R_m}=7.6\times10^{-4}\text{m}, \tag{5.4.2}$$

where h=0.06mm is the available material thickness. Moreover the ring spring stiffness given by [77] is equal to the required stiffness K from Section 4.1. if

$$b_{sp}=\frac{KR^3 9}{5h^3 E_{st}}=17.96\times10^{-4}\text{m}, \tag{5.4.3}$$

so that a spring width b_{sp}=1.8mm is chosen. At this spring width a dynamic moment

$$M_d=0.318\times K\times 2\times d\times r=5\times 10^{-4}\text{Nm} \quad (5.4.4)$$

with the required stroke d from Section 4.6 leads to a dynamic stress σ_d=464.9MPa. Together with the static stress and a safety factor S_d it should be smaller than the maximum allowable stress $\sigma_H(\sigma_u)$=700MPa from Figure 5.4.2 at the lower stress $\sigma_u=\sigma_{st}-\sigma_d/2$=-88.05MPa. For the chosen spring width a theoretical safety factor S_d=1.5 is realized that is a reasonable value for bending load [81]. However, these calculations are just approximate since the required dimensions can only be realized approximately due to the manual production process. Bronze springs should be used when material failure is not critical, but the influence on the magnet field is important. Steel springs can be more reliably designed against dynamic failure except if stress peaks occur at discontinuities, but they still are influenced by the magnetic field.

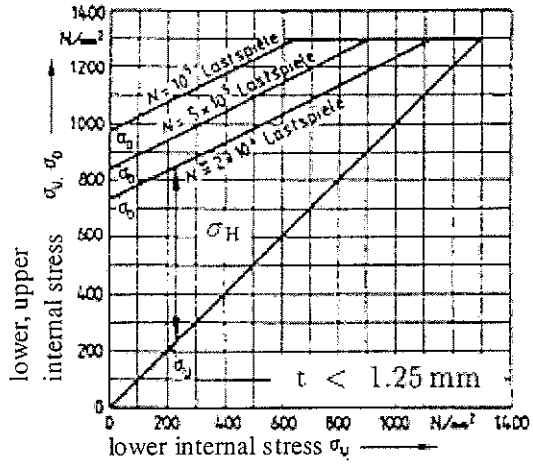

Figure 5.4.2: *Resistance against dynamic failure for spring steel following DIN 2093[81], No of cycles N*

The metal strips, either phosphor bronze or spring steel, are bent to ring springs using a special forming tool that is manufactured with close tolerances. It consists of an inner cylinder of diameter 15 (0,-0.1)with a groove to carry the 1mm x 0.1mm and 50mm long metal strip and an outer hollow cylinder of diameter 15 (+0.1, 0) that presses the metal strip into the groove as is depicted in Figure 5.4.3. A small groove is filed into the outer cylinder so that the ends of the metal strip may overlap for better soldering. While being clamped in this tool the ring springs are soldered one after the other to the moving mass piece using soldering fat. A circular shape of the ring springs results as is shown in Section 5.5.

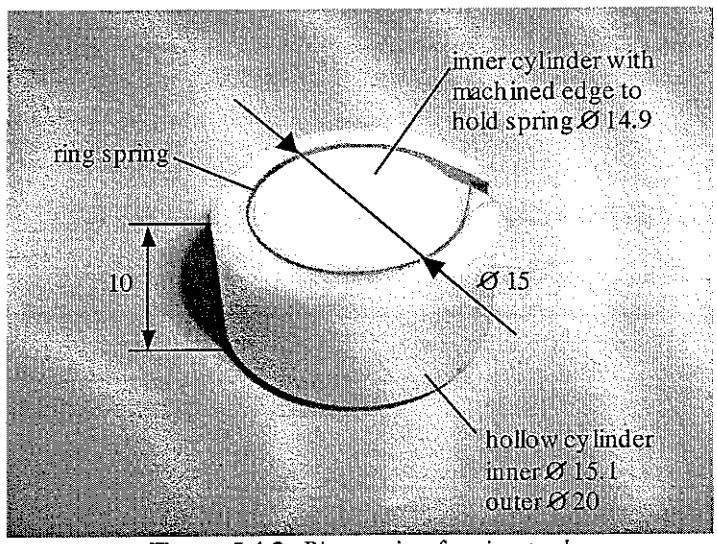

Figure 5.4.3: *Ring spring forming tool*

5.5. Assembly

The order of necessary assembly steps is illustrated in Figure 5.5.1 starting with the machining of all parts.

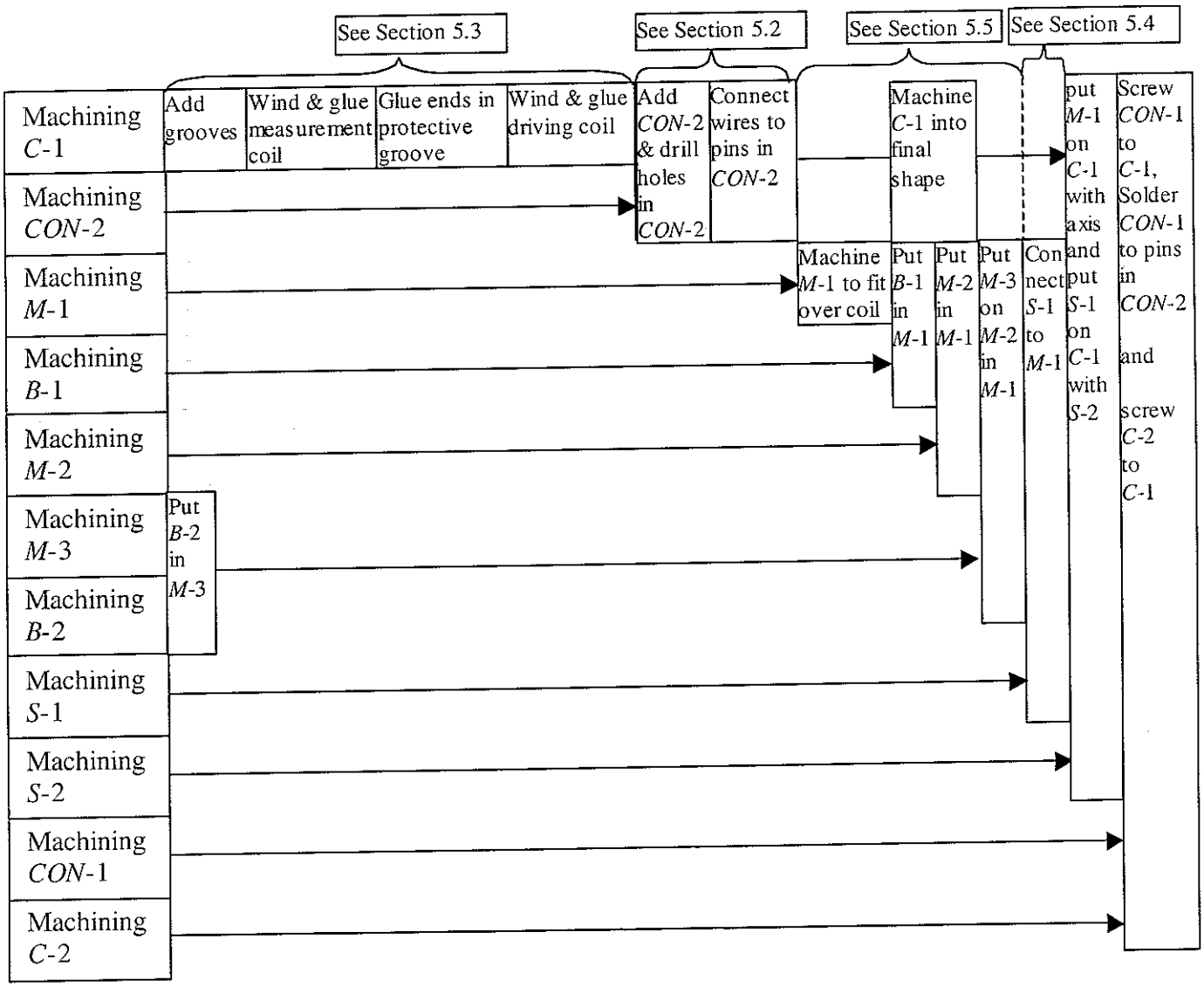

Figure 5.5.1: *Actuator assembly*

After winding the two coils, fixing them with low-viscosity epoxy glue and connecting them to the metal pins in the wire outlet the interior of the moving mass part M-1 is machined so that it fits over the wound coil. Since the winding process does not allow very dense packages for more than about four layers the air gap is to be widened considerably. A clamping tool depicted in Figure 5.5.2 is built so that the part M-1 may be clamped into the chunk of a lathe. The inner diameter forming the outer part of the air gap is widened from diameter 19.5 to diameter 19.9 to fit over the coil with a small gap. Then the bushings B-1 and B-2 are mounted into the parts M-1 and M-3 by press fitting with the smaller outer diameter of parts B-1 and B-2 going first. In order to mount the permanent magnet M-2 and the iron M-3 a hollow cylindrical PTFE mounting device with close tolerances is machined for each of the parts. M-2 is connected to M-1 as depicted in Figure 5.5.3 with a small layer of glue that also

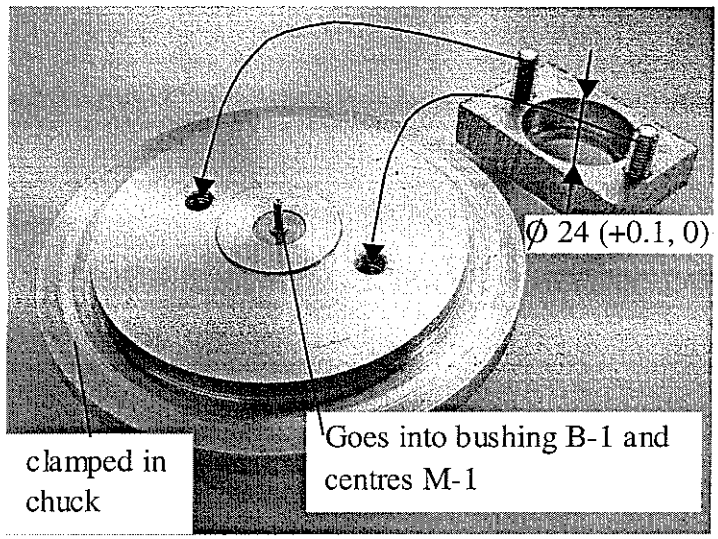

Figure 5.5.2: *Clamping tool to allow machining of part M-1*

serves as heat insulator. After hardening the glue part M-3 is mounted on and glued to M-2. The axis is used to align parts M-1 and M-3 before the glue is hardened. Then the three ring springs are soldered to M-1 using the ring spring forming tool. Before clamping the ring springs to the lower cover and adding the moving mass assembly together with the guiding axis the lower cover is brought into its final shape by removing the clamping cylinder on its bottom side and the PTFE cylinder on its upper side. During removal of the PTFE cylinder using its internal thread care is to be taken to not damage the 0.1mm thick former supporting the coils. The final lower cover and the moving mass are depicted in Figure 5.5.4.

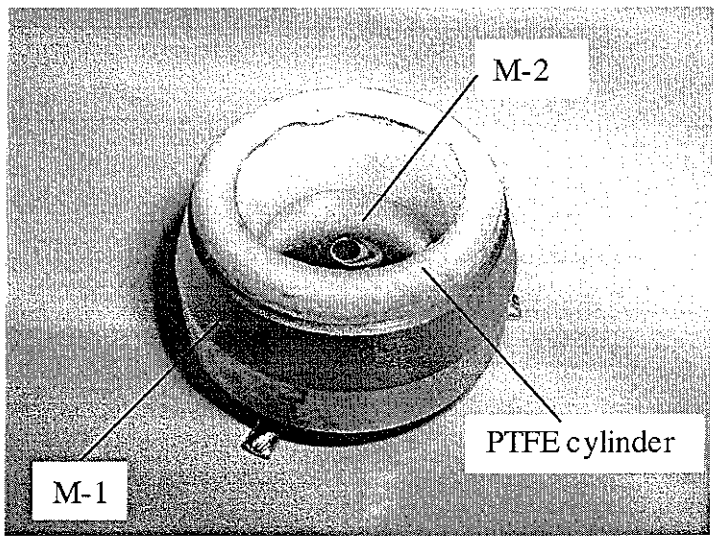

Figure 5.5.3: *Mounting M-2 in M-1*

The ring spring clamps are screwed to the lower cover and depending on the chosen clamp version they either clamp the ring springs or ring springs are soldered to them. Because of the small dimensions soldering ring springs to the clamp does actually provide a larger connecting surface than just clamping the ring springs to the lower cover. Therefore only the clamping version of S-2 is retained. Potentially point laser welding could allow a minimum contact area between the ring springs *S*-1 and the lower cover *C*-1. Finally the upper cover is added. The actuator as depicted in Figure 5.5.4 without upper cover is ready for performance checks described in the following Section 6.

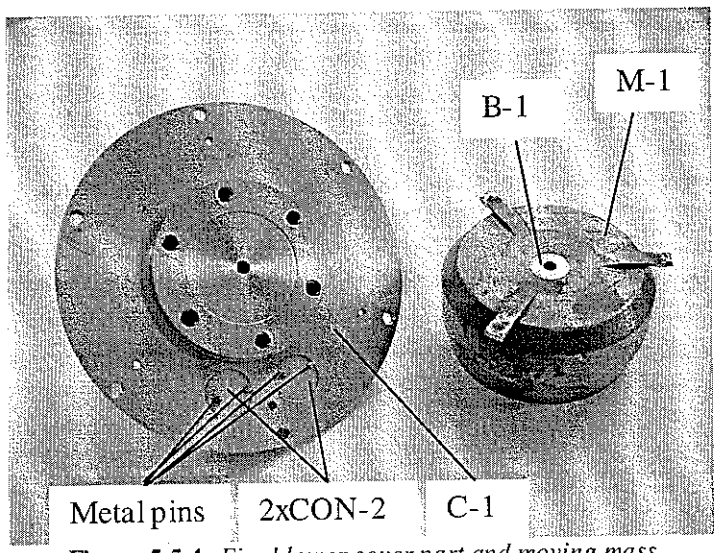

Figure 5.5.4: *Final lower cover part and moving mass*

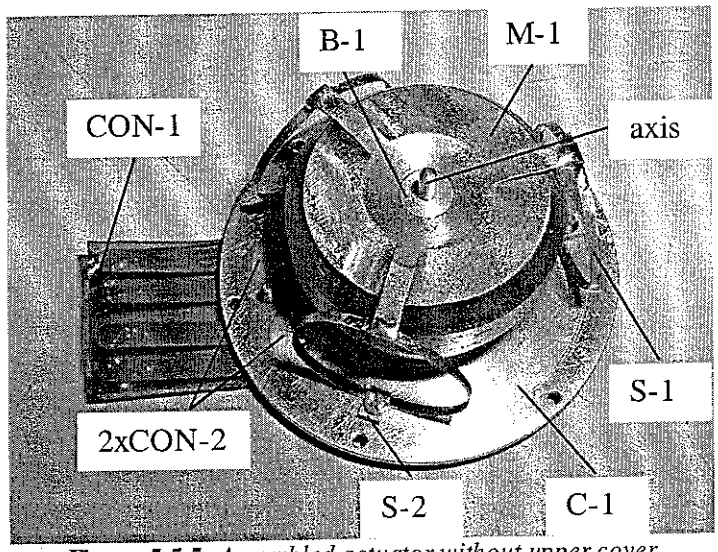

Figure 5.5.5: *Assembled actuator without upper cover*

6. VALIDATION

In this section the maximum performance of the actuator prototype is estimated and its dynamical behaviour is characterised. In particular the maximum power input, internal resonance frequencies and ways to estimate the vibration velocity of the moving mass relative to a connected structure are investigated. The aim is to use feedback of a velocity related signal to add damping to an internal resonance frequency until a certain frequency. An electronic circuit is proposed in order to include resonance frequencies of an attached structure in this bandwidth. Limits to this approach are mentioned.

6.1. Maximum power input

In order to measure the maximum electric power input the actuator is placed into a closed box to minimize the influence of the environment. A DC voltage is applied to the actuator so that the reactive mass does not move from a reached equilibrium position. Therefore no induced voltage disturbs measurements. A voltmeter V and an ammeter A as illustrated in Figure 6.1 measure voltage and current. The product of voltage and current gives the input power and the ratio of voltage and current gives the internal resistance R_0 of the actuator at DC. When higher power values are input into the actuator it is heated up by ΔT and as a result the value of the resistance changes by

$$\Delta R = R_0 \alpha_{20} \Delta T \,, \tag{6.1}$$

where R_0=1.68Ω is the resistance at 20°C and α_{20}=4.3×10^{-3}1/K is the linear temperature coefficient of the specific resistance of copper from [66].

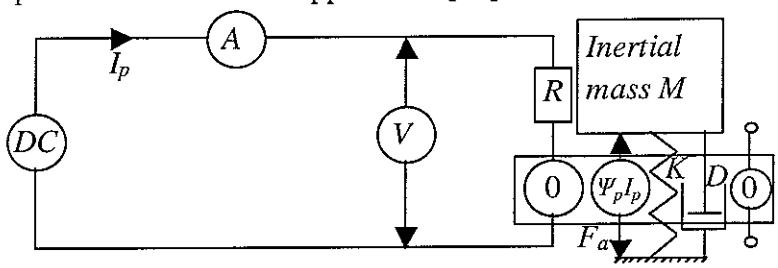

Figure 6.1.1: *Setup for input power measurements*

Thus by measuring the increase in resistance the temperature increase is determined. Measurements are carried out for several DC voltage i.e. power inputs and temperature increase vs. power input results are compiled in Figure 6.1.2. A line extrapolates the measurement points (circles) for which an increase in temperature is measured. Different points at a similar power input indicate that even when having waited over an hour until a stabilisation of the voltage and current small changes are possible. This is due to the influence of the environment that could not completely be eliminated. In particular only small differences in the temperature of the environment lead to a different 0K position as is shown by measurement points marked with a cross and a dot in Figure 6.1.2. Assuming an environmental temperature of 20°C an increase by about 60K in the wire is acceptable since the supplier of the permanent magnet material gives a temperature limit of 80°C. Hence, a maximum input power of 2.2 Watts at an input current of 1.1A is predicted. Higher temperatures are possible with reversible change of the demagnetisation line to lower H values since the knee of the demagnetisation curve of the permanent magnet lies at negative B

values as described in Section 2.1. An ultimate limit with reduction of the static magnetic field in the air gap is given by the melting temperature of the wire insulation at 155°C leading to an ultimate power input limit of about 4.7Watts or a current input limit of 1.33A. This is below the easy to implement 2A mentioned in Section 4.4.

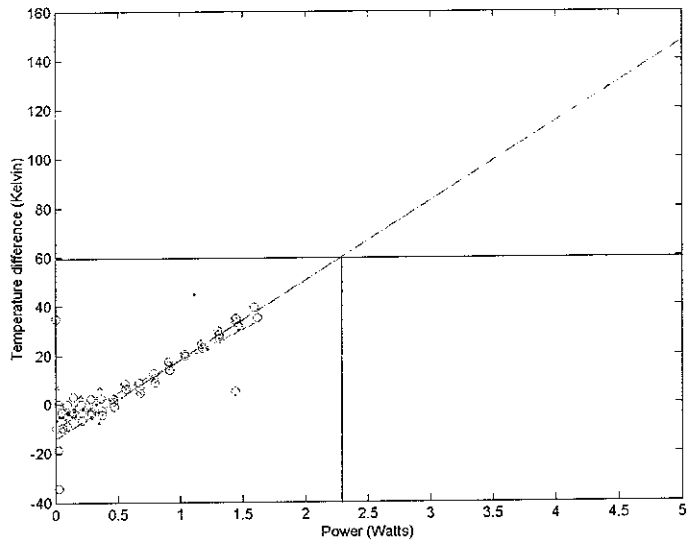

Figure 6.1.2: *Measured (o) and extrapolated (-) temperature increase of the driving coil for different DC current power inputs*

Adding a known weight on top of the moving mass and increasing the coil current until the top mass moves to an equilibrium position allows determining the transducer coefficient of the primary driving coil. The measurement is carried out for several current inputs from 0A to the 1A close to the current limit since the current at the equilibrium position is difficult to find with just one measurement. The average transducer coefficient is found to be 2.52 N/A where a maximum mass of 247g is lifted to an equilibrium position at 1A DC input. Together with the current limits for 60K and the power limit for 135K temperature increase a maximum continuous actuation force F_a=2.7N and a maximum 10s peak force F_{ap}=4.2N, when the actuator resistor does not have time to heat up, are predicted. These values are only indicative as for example the driving coil resistance is 1.8Ω when measured with a conventional Ohmmeter instead of 1.68Ω. Relevant values are compiled in Table 6.1 with geometry parameters as in Figure 5.1.

Table 6.1: *Characteristic values of the inertial actuator*

Parameter	Value	Description
d	39.5mm	overall diameter
h	20.7mm	overall height
d_3	19mm	diameter of the flange
h_3	1.7mm	height of the flange
m_t	46g	total mass
m_{lc}	12g	mass of the lower cover and coils
m_{uc}	12g	mass of the upper cover
m_i	22g	approximate moving mass
Ψ_p	~2.5N/A	primary transducer coefficient
P_{max}	~2.2W	maximum DC power input
F_{max}	~2.5N	maximum continuous actuation force, ΔT=60 degree C
F_{peak}	~4.2N	peak actuation force, 10 sec.
d	+/-2mm	maximum stroke
R_s	~22Ω	secondary coil resistance
R_p	~1.8Ω	primary coil resistance

6.2. Internal resonance frequencies

Ideally the frequency response function between the primary current and the transmitted force should look like as in Figure 2.2.1 with a -180° phase shift at the spring-mass resonance frequency and no further internal suspension dynamics. Figure 6.2.1 depicts this FRF measured at the prototype with a PCB208 force transducer below the actuator as in Figure 6.2.2 and a measurement resistor in series to the actuator. The electronics of the used ICP accelerometer incorporate a high pass filter at lower frequencies so that only measurements above approximately 10Hz make sense. Therefore a sine sweep voltage between 10Hz and 10kHz is input to the actuator. The phase plot hints at the expected -180° phase shift from +180° to 0°. At about 22Hz the very small influence of a secondary resonance frequency appears that possibly is the main rotational resonance frequency predicted by simulations in Section 4.6. Then a flat response until about 1kHz follows indicating that internal spring resonance frequencies are of small importance. For higher frequencies the stiffening effect of the upper cover plays a role. In Figure 6.2.1 the thick solid line indicates measurements without upper cover C-2 and the faint solid line is from measurements with mounted upper cover C-2. There is an additional resonance frequency at about 3200Hz that is shifted to about 3500 Hz when the cover stiffens the actuator. Another resonance frequency appears at 2000Hz when the cover is mounted. A high order low-pass filter at about 1kHz is recommended in order to cut-off the bandwidth when the actuator is used in an active control system. The exact position of these resonance frequencies depends on the mounting of the actuator relative to the force transducer, but they usually lie beyond 1kHz as is also shown in Figure 6.4.3. For higher excitation voltages there is stroke saturation at the spring-mass resonance frequency since the moving mass hits the cover. Therefore further damping is to be added for example by using feedback of the velocity signal in the secondary coil.

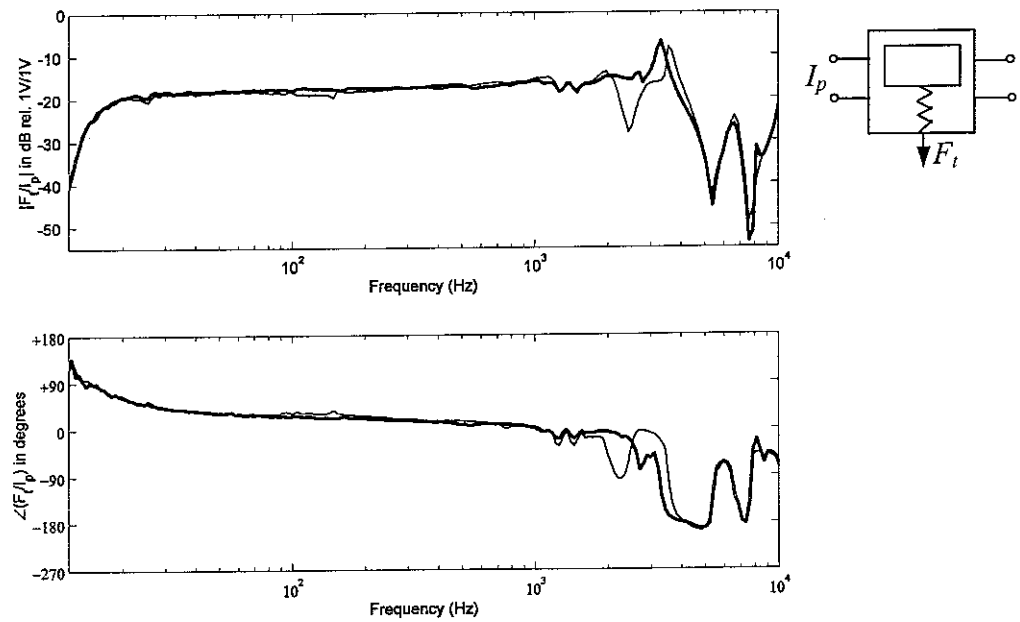

Figure 6.2.1: *FRF between primary current I_p and transmitted force F_t with upper cover (faint solid line) and without upper cover (thick solid line)*

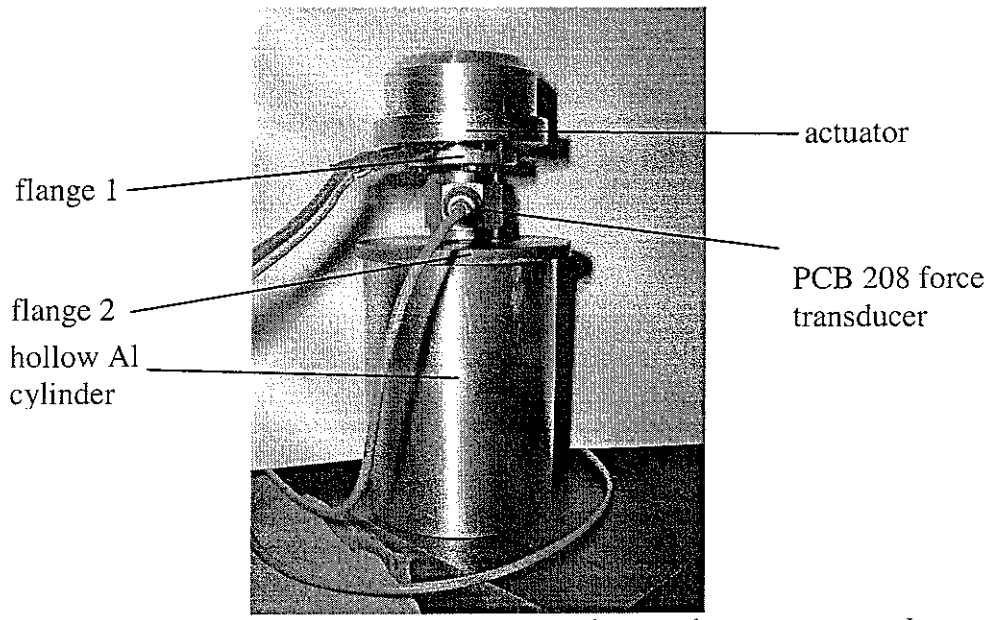

Figure 6.2.2: *Setup for the measurement of the FRF between the primary current I_p and the transmitted force F_t*

6.3. Relative velocity measurements and direct feed through

The measured FRF between the velocity signal in the secondary coil and the driving current in the primary coil is depicted in Figure 6.3.1 as a thin solid line. The peak of the spring-mass resonance frequency and the 180° phase shift is visible at about 25Hz i.e. at higher frequencies than in Figure 6.2.1 since a stiffer spring is used. Up to about 80Hz the relative vibration velocity between the moving mass and the lower cover can be sensed. For frequencies higher than the anti-resonance frequency at about 90Hz the amplitude increases at 20dB/decade and the phase shift moves again to +90°. A curve only slightly shifted in amplitude is obtained for the FRF secondary current-primary voltage verifying reciprocity of the coupling.

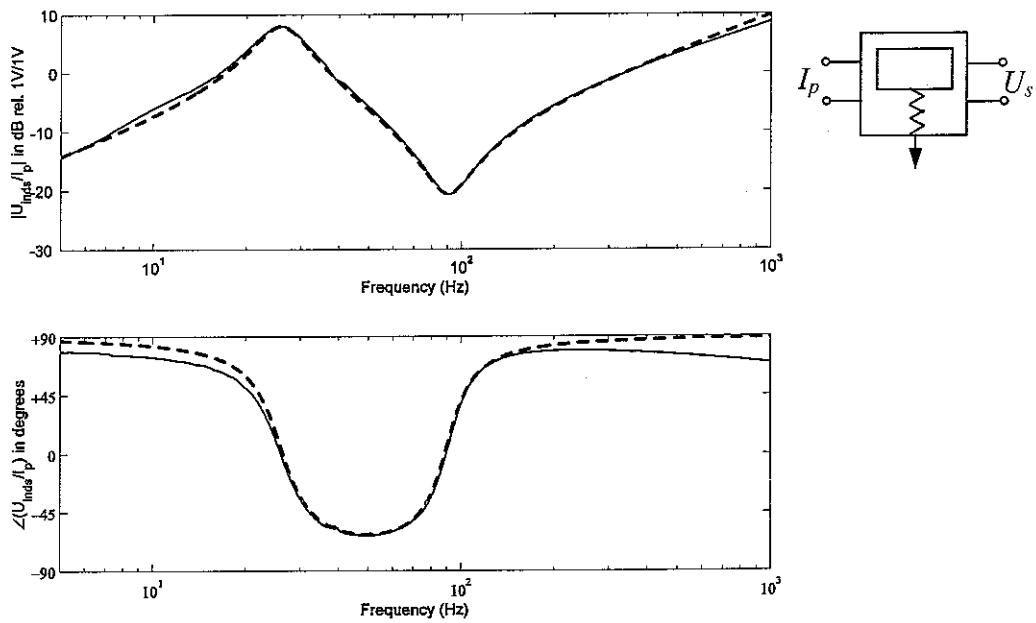

Figure 6.3.1: *FRF between the primary current I_p and the secondary voltage U_s without upper cover and stiff suspension*

In comparison Figure 6.3.2 shows the same FRF between primary current and secondary induced voltage for the test part with two coils mentioned in Section 5.3 that does not contain a moving mass. The bold dashed line indicates measurements with an iron core and the thin solid line is for measurements without iron core. Both measurements show a first order high pass filter (derivative) behaviour until an electrical cut-off frequency. This electrical frequency lies at lower values when an iron core is introduced. The similar 20dB/decade increase beyond about 90Hz in Figure 6.3.1 and until about 8kHz Figure 6.3.2 is assumed to result from the coupling between the primary driving and the secondary measurement coil.

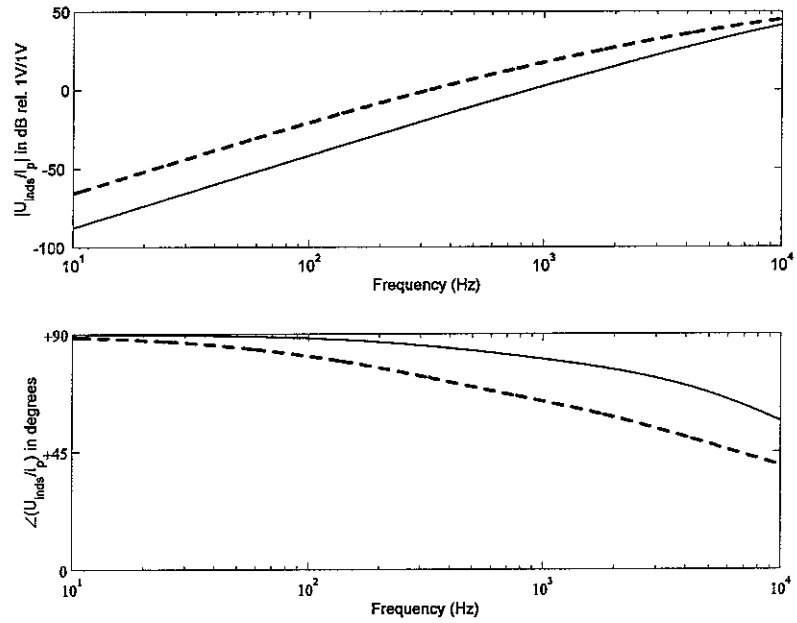

Figure 6.3.2: *FRF between the primary current I_p and the secondary voltage U_s for winding test coils*

Using formulae from [73] for two cylindrical transformer coils the secondary voltage is given by

$$U_s = \frac{\partial B}{\partial t} A_s + \Psi_s \dot{x} \tag{6.3.1}$$

if the secondary transducer coefficient Ψ_s is constant.

$$B = B_g + \mu N_p / h_p A_p \, I_p - \mu N_s / h_s A_s \, I_s \tag{6.3.2}$$

is the magnet field at the coil center that consists of a constant component due to the permanent magnet B_g and two time varying terms that depend on geometric constants described in Section 4.4 and the current in the primary coil I_p as well as in the secondary coil I_s . The vibration velocity in Equation (6.3.1) $\dot{x}$ is linked to the primary current I_p and the secondary current I_s via the sum of the forces at the moving mass

$$Z_m \dot{x} = \Psi_p I_p + \Psi_s I_s , \tag{6.3.3}$$

where $Z_m=Mj\omega+K/j\omega+D$ is the mechanical impedance of the mass-spring system and Ψ_p is the transducer coefficient of the primary coil. Solving Equation (6.3.3) for $\dot{x}$ and using the result together with Equation (6.3.2) in Equation (6.3.1) leads to the appearance of a motional impedance term Ψ_s^2/Z_m and an additional coupling term $\Psi_p\Psi_s/Z_m$ that also depends on the mechanical impedance. The first term changes damping at the resonance frequency whereas the second term determines the position of the anti-resonance frequency whose damping is equivalent to the damping D of the pure mechanical system without electromagnetic coupling. In this model the sign of the motional impedance term depends on the direction voltage is input to each coil i.e. the location of the reference ground voltage. In this case opposite input voltages are assumed, which is also obvious by the signs in Equation (6.3.2). Solving for the secondary voltage U_s gives the FRF between the secondary voltage and the primary current

$$\frac{U_s}{I_p}=\frac{L_{sp}j\omega+\dfrac{\Psi_s\Psi_p}{Z_m}}{1+\left(L_s j\omega-\dfrac{\Psi_s^2}{Z_m}\right)/Z_s}, \tag{6.3.4}$$

where $Z_s=U_s/I_s$ is the electrical impedance of the secondary coil with the measurement device in parallel. Neglecting the self-inductance of the secondary coil L_s this FRF is simulated as a bold dashed line in Figure 6.3.1 for parameter values compiled in Table 6.2. This identification is not unequivocal since several parameter combinations lead to a similar curve in Figure 6.3.1. Especially since the driving current amplifier might add negative damping because of positive current feedback. Measurements and simulations fit well in the important frequency range around the resonance and the anti-resonance frequency. For higher frequencies neglecting the self-inductance of the secondary coil and non-linear effects lead to differences due to the permanent magnet and the iron within the coil.

Table 6.2: *Parameter values used for simulations in Figure 6.3.1*

Parameter	Value	Description
Z_s	0.57Ω	Resistance of secondary coil and measurement equipment
L_{sp}	0.0005H	Coupling inductance
M	0.0203kg	Weight of the moving mass
D	3.5Ns/m	Damping factor
K	540N/m	Spring stiffness
Ψ_p	2.6N/A	Transducer coefficient of the driving coil
Ψ_s	1.146N/A	Transducer coefficient of the measurement coil

In order to increase the measurement bandwidth the direct feed through could be prevented using self-sensing in either the primary or the secondary coil comparable to the one described in [12]. But Figure 6.3.3. shows the FRF between the current and the voltage in the primary coil. Although depending on the used current amplifier it may show the influence of the coupling to the mechanical system at about 20Hz the frequency bandwidth due to the electric frequency R_p/L_p is reduced relative to the bandwidth of the FRF primary current to secondary voltage determined by the electrical frequency R_s/L_s once feed through is compensated because of the larger value of the self-inductance L_p.

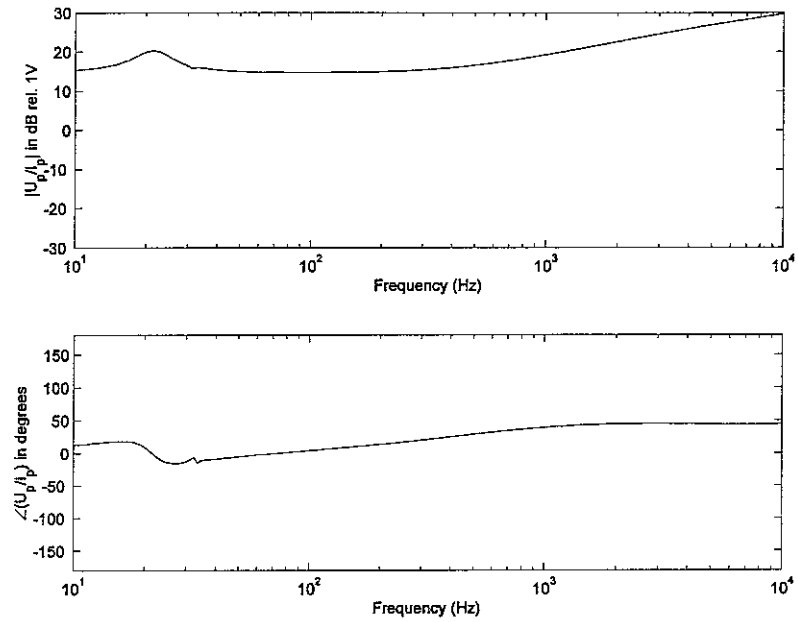

Figure 6.3.3: *FRF between the primary voltage U_p and the primary current I_p without upper cover*

Figure 6.3.4 shows the FRF between the secondary current and the secondary voltage. Although the bandwidth is not reduced relative to the primary current-secondary voltage case since the self-inductance L_s is the same the influence of the electromechanical coupling is much reduced due to the high resistance. Additionally a higher power input is necessary to obtain a comparable current as in the primary coil. Thus, velocity feedback using the secondary coil should be used instead of self-sensing with either of the coils.

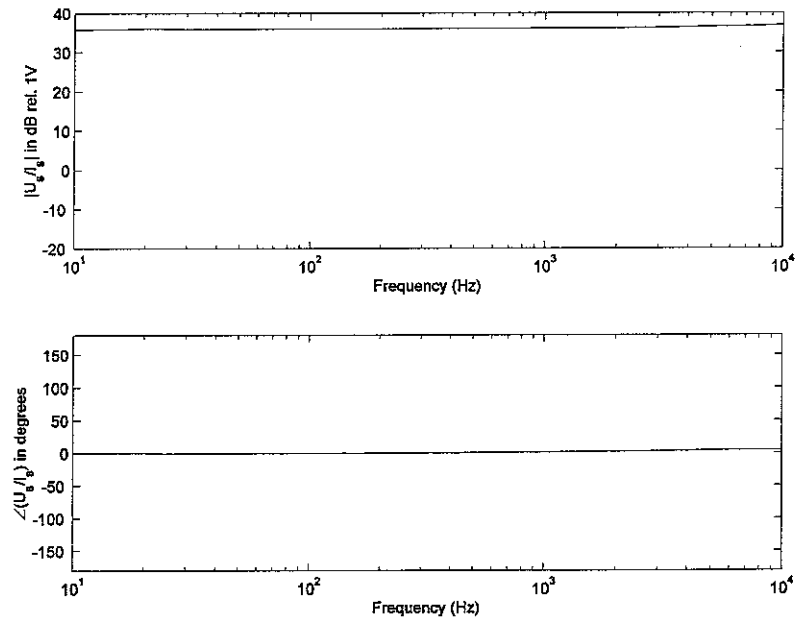

Figure 6.3.4: *FRF between the secondary voltage U_s and the secondary current I_s without upper cover*

6.4. Damping of internal resonance frequency using secondary coil voltage feedback

Before the voltage in the secondary coil is fed back stability of the closed loop is examined by considering the open loop. In a first scheme a 2nd order filter is added to the feedback loop that increases velocity feedback performance without significantly altering the available frequency bandwidth. In a second scheme an electronic circuit similar to the one described by [82] is implemented that allows increasing the bandwidth of velocity measurements with the secondary coil and the increased damping bandwidth is verified at a plate.

First Figure 6.4.1. schematically shows the compensator electronics for feedback of the secondary coil signal. A 2nd order filter with a cut-off frequency of about 1kHz is added that compensates for the non-ideal current amplifier behaviour. The variable 50kΩ resistor at the first operation amplifier in the feedback loop is used to adjust the feedback gain.

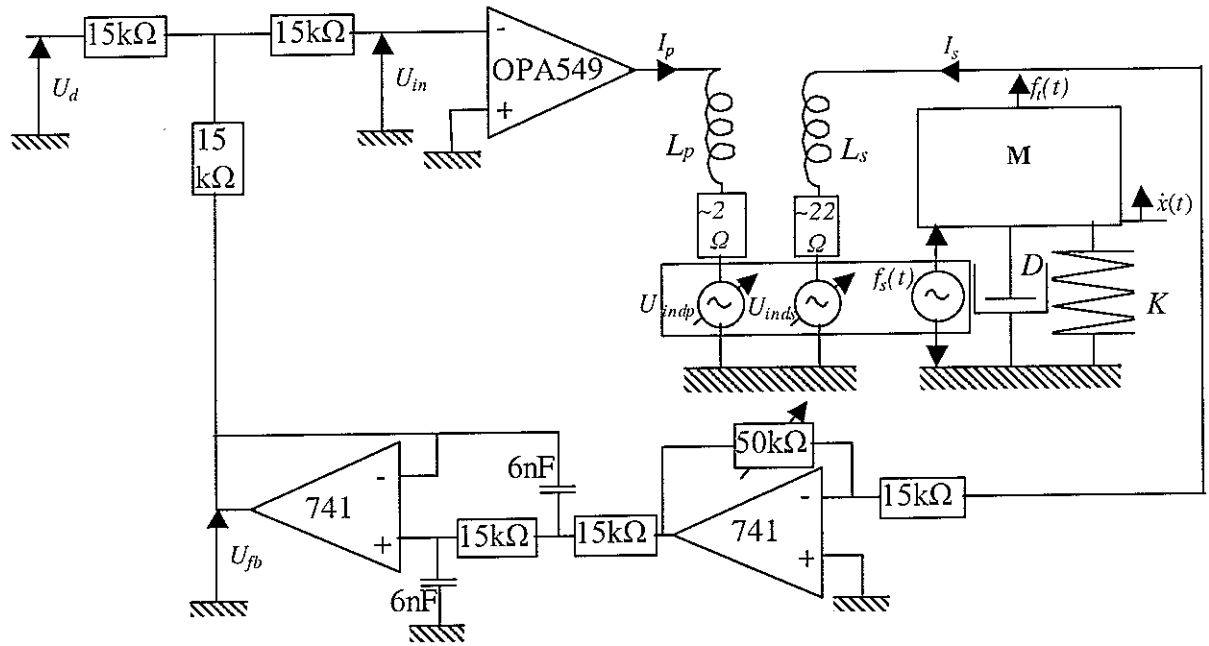

Figure 6.4.1: *Compensator electronics for velocity feedback measured by the secondary coil*

Figure 6.4.2 shows a plot of the imaginary part versus the real part of the open loop FRF between the input voltage to the voltage-current amplifier U_{in} and the feedback voltage U_{fb} for a feedback gain that guarantees stability. Note that negative feedback is realized with inverting amplifiers instead of a summing amplifier so that the point $(1,0j)$ becomes the critical point and the loop just needs to be closed without inverting. No further resonance appears once the locus has passed into the positive half-plane so that it is expected that for higher order filters even higher feedback gains could be realized. In addition to the big resonance loop due to the induced voltage an additional smaller one is visible that is probably due to the influence of the rotational resonance frequency.

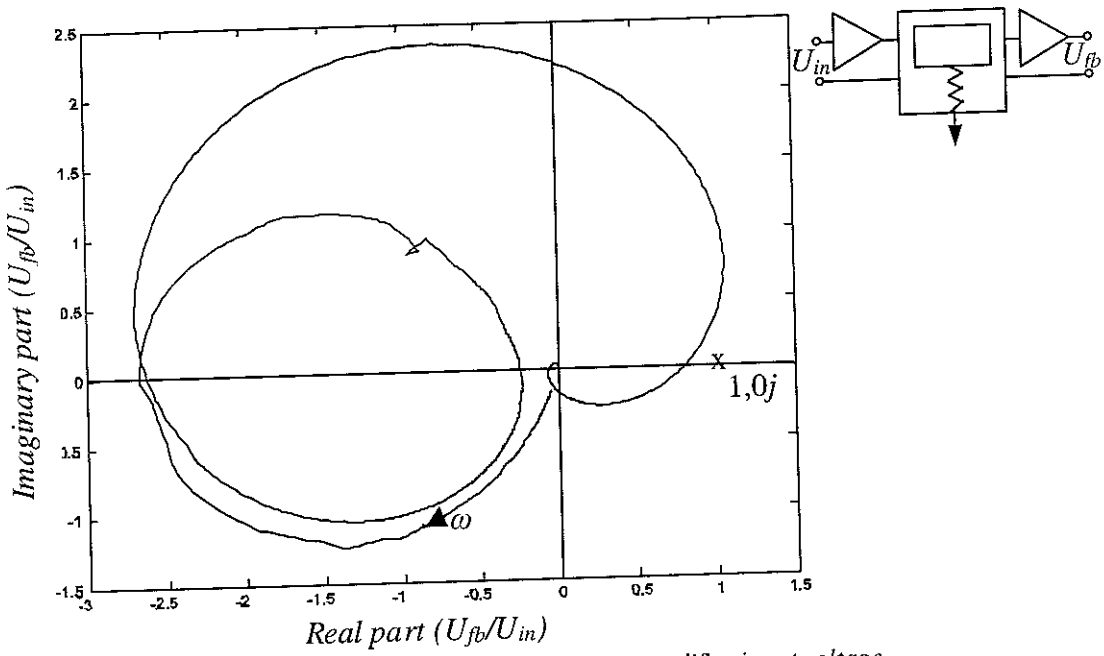

Figure 6.4.2: *Nyquist plot of the open loop FRF between the amplifier input voltage U_{in} and the feedback voltage U_{fb}*

Figure 6.4.3. shows the FRF between a disturbance voltage U_d that simulates external vibration excitation of the actuator and the transmitted force on the structure. The solid faint line is measured in the open loop case, the solid bold and dashed bold lines are with increasing feedback gains where the dashed bold line corresponds to a feedback gain used for measurements in Figure 6.4.2. For increasing feedback gains the phase at the spring-mass resonance frequency is typically deformed like a system to which viscous damping is added.

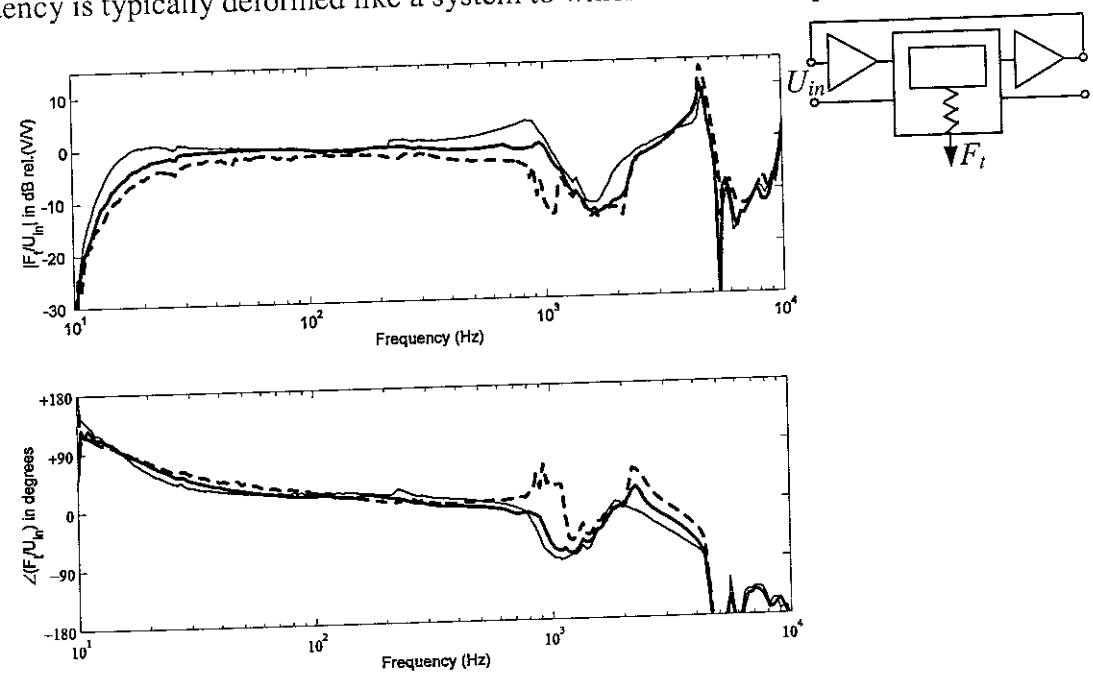

Figure 6.4.3: *FRF between the disturbance voltage U_{in} and the transmitted force F_t measured by an accelerometer below the actuator in the open loop case (faint solid line) and for increasing closed loop feedback gains (thick solid and thick dashed line)*

Moreover until 1kHz the amplitude is flattened and the phase shift is shifted upwards. The resonance peak at 4.5kHz is increased and it is likely to be of serious concern when the actuator is used in a force feedback loop. Current amplifier dynamics also increase the amplitude in this frequency range so that a high order cut-off filter and further improvement of the current amplifier is recommended at 1kHz if additional force feedback is implemented.

Second Figure 6.4.4 shows the electronics used to increase the bandwidth for velocity measurements with the secondary coil. A high pass filter in series with an inverting amplifier filters a signal proportional to the primary current and the resulting signal is subtracted from the secondary coil signal. Hence, the high pass filter behaviour of the voltage induced in the secondary coil can be shifted to higher frequencies as illustrated by measurements shown in Figure 6.4.5.

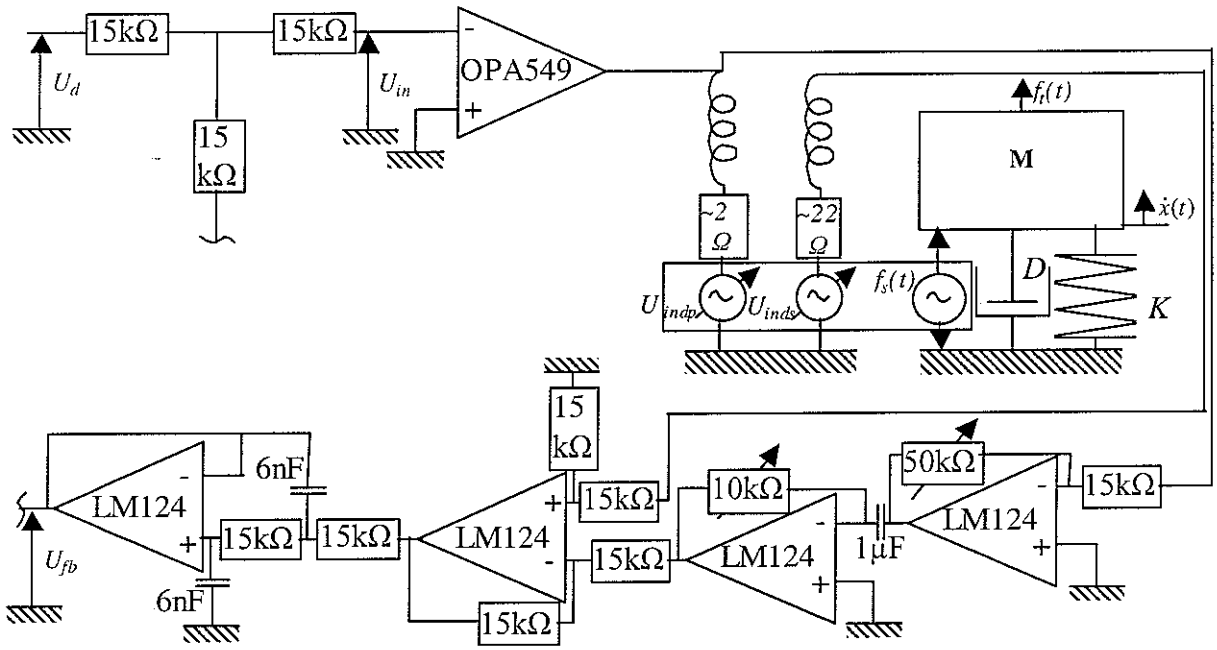

Figure 6.4.4: *Feed forward electronics for relative velocity estimation*

The anti-resonance of the induced voltage signal without compensation (fine solid line) lies at about 70Hz for this spring configuration and it can be shifted up to 200Hz with compensation of the coupling inductance (bold solid line). This compensation scheme is limited by the dynamics of available operation amplifiers and a DC offset in the disturbance signal. More physical limits are given by changing parameter values since for example resistors change with temperature so that especially when higher currents are used an adaptation mechanism of the compensating high pass filter coefficients is recommended. Due to the used operation amplifiers there is an electronic resonance frequency at about 2.5kHz so that a steep cut-off filter is to be applied at lower frequencies in the feedback path limiting control bandwidth. The DC offset can be regulated using the internal DC offset regulation of operation amplifiers. In order to check maximum control bandwidth for active vibration damping the inertial actuator is attached to a plate structure and the secondary coil voltage is fed back using the mentioned compensator and a low pass filter with 800Hz cut-off frequency. Figure 6.4.6 shows a Bode plot of the FRF between the input voltage to a primary exciting shaker U_p and the acceleration at the secondary force input position X_{dds} measured with an accelerometer on the side of the plate opposite to the inertial actuator. The solid line is open loop

measurements whereas the dashed line indicates closed loop measurements with a feedback gain close to the stability limit. Damping is added to resonance peaks below about 200Hz; spill-over occurs at higher resonance frequencies. In comparison to pure secondary voltage feedback the bandwidth where damping is added to an attached structure is increased. By decreasing the damping bandwidth the amount of added damping might be increased.

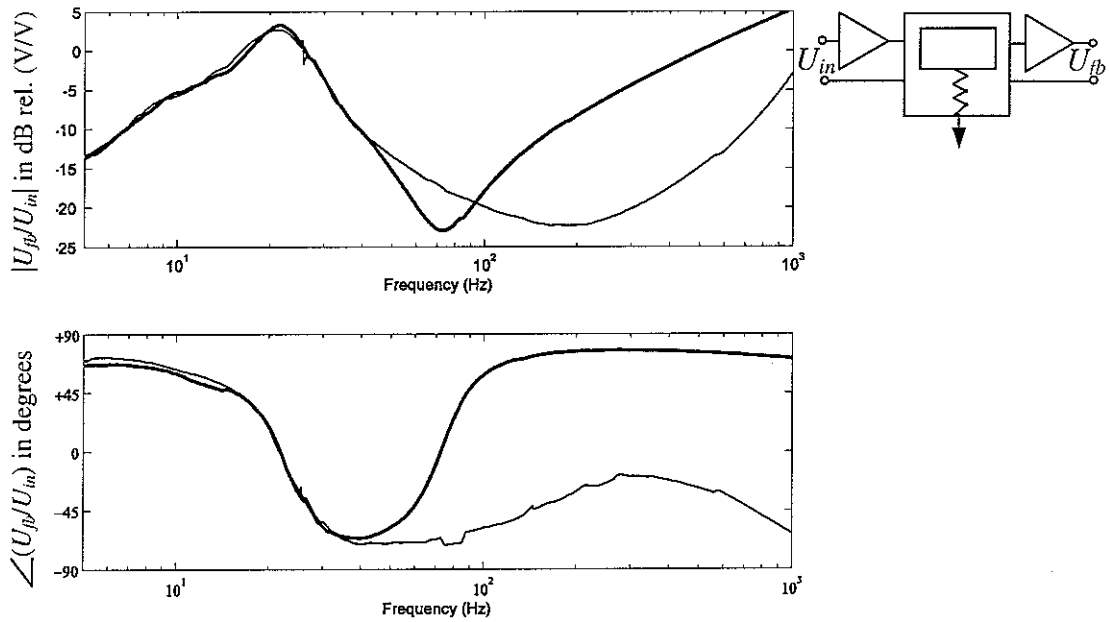

Figure 6.4.5: *Open loop FRF between the voltage in the secondary coil U_{fb} and the feedback voltage U_{fb} with (faint solid line) and without compensation circuit (bold solid line)*

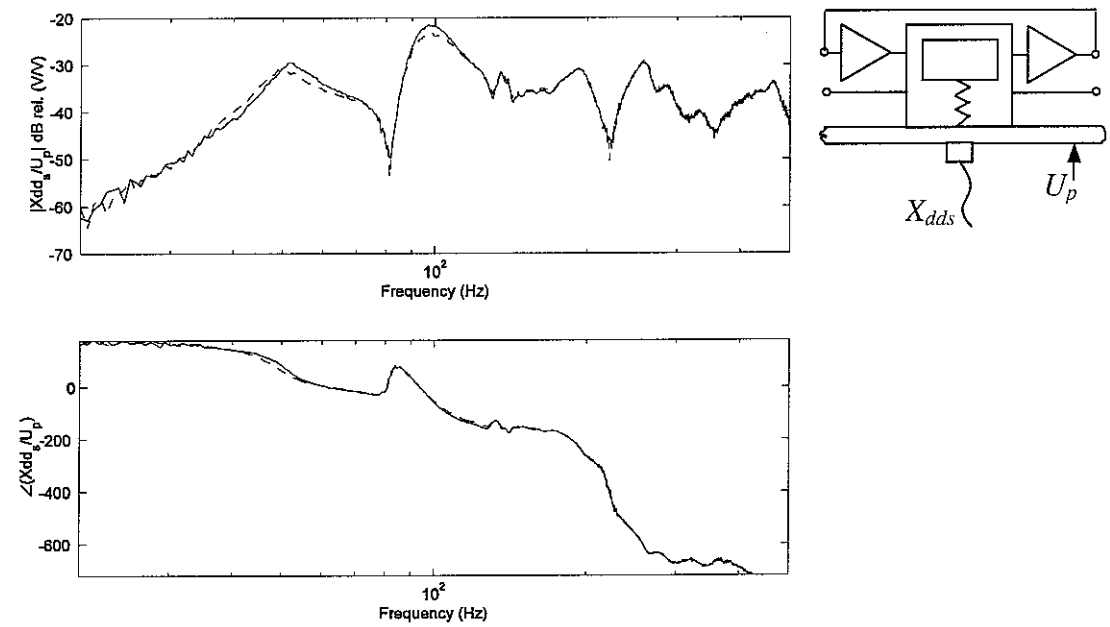

Figure 6.4.6: *Open loop (solid line) and closed loop (dashed line) FRF between the input voltage to a primary exciting shaker U_p and the plate acceleration at the inertial actuator position X_{dds}*

7. CONCLUDING REMARKS

A lightweight, electrodynamic, inertial actuator with internal velocity sensor has been developed. During the design requirements for its use for active vibration control at a lightweight panel are compiled and appropriate electromagnetic and mechanical components are investigated. Finally manufacturing challenges are solved and the actuator performance is evaluated.

The compilation of requirements shows that the permanent magnet and coil material properties are a limit for the design of the electromagnetic circuit. The transmitted 4N peak force is limited by the moving mass of 0.02kg and the maximum stroke of 0.001m of the actuator at lower frequencies and by electromagnetic properties at higher frequencies. A lower bandwidth limit is given by the moving mass, the minimum suspension stiffness an the stroke to about 20Hz. The velocity sensor function can be either achieved using a self-sensing approach or an additional measurement coil.

An investigation of the electromagnetic behaviour shows that a combined consideration of the amount of wire in the air gap and the amount of magnetic B-field in the air gap gives a maximum force that is larger than the force at maximum B-field or maximum amount of wire in the air gap at constant actuator mass. FE simulations are used to optimise the actuator geometry and the air gap dimensions. They show that the transmitted peak force of 4N can only be realized at a power input of more than 5W when a required mass of 0.02kg is considered.

The dimensions of the electromagnetic circuit are used as input for the mechanical design step where different solutions for the suspension, the guide, the cover and the coil are investigated in detail. Especially stress considerations for different types of suspensions at the required stroke-force combination lead to the choice of ring springs. At given dimensions other spring types especially membranes show high internal stress concentrations. The guiding function is realized by an internal axis that allows small air gap tolerances. A whole cover is used in order to guarantee maximum protection of the air gap. The driving coil is chosen to 0.315mm as to give maximum actuation force for given dimensions and manufacturing techniques. In order to allow easy manufacturing and to reduce transformer coupling a wire diameter of the measurement coil of 0.052mm with 2 horizontal layers is chosen. At a design combining the mentioned, different functions a dynamic FEA shows that the lower frequency limit of about 20Hz can only be reached if an internal rotational frequency is negligible or the boundary conditions of the ring spring are chosen appropriately. A higher bandwidth limit is given by internal resonance frequencies whose importance is precisely determined at an actuator prototype.

During the computer aided design tolerances in the air gap, at bushings, the cover and at the wire outlet are identified to be important. Special care is taken for the manufacture of the lower cover part. For the coil winding a special winding device is built and the measurement wire is protected from the driving wire by special grooves. A special tool is designed to form the ring springs and finally spring steel is chosen as an appropriate material. The assembly follows specific steps since the moving mass part can only be machined to its final stage after the coil has been wound.

The validation of the prototype actuator gives a continuous force input of about 2.5N at a power input of 2.2W, but a higher peak force of up to 4.2N can be achieved during a short period of time. A moving mass of 0.022kg is realized at a total mass of 0.046kg that can be reduced to 0.034kg in a clean environment without using the upper cover. The upper bandwidth limit lies beyond 1kHz and the lower bandwidth limit is given by the spring-mass resonance frequency at about 20Hz. The measurement coil is used to add a large amount of vibration damping at the spring-mass resonance frequency, but transformer coupling limits the velocity measurement bandwidth to about 90Hz. An electronic compensation scheme does increase the velocity measurement bandwidth to about 200Hz, but DC offsets and internal electronic resonance frequencies limit the damping added to an attached plate. Without inductance compensation self-sensing is limited to low frequencies by the high inductance in the primary coil.

Further work could first investigate possible sensing improvements using a digital compensation scheme or introduce an adaptation mechanism in order to not be forced to fine-tune electronic components each time before operation. The geometry of the secondary coil could be optimised to reduce transformer coupling at acceptable sensitivity.

Second the frequency bandwidth and damping added to an attached plate with the internal velocity sensor could be compared to a self-sensing mechanism, conventional passive means and other collocated active vibration control schemes using explicit sensors.

Third springs in postbuckling could be investigated to further reduce the spring-mass resonance frequency and allow low stiffness at acceptable strokes at even smaller dimensions.

Finally although they show a higher degree of non-linearity electromagnetic actuators tend to have a higher force at the same magnetic field in the air gap [23] so that a similar study could be carried out for this type of actuators either with a separate velocity sensor or an internal sensorless velocity estimator.

8. REFERENCES

[1] Beranek, L.L. Acoustics. McGraw-Hill. New York. 1954.

[2] Sun, J.Q. Some Observations on Physical Duality and Colocation of Structural Control Sensors and Actuators. Journal of Sound and Vibration. Vol.194. No.5. 1996. pp.765-770

[3] Preumont, A. Vibration Control of Active Structures. Kluver Academic Publishers. 2nd Edition. 2002.

[4] Fuller, C.R. Elliott, S.J. and Nelson, P.A. Active Control of Vibration. Academic Press. London. 1997.

[5] Henrioulle, K. and Sas, P. Experimental validation of a collocated PVDF volume velocity sensor/actuator pair. Journal of Sound and Vibration. Vol. 265. 2003. pp. 489-506.

[6] Crawley, E.F. and de Luis, J. Use of Piezoelectric Actuators as Elements of Intelligent Structures. American Institute of Aeronautics and Astronautics. Vol. 25. No. 10. October 1987. pp.1373-1385.

[7] Leo, D.J. and Paine, J.S.N. A Comparison of Point Force and Distributed Actuators for the Active Control of Structural Sound Radiation. Proceedings of SPIE Smart Structures and Materials. Smart Structures and Integrated Systems. Vol. 3041. 3-6 March 1997. pp. 819-828.

[8] Gavagni, M. Gardonio, P. and Elliott, S.J. Theoretical study of a velometer sensor-piezoelectric patch actuator pair for direct velocity feedback control systems. ISVR Technical Report No 303. July 2004.
[9] Elliott, S. J. Gardonio, P. Sors, T.C. and Brennan, M.J. Active vibroacoustic control with multiple local feedback loops. Journal of the Acoustical Society of America. Vol. 111. No. 2. February 2002. pp. 908-915.
[10] Tappert, P.M. Mercadal, M. and v. Flotow, A. Evaluation of actuation schemes used for acoustic attenuation of vibrating surfaces. Proceedings of SPIE Smart Structures and Materials. Industrial and Commercial Applications of Smart Structures Technologies. Vol. 3044. 4-6 March 1997. pp. 79-86.
[11] Elliott, S.J. Serrand, M. and Gardonio, P. Feedback Stability Limits for Active Isolation Systems with Reactive and Inertial Actuators. Transactions of the ASME. Vol.203. April 2001. pp.250-261.
[12] Paulitsch, C. Gardonio, P. and Elliott, S.J. Investigation of an Electrodynamic Actuator for Self-Sensing Active Vibration Control. ISVR Technical Memorandum No. 917. Southampton. August 2003.
[13] Janocha, H. Aktoren Grundlagen und Anwendungen. Springer-Verlag. Berlin. 1992.
[14] Lee, Y.K. and Shimoyama, I. A micro rubber artificial muscle driven by a micro compressor for artificial limbs. Actuator 2000. 7th International Conference on New Actuators. 19-21 June 2000. Bremen. pp.272-275.
[15] Janocha, H. Adaptronics and Smart Structures. Springer. Berlin. 1999.
[16] Busch-Vishniac, I. J. Electromechanical Sensors and Actuators. Springer. New York. 1998.
[17] Brennan, M. J. Garcia-Bonito, J. Elliott, S.J. David, A. and Pinnington, R.J. Experimental investigation of different actuator technologies for active vibration control. Smart Structures and Materials. Vol. 9. 1999. pp.145-153.
[18] product catalogue Cedrat SA www.cedrat.com.
[19] Wildi, T. Electrical machines, drives and power systems. Prentice Hall. Upper Saddle River. NJ. 2002.
[20] Stoelting, H-D and Kallenbach, E. Handbuch Elektrische Kleinantriebe. Hanser. Munich. 2002.
[21] Nasar, S.A. and Boldea, I. Linear electric motors: Theory, design and practical applications. Prentice-Hall. Englewood Cliffs. NJ. 1987.
[22] Haase, H. Hartwig, C. Hofmann, M. and Karkosch, H.-J. Electromagnetic actuators for active engine vibration cancellation. Actuator 2000. 7th International Conference on New Actuators. 19-21 June 2000. Bremen. B5.4.
[23] Oberbeck, C. and Ulbrich, H. Design and optimisation of electromagnetic actuators for mechanical and automotive applications. Actuator 2002. 8th International Conference on New Actuators. 10-12 June 2002. Bremen. Pp.600-603.
[24] Kim, Y-B. Hwang, W-G. Kee, C-D and, Yi H-B. Active vibration control of a suspension using an electromagnetic damper. Proc Instn Mech Engrs Vol 215 Part D. ImechE 2001.
[25] Zago, L and Genequand, P. Electromechanical lever blocks for active vibration isolation. Smart Structures and Materials 2000: Damping and Isolation. Proceedings of SPIE Vol. 3989 2000. pp.479-486.
[26] Kjellqvist, P. Sadarangani, C. and Oestlund, S. Design of a Permanent Magnet Synchronous Machine for an Electromechanical Active Suspension Actuator. IEEE

International Electric Machines and Drives Conference. June 17-20, 2001. Cambridge, Ma.pp.534-541.
[27] Mirzaei, S. Saghaiannejad, S.M. Tahani, V. and Moallem, M Electromagnetic shock absorber. IEEE International Electric Machines and Drives Conference. June 17-20, 2001. Cambridge, Ma. pp. 761-764.
[28] Roschke, Th. Miniaturised bipolar electromagnetic actuators for space applications. Actuator 2002. 8th International Conference on New Actuators. 10-12 June 2002. Bremen. pp.664-667.
[29] product catalogue BEI Kimco Magnetics Division www.beikimco.com.
[30] product catalogue TIRA GmbH www.tira-gmbh.de.
[31] product catalogue LDS www.lds-group.com.
[32] product catalogue LMS www.lmsintl.com.
[33] product catalogue Unholtz-Dickie Corporation www.udco.com.
[34] product catalogue Aurasound Inc. www.aurasound.com.
[35] She, T. Active vibration control by eigenstructure assignment. Ph.D. thesis. Katholieke Universiteit Leuven. October 1992.
[36] Heinrich, J. Hermann, R. Eccarius, M. and Kallenbach, E. Optimal application fields of electromagnetic and piezoceramic actuators. Actuator 2000. 7th International Conference on New Actuators. 19-21 June 2000. Bremen.
[37] Wang, B. Fuller, C.R. and Dimitriadis, E.K. Active control of noise transmission through rectangular plates using piezoelectric or point actuators. Journal of the Acoustical Society of America. Vol. 90. No. 5. pp. 2820-2830. 1991.
[38] Nasar, S.A. Boldea, I. And Unnewehr, L.E. Permanent magnet, reluctance and self-synchronous motors. CRC Press.
[39] Kallenbach, E. Eick , R. Quendt, P. Stroehla, T Feindt, K. and Kallenbach, M. Elektromagnete. Grundlagen, Berechnung, Entwurf und Anwendung. 2nd edition. Teubner. Stuttgart. 2003.
[40] Hendershot, J.R. and Miller The Design of brushless permanent-magnet motors. Magna Physics Publishing and Clarendon Press. Oxford. 1994.
[41] Hanselman, D.C. Brushless permanent-magnet motor design. McGraw-Hill. New York. 1994.
[42] Jufer, M. Size limits and characteristic influence of electromagnetic actuators. Actuator 94. 4th International Conference on New Actuators. 15-17 June 1994. Bremen. pp.390-393.
[43] Borwick, J. Loudspeaker and headphone handbook. Butterworths. London. 2nd edition.1994.
[44] McCaig, M. Permanent magnets in theory and practice. Pentech Press. London. 1977
[45] Ireland, J.R. Ceramic permanent-magnet motors. McGraw-Hill. New York. 1968.
[46] Snelling, E.C. Soft ferrites properties and applications. Butterworths. London. 2nd Edition. 1988 .
[47] Miyashita, O. Ohniwa, K. Fujimaki, T. and Morikawa, M. Analysis of the Flux-Lag Effect in an Iron Core. Journal of the Japan Society of Applied Electromagnetics and Mechanics. Vol. 19. No.5. 1995. pp.875-878.
[48] Leigh, R. The Systematic Design of an Inductive Transducer Coil Winding System. M.Phil. thesis. University of Southampton. February 1991.
[49] Kallenbach, E. and Stroehla, T. Dynamic simulation of electromagnetic actuators using network models including eddy currents. Actuator 2002. 8th International Conference on New Actuators. 10-12th June 2002. Bremen. pp.604-607.

[50] Rausch, M. Numerische Analyse und Computeroptimierung von elektrodynamischen Aktoren - am Beispiel eines elektrodynamischen Lautsprechers. Dr.-Ing. Thesis. University of Erlangen-Nuremberg. Erlangen. 2001.
[51] VandeSande, H. Modelling and finite element simulation of non-linear and anisotropic quasi-static electromagnetic systems. Ph.D. thesis. KU Leuven. 2003.
[52] Asche, G. Elektromagnetischer Actuator mit beschleunigter Bewegung. Dr.-Ing. Thesis. RWTH Aachen. Aachen. 1988.
[53] European Patent "Aktiver Schwingungstilger" 96 103 094.7.
[54] Bendel, K. Brechlin, E. and Storz, A. Electromagnetic vibration excitation of moments and forces with minimal mass loading. Proceedings of ISMA25. 2000. pp.967-972.
[55] Hanieh, A. A. Active Isolation and Damping of Vibrations via Stewart Platform. Ph.D. thesis. Universite Libre de Bruxelles. January 2003.
[56] Rogers, P. Electrodynamic Shaker Performance Breakthroughs: Extreme Random and SRS Shock Testing. 74th Shock & Vibration Symposium. October 26-31 2003. San Diego.
[57] Godkin, M. New developments in the linear voice coil actuator technology. Actuator 2002. 8th International Conference on New Actuators. 10-12 June 2002. Bremen. pp.188-191.
[58] Foshage, J. Davis, T. Sullivan, J. Hoffman, T. and Das, A. Hybrid active/passive actuator for spacecraft vibration isolation and suppression. Proceedings of the SPIE. Vol. 2865. March 1996.
[59] product catalogue ADD www.micromega-dynamics.com.
[60] Inman, D.J. Control/Structure Interaction: Effects of Actuator Dynamics. In Mechanics and Control of Large Structures. Ed. J.L. Junkins.4.Vool29.1990. pp.507-533.
[61] Garcia, E. Webb, S. and Duke, J. Passive and active control of a complex flexible structure using reaction mass actuators. Transactions of the ASME. Journal of Vibration and Acoustics. Vol. 117. January 1995. pp.116-122.
[62] Paulitsch, C. Gardonio, P. and Elliott, S.J. Active vibration damping using a self-sensing electrodynamic actuator. Proceedings of the SPIE. Smart Structures and Materials. Damping and Isolation. Vol.5386. March 2004.
[63] Olson, H.F. Elements of Acoustical Engineering. D van Nostrand. NY. 2nd edition. 4th reprint. 1952.
[64] Woolvet, G.A. Transducers in digital systems. IEE Control Engineering Series 3. Peter Peregrinus. London. 1977. pp.64f.
[65] Gardonio, P. Bianchi, E. and Elliott, S.J. Smart panel with multiple decentralized units for the control of sound transmission. Part I: theoretical predictions. Journal of Sound and Vibration. Vol. 274. No.1-2. July 2004. pp.163-192.
[66] Czichos, H. ed. Huette Die Grundlagen der Ingenieurwissenschaften. 30th edition. Springer. Berlin. 1996.
[67] product catalogue ThyssenKrupp VDM GmbH. www.kruppvdm.de.
[68] product catalogue Goodfellow Cambridge Limited www.goodfellow.com.
[69] Ehmann, C. Methoden und Komponenten für die Realisierung aktiver Schwingungsdämpfung. Dr.-Ing. Thesis. Technische Universität Darmstadt. Shaker. Aachen. 2004.
[70] Stöbener, U. Untersuchungen zur Schwingungs- und Schallabstrahlungsregelung flächenhafter Strukturen. Dr.-Ing. Thesis. Universität Stuttgart. Fortschritt-Berichte VDI Reihe 11 Nr.307. VDI. Düsseldorf. 2002.
[71] De Man, P. Contrôle actif du rayonnement acoustique des plaques: une approche a faible autorité. Ph.D. Thesis. Université Libre de Bruxelles. Brussels. 2004.

[72] Lindner, D.K. Celano, T.P. and Ide, E.N. Vibration Suppression Using a Proofmass Actuator Operating in Stroke/Force Saturation. Transactions of the ASME. Journal of Vibration and Acoustics. Vol. 113. October 1991. pp.423-433.
[73] Inan, U. S. and Inan, A. S. Engineering Electromagnetics. Addison-Wesley. Menlo Park. 1999.
[74] Hunt, F.V. Electroacoustics. Transduction and Its Historical Background. Harvard University Press. 1954.
[75] Bazant, Z.P. Cedolin, L. Stability of structures elastic, inelastic, fracture and damage theories. Oxford University Press. New York. 1991.
[76] product catalogue Servometer www.servometer.fr.
[77] Den Hartog, J.P. Sterkteleer. Prisma-Technica. Het Spectrum. Utrecht/Antwerpen. 1967.
[78] Blevins, R.D. Formulas for natural frequencies and mode shape. Van Nostrand. New York. 1979.
[79] product catalogue Fabory. www.fabory.com.
[80] Nabla Technisch Studiebureau. Riemst. Belgium.
[81] Franke, H.-J. and Glienicke, J. Maschinenelemente I-III. Lecture notes. Technische Universität Braunschweig. IKMF. Brunswick. 1996.
[82] Okada, Y. Matsuda, K. Hashitani, H. Self-sensing Active Vibration Control using the Moving-Coil-Type Actuator. Journal of Vibration and Acoustics. Vol.117. October 1995. pp. 411-415.

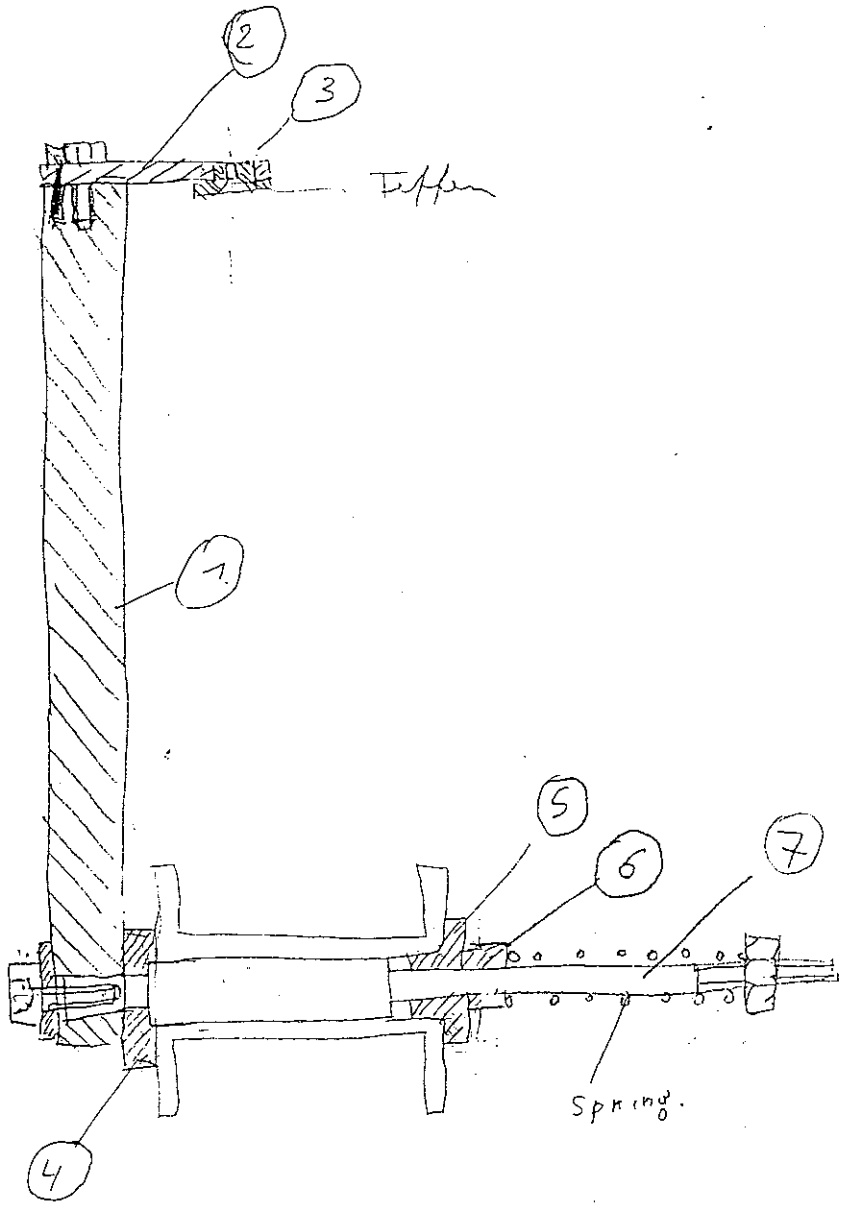

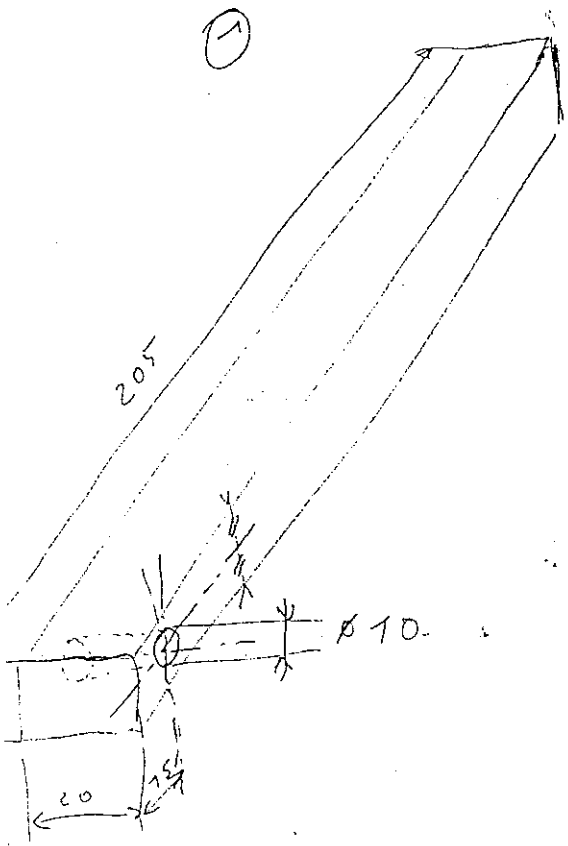
1
205
ø10.
20
15

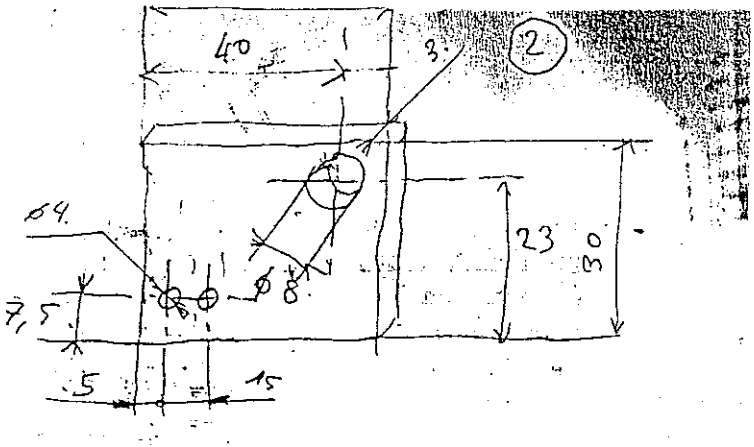
2
40
1
3.
ø4.
ø8.
7,5
5
15
23
30

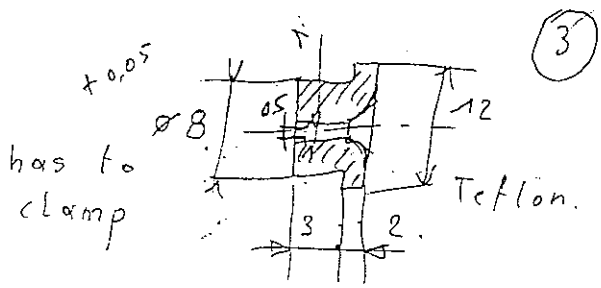
3
+0,05
ø8.
05
12
has to
clamp
Teflon.
3
2.

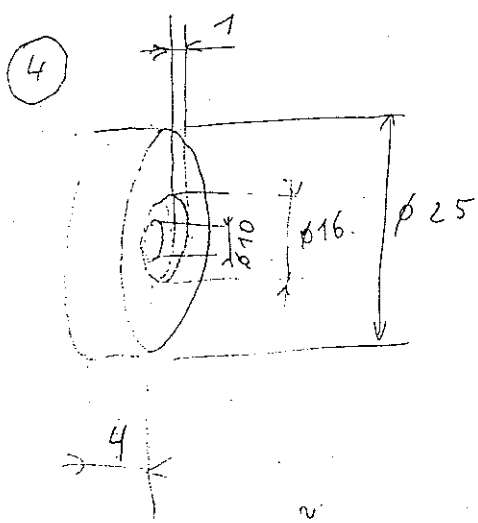
4
1
ø10
ø16.
ø25
4

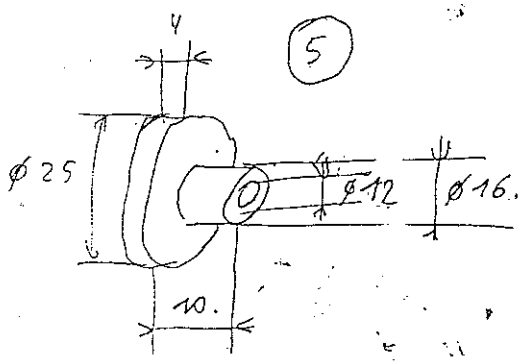
5
4
ø25
ø12
ø16.
10.

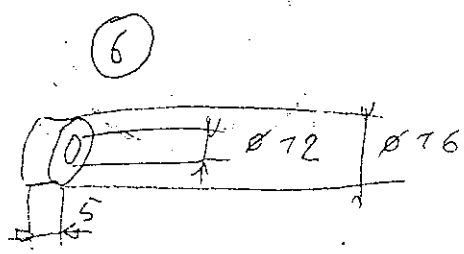
6
ø12
ø16
5

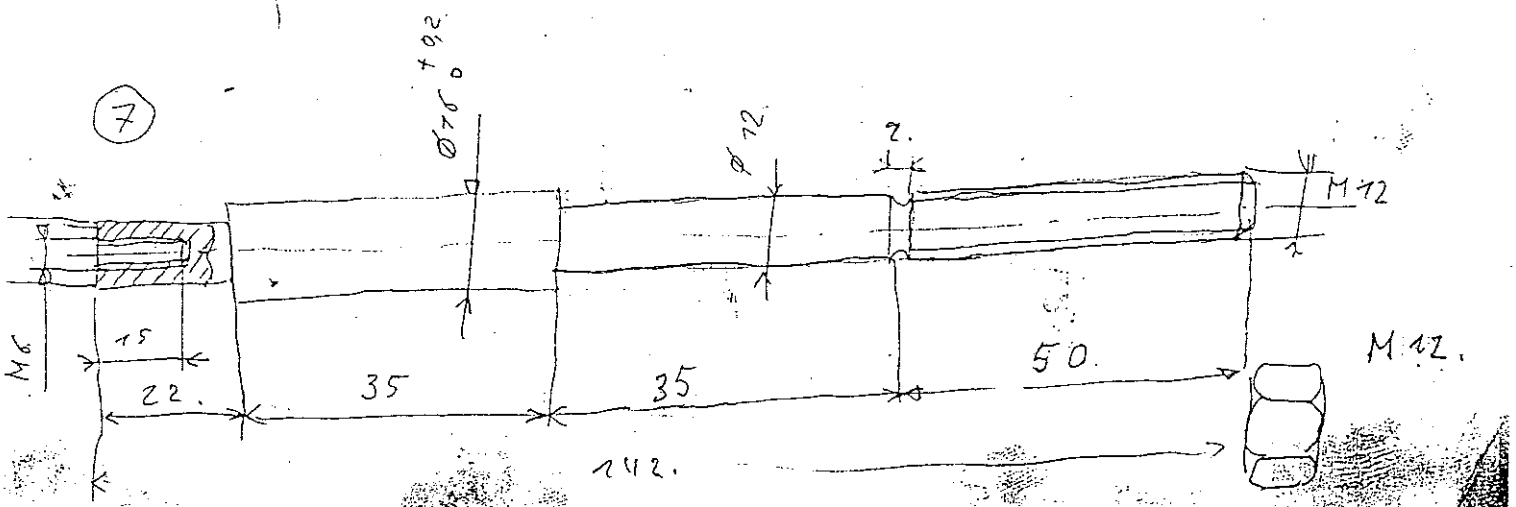
7
ø16 +0,2 0
ø12
2.
M12
M6
15
22.
35
35
50
M12.
142.

ARALDITE

CW 1301 + HY 1300

Low-viscosity unfilled epoxy casting and impregnating system

® Araldite casting and impregnating systems for inductive components

Ready-for-use Mixing Pack

Mixture	Weight		or	Volume	
	Pack	Ratio		Pack	Ratio
Araldite CW 1301	546 g	100		488 ml	100
Hardener HY 1300	180 g	33		180 ml	37

Pack contents: 2 x 273g resin + 2 x 90g hardener

Mixing

1. Thoroughly stir the Araldite resin in its container to ensure uniform dispersion of the filler. A spatula for stirring is supplied in the pack.
2. Pour the hardener into the resin container.
   Note Traces of hardener remaining on the walls of the hardener container should be disregarded.
3. Stir thoroughly until mixing is complete.

Deaeration

The mixed resin-hardener (at 25°C or above) may be deaerated when necessary by placing the container in a vacuum chamber. Vacuum should be applied with care in order to expand and break the foam without causing overflow.

Usable life

The mixed resin-hardener held in the resin container has usable life:

Temperature of mixture	25°C	40°C
Usable life	½h	ca 12 min

Usable life may be extended by dividing the mixutre into several small containers. This avoids the exothermal heat build-up which would otherwise occur in mixture held in bulk. Divided into 50ml quantities, the mixture has usable life:

Temperature of mixture	25°C	40°C
Usable life	2½h	30 min

Mould filling

The resin mixture should be introduced in a steady stream, preferably into the bottom of the mould, so that the air is displaced from the assembly.

Curing

Minimum curing schedules depend on the performance level required of the completed units.
Initially, cure the cast mixture for at least: 24 hours at 25°C.
This schedule develops sufficient strength to permit demoulding. The properties may also be adequate for the particular service conditions.
Near maximum properties are obtained by post-curing:
2 days at 25°C or 8-10 hours at 40°C or 2 hours at 60°C
or 1¼ hours at 80°C or 1 hour at 100°C

Note These instructions are adapted from Vantico Instruction Sheet No. C.110 *Araldite CW 1301, Hardener HY 1300.* The Sheet gives fuller details on processing techniques and lists the properties (mechanical, electrical, etc.) of the cured resin-hardener system. Sheet No. C.110 is available on request.

Caution

Araldite resins and hardeners are generally quite harmless to handle provided that certain precautions normally taken when handling chemicals are observed. The uncured materials must not, for instance, be allowed to come in contact with foodstuffs or food utensils, and measures should also be taken to prevent the uncured materials from coming in contact with the skin, since people with particularly sensitive skin may be affected. The wearing of impervious rubber or plastics* gloves will normally be necessary; likewise the use of eye protection. The skin should be thoroughly cleansed at the end of each working period by washing with soap and warm water. The use of solvents is to be avoided. Disposable paper towels - not cloth towels - should be used to dry the skin. Adequate ventilation of the working area is recommended. These precautions are described in greater detail in Vantico Manual No. M.37 *Handling Precautions for Araldite Epoxy Resin Materials* and in the Vantico Product Safety Information Sheets for Araldite CW 1301 and Hardener HY 1300. The publications are available on request and should be referred to for fuller information.

Hardener HY 1300 is a corrosive and will cause irritation to sensitive skin. Particular care must be taken to observe the above precautions concerning measures to prevent the uncured materials from coming in contact with the skin. Further details are given in the Vantico Product Safety Information Sheet for Hardener HY 1300.

* A pair of plastics gloves is supplied in each resin-hardener pack.

Packed by Robnor Resins Ltd., Hunts Rise, South Marston Park, Swindon, Wilts. SN3 4TE
Tel No. 01793 823741 Fax No. 01793 827033

REVISION RECORD			
LTR	ECO NO:	APPROVED:	DATE:

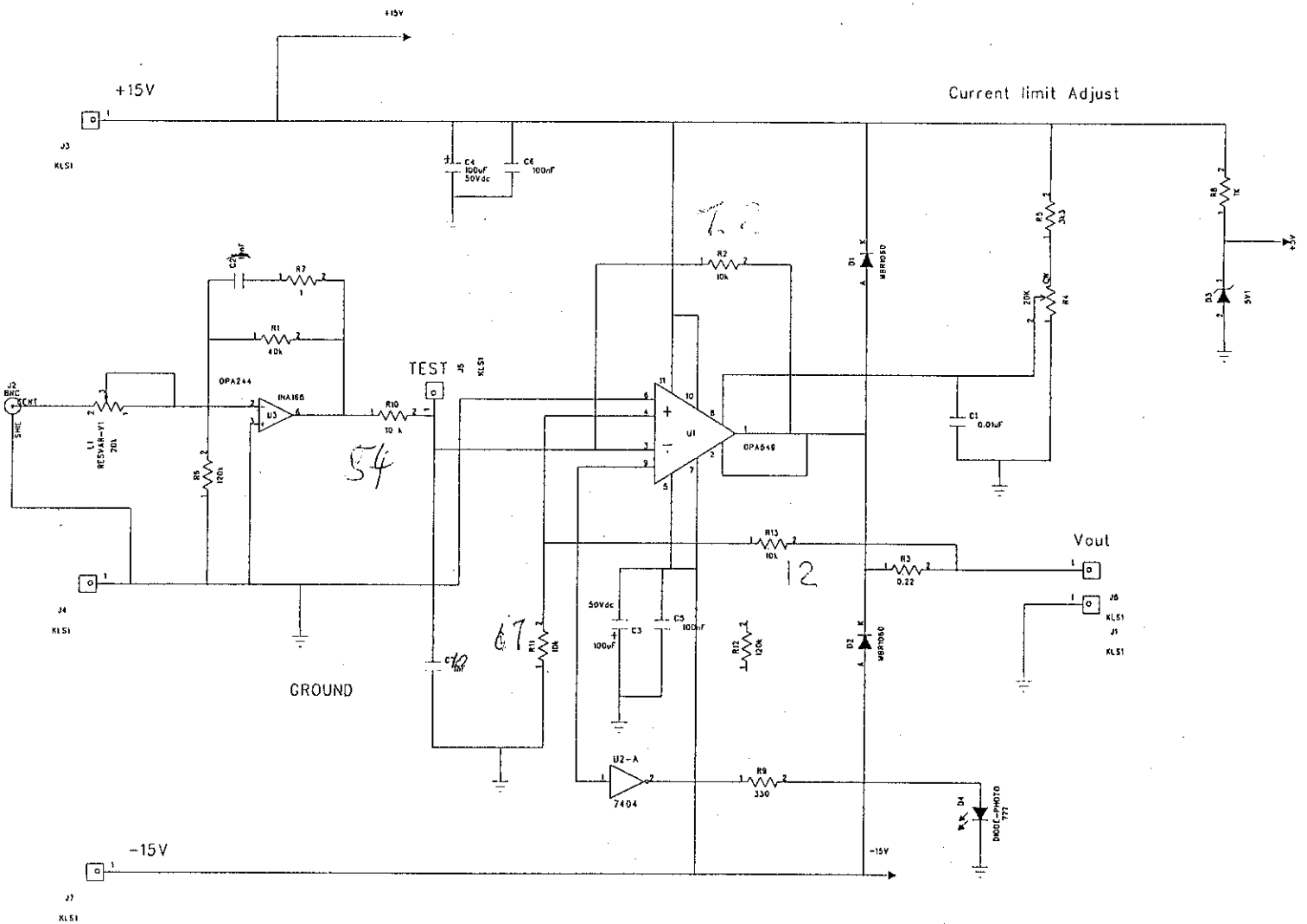

DRAWN:	DATED:	COMPANY:			
CHECKED:	DATED:	TITLE:			
QUALITY CONTROL:	DATED:	CODE:	SIZE:	DRAWING NO:	REV:
RELEASED:	DATED:	SCALE:		SHEET: OF	

ENGLISH

INSTRUCTIONS FOR USE FOR C.I.F. PRESENSIBILIZED

THE FINAL RESULT EXCLUSIVELY DEPENDS ON THE CARE TAKEN DURING EACH OPERATION

(please read these instructions before making your first circuit)

EXPOSURE

- Remove the adhesive protection from your C.I.F. positive light-sensitive plate.
- Place our film or original drawing on emulsion layer. (Pay special attention to placement ; component side or track side)
- Place the set (film + board) on your exposure unit.
- Expose your board :
  from 1' to 2"
  (make a test to calibrate your exposure unit).

DEVELOPMENT

Prepare the development in a tray
Pour the contents of CIF bag in the tray and add the quantity of water required (at 18° minimum).
Wait for the complete dissolution of the crystals.
Immediately after exposure, put the board into the developer and shake.
The photosensitive resin which has been exposed should disappear in less than 2 minutes. If development has not been totally carried out, please refer to the table at the end of the notice).
If the plate is not immediately etched, rinse it with running water.

ETCHING

To avoid a waste of time, heat your etching machine before exposing your circuit.
Put your circuit into the etching tank.
Etching agent will corrode the copper which is not protected by resin.
Etching time (with new ferric chloride) : from 45" to 2' into spray etching machine, from 5' to 8 ' into air pulsed etching machine or foam machine and 8' into foam machine) from 15 to 20' into a tank.
When etching time has doubled, change ferric chloride.
Rinse.

RESIN REMOVAL

With buffer or C.I.F. stripper.
Resin can be left during drilling to protect copper.
Etched board can be reexposed and resin destroyed with U.V. : plunge the board into the developer.
Your circuit is finished (you can either tin or varnish).

INCIDENT AND SOLUTION TABLE

INCIDENTS	CAUSES	SOLUTIONS
Photo sensitive circuit Development is not made	Exposure time too short Out of date plate. Development temperature too low – saturated developer.	Carry out test with grey scale (test film) and a new developer – Minimum temperature 18°C
Circuit cut during development or out of focus development	Bad contact of original on the plate - Mylar too thick - Drawing density not black enough – cut on the drawing	Improve pressing or check the machine – Make a contact film (C.I.F. reprophane film) . Check light table.
Copper full of holes after etching	Over exposed plate – drawing not opaque enough – bad contact – etching time too long	Check the original and make test with grey scale (test film)
No etching	Resin remains on the plate. Saturated etching agent	Increase exposure and development times – change etching agent.
Fine tracks after etching	U.V. pass under the original – under etching phenomenon – Mylar too thick	Improve contact. Improve etching system – Make a contact film – Place the photo layer against the resin

ADMISSIBLE (1A) INTENSITY INTO A CONDUCTOR

	Conductor width in mm									
Cu 35µ	0.36	0.4	0.72	1.14	1.78	2.5	3.5	4.5	5.8	7.1
Δ T°→ 20°C	1.2	1.3	2.7	3.8	5.2	6.8	8.3	9.7	11.2	13

ITALIANO

ISTRUZIONI PER L'USO PER PRESENSIBILIZZATI CIF

IL RISULTATO FINALE DIPENDE ESCLUSIVAMENTE DALLA CURA CON CUI OGNI OPERAZIONE VIENE SVOLTA

(Leggere queste istruzioni prima di eseguire il primo circuito)

ESPOSIZIONE

Togliere la protezione adesiva della lastra fotosensibile positiva C.I.F.

- Posizionare il film o il disegno originale sullo strato foto (badare alla sistemazione lato componente o lato piste)
- Porre l'insieme film + lastra sulla machina
- Esporre la lastra
  da 1 a 2 minuti.
  (fare una prova per calibrare il châssis di esposizione)

SVILUPPO

Preparare il rivelatore in una vasca.
Versare il contenuto del sacchetto C.I.F. nella vasca e aggiungere un litro d'acqua *(a 18°C minimo)*
Aspettare la completa dissoluzione dei cristalli.
Immediatamente dopo l'esposizione, immergere la lastra nel rivelatore ed agitare.
Tutta la resina fotosensibile che è stata esposta deve sparire in meno di 2 minuti.
Se lo sviluppo non è totalmente eseguito, riferirsi alla tabella alla fine dell'avvertenza.
Se la lastra non viene incisa immediatamente, risciacquarla sotto l'acqua corrente.

INCISIONE

Per non perdere tempo, fare scaldare la macchina da incidere prima di procedere all'esposizione del circuito.
Immergere il circuito
L'agente di incisione attacca il rame che non è protetto dalla resina..
Tempo di incisione (con percloruro nuovo) ; da 45" a 2' nelle macchine a polverizzazione, da 5' a 8' nelle macchine a pulsazione o 15' a 20' nella vasca.
Quando il tempo di incisione sarà raddoppiato , cambiare il percloruro. Risciacquare.

ELIMINAZIONE DELLA RESINA

Con un tampone e lo Stripper CIF.
Si può lasciare la resina durante il foraggio per proteggere il rame.
Si può ugualmente esporre di nuovo la lastra incisa e distruggere la resina con gli ultravioletti ; immergere di nuovo la lastra nel rivelatore.
Il circuito è finito.*(può essere stagnato o verniciato).*

INCIDENTI	CAUSE	SOLUZIONI
Circuiti fotosensibili. Lo sviluppo non viene eseguito	Tempo di esposizione troppo ridotto. Lastra scaduta. Temperatura di sviluppo troppo bassa. Sviluppo saturo.	Eseguire delle prove con una scala di grigio (film prova) e un rivelatore nuovo – temperatura minima 18°C.
Circuito tagliato allo sviluppo o sviluppo sfocato	Contatto scorretto dell'originale sulla lastra. Mylar troppo spesso. Densità del disegno non abbastanza nera. Taglio sul disegno.	Migliorare la pressatura o verificare la macchina. Fare un film contatto (film reprophane CIF). Controllare la tavola luminosa.
Rame pieno di buchi dopo incisione	Lastra sovraesposta. Disegno non abbastanza opaco. Cattivo contatto. Tempo di incisione troppo lungo.	Verificare l'originale e eseguire delle prove con la scala di grigio (film prova).
Nessuna incisione	Resina rimanente sulla lastra. Agente di incisione saturo.	Aumentare il tempo di esposizione ed il tempo di sviluppo. Cambiare l'agente di incisione.
Piste fini ridotte dopo incisione	Gli UV passano sotto l'originale. Fenomeno di sotto-incisione. Mylar troppo spesso.	Migliorare il contatto. Migliorare il sistema di incisione. Fare un film contatto. Posare lo strato foto contro la resina.

INTENSITÀ (1A) AMMISSIBILE NEL CONDUTTORE

Estratto di "preparazione di un circuito stampato" editato da Mecanorma

	Larghezza conduttore									
Cu 35µ	0.36	0.4	0.72	1.14	1.78	2.5	3.5	4.5	5.8	7.1
Δ T°→ 20°C	1.2	1.3	2.7	3.8	5.2	6.8	8.3	9.7	11.2	13

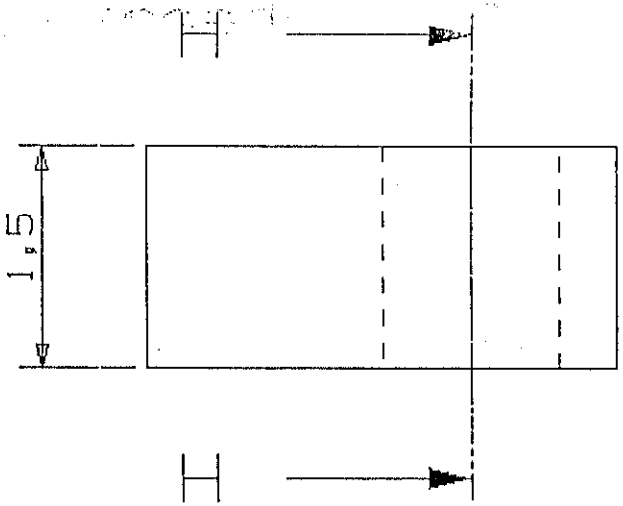

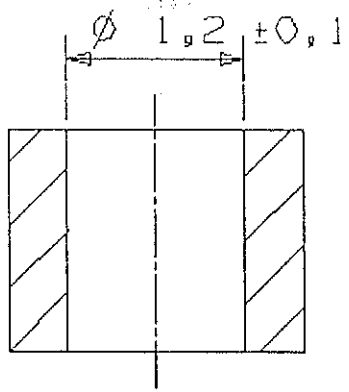

SECTION H-H

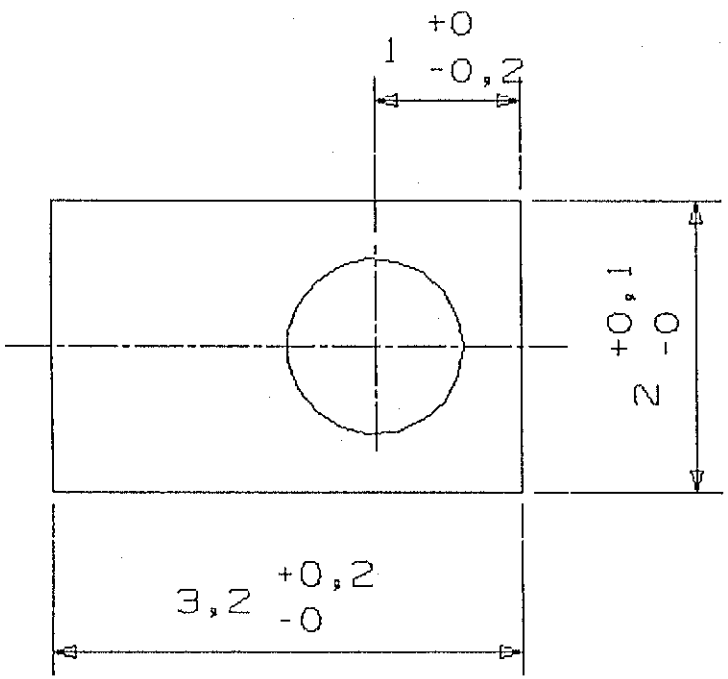

Part Name:	Spring clamp	Part Number:	S-2
Material:	MS58zh 2.0401	Scale:	20:1
Version:	1.1		
Tolerance	+/-0.2		
Designer:	C.Paulitsch	Design Date:	05.01.04
Checked by:		Review Date:	

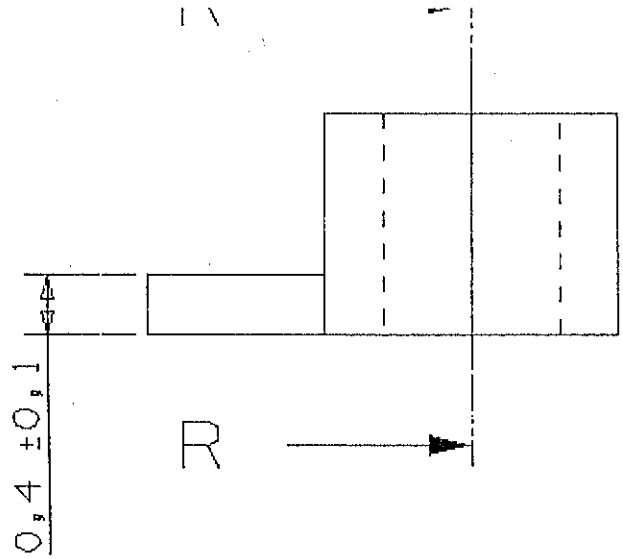

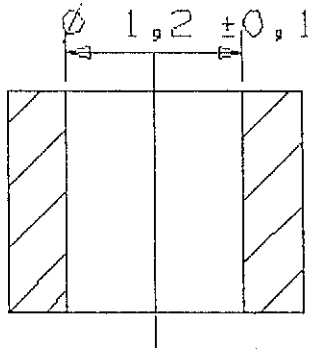

SECTION R - R

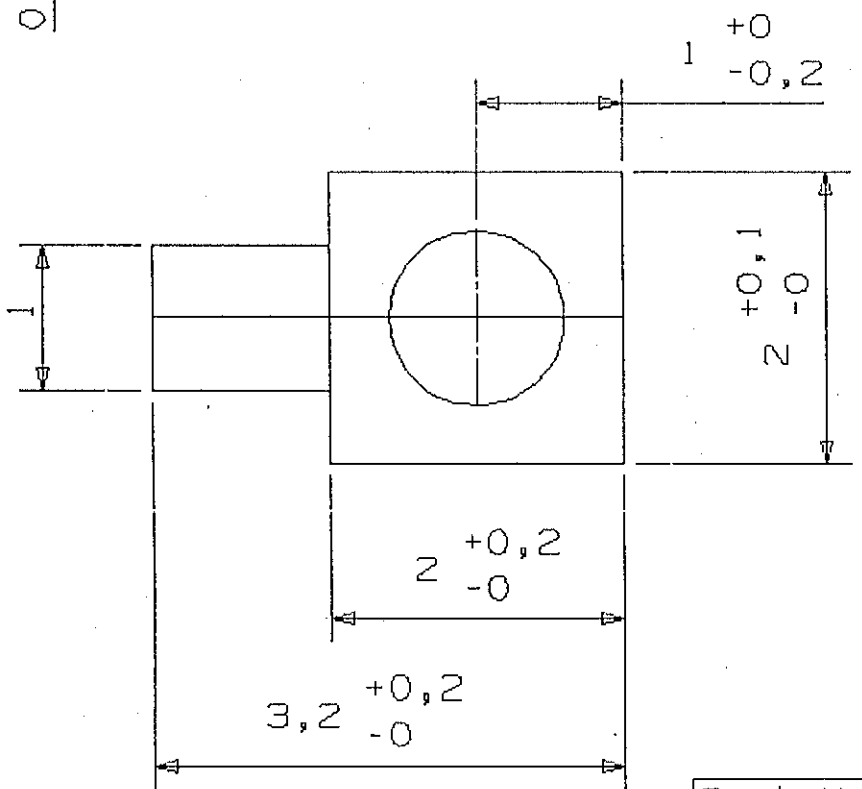

Part Name:	Spring clamp	Part Number:	S-2
Material:	Phosphore bronze CuSn6	Scale:	20:1
Version:	2.0	dimensions	in mm
Tolerance	+/-0.2		
Designer:	C.Paulitsch	Design Date:	05.01.04
Checked by:		Review Date:	

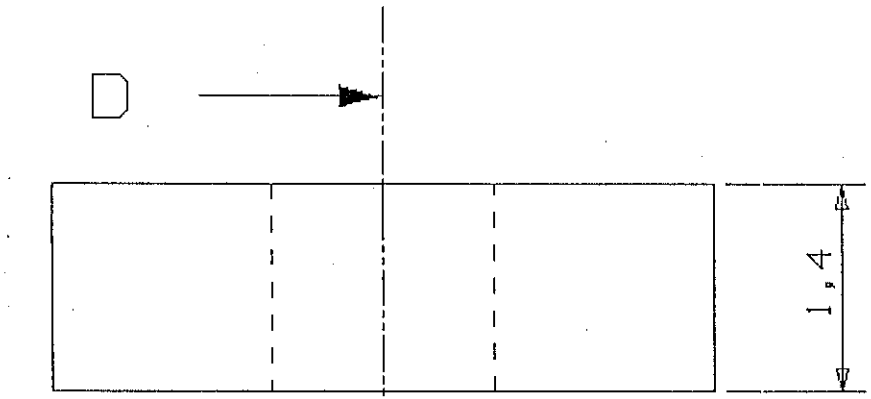

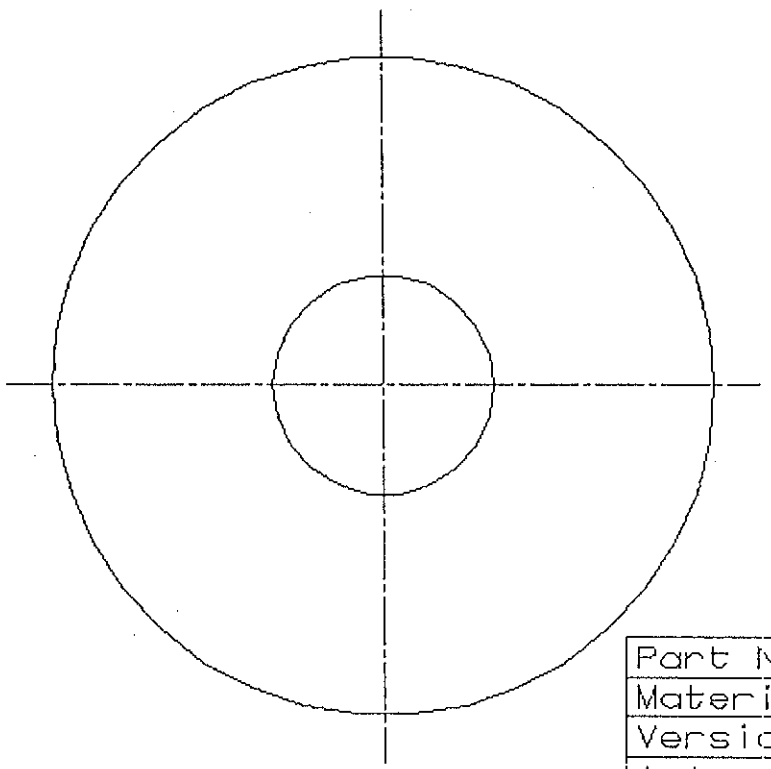

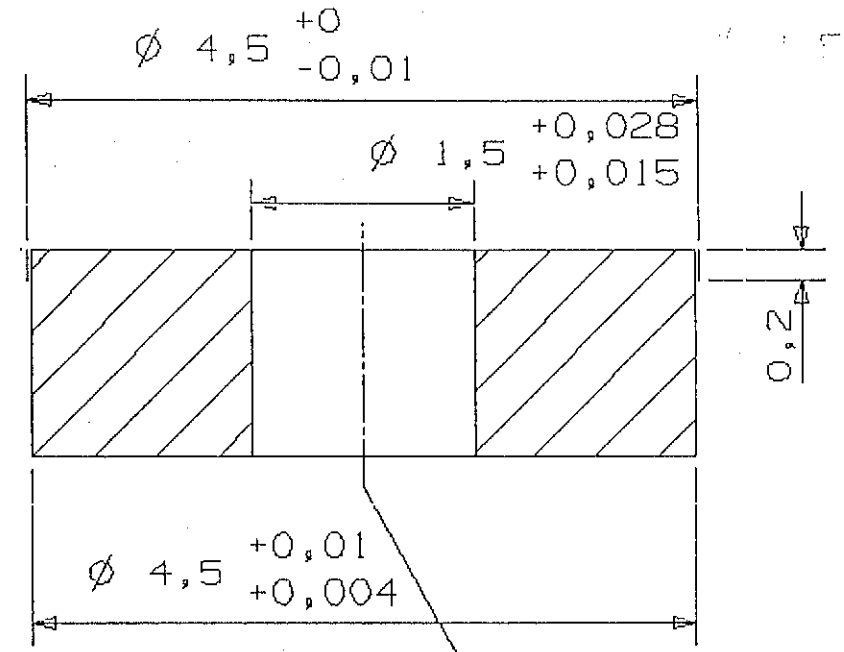

SECTION D - D

Hole made during assembly

Part Name:	Upper bushing	Part Number:	B-1
Material:	RG7 2.1090.04	Scale:	20:1
Version:	1.0	dimensions in mm	
Tolerance	+/-0,2	4,5 n6	+0,004/+0,01
Designer:	C.Paulitsch	Design Date:	19.11.03
Checked by:	R.Bonnen	Review Date:	24.11.03

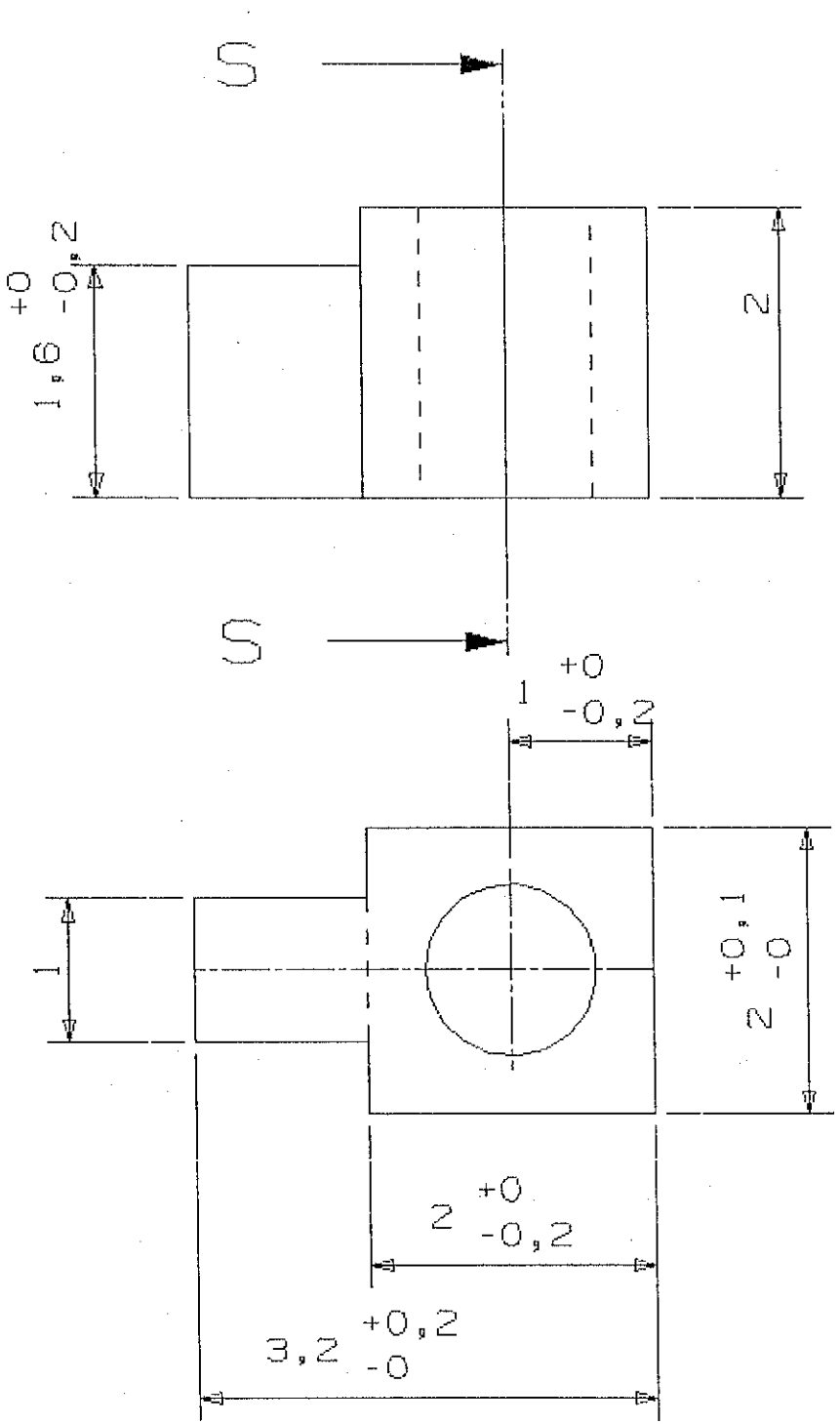

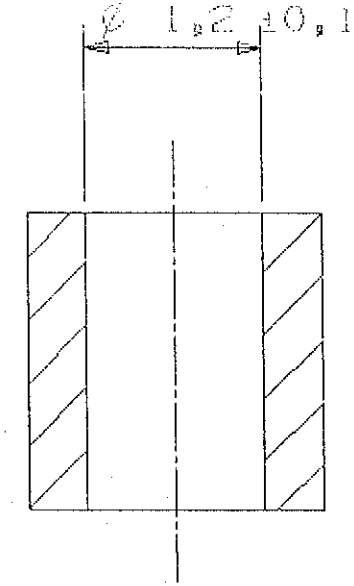

SECTION S-S

Part Name:	Spring Clamp	Part Number:	S-2
Material:	MS58zh 2.0401	Scale:	20:1
Version:	3.0	dimensions	in mm
Tolerance	+/-0.2		
Designer:	C.Pavlitsch	Design Date:	06.01.04
Checked by:		Checked Date:	

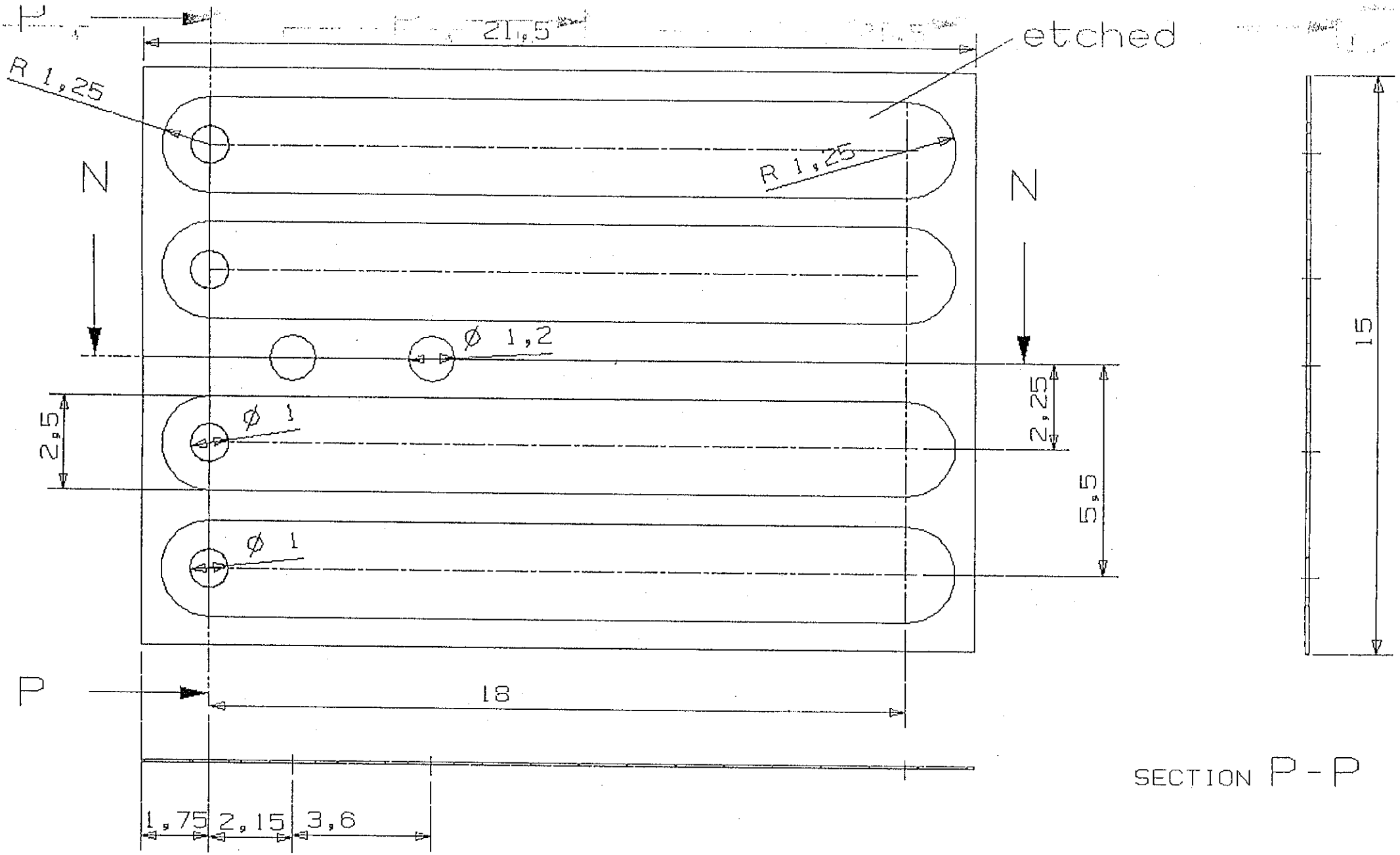

Section N-N

SECTION P-P

Part Name:	Connector Plate	Part Number:	CON-1
Material:	PCB	Scale:	8:1
Version:	1.3	dimensions	in mm
Tolerance	+/-0.2		
Designer:	C.Paulitsch	Design Date:	04.12.03
Checked by:	R.Pinnegar	Review Date:	08.01.04

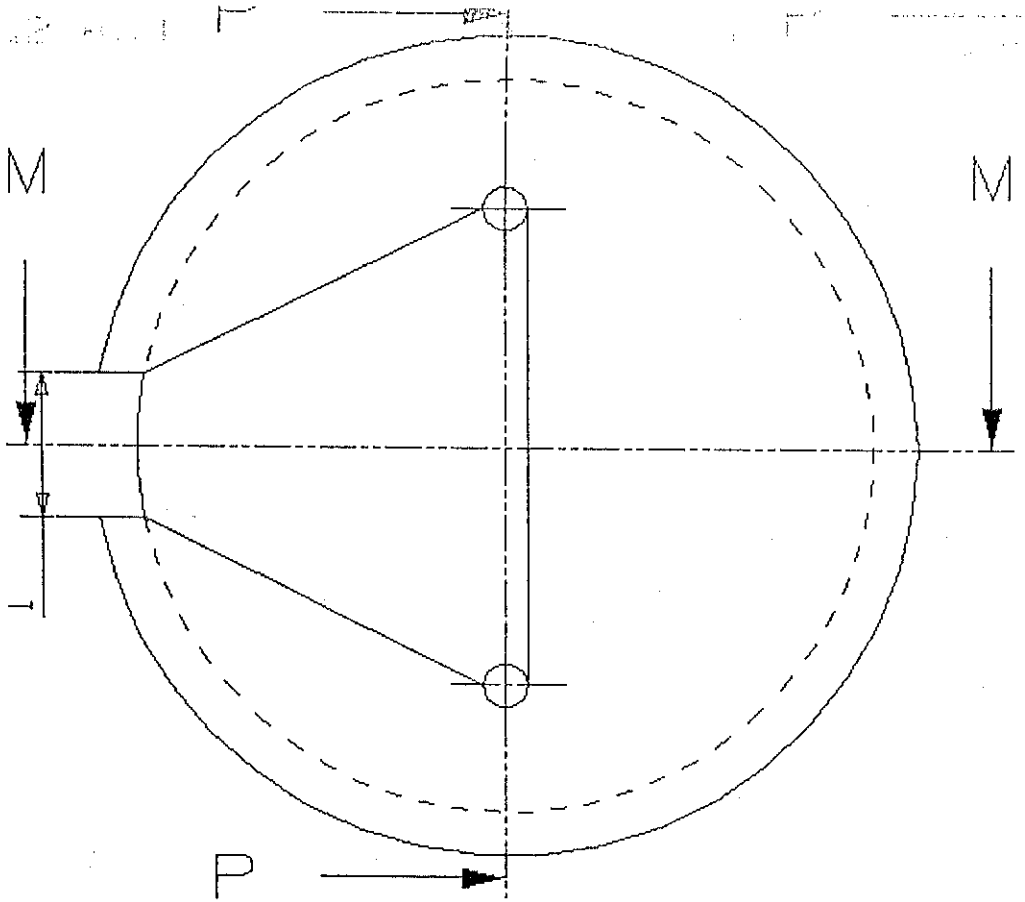

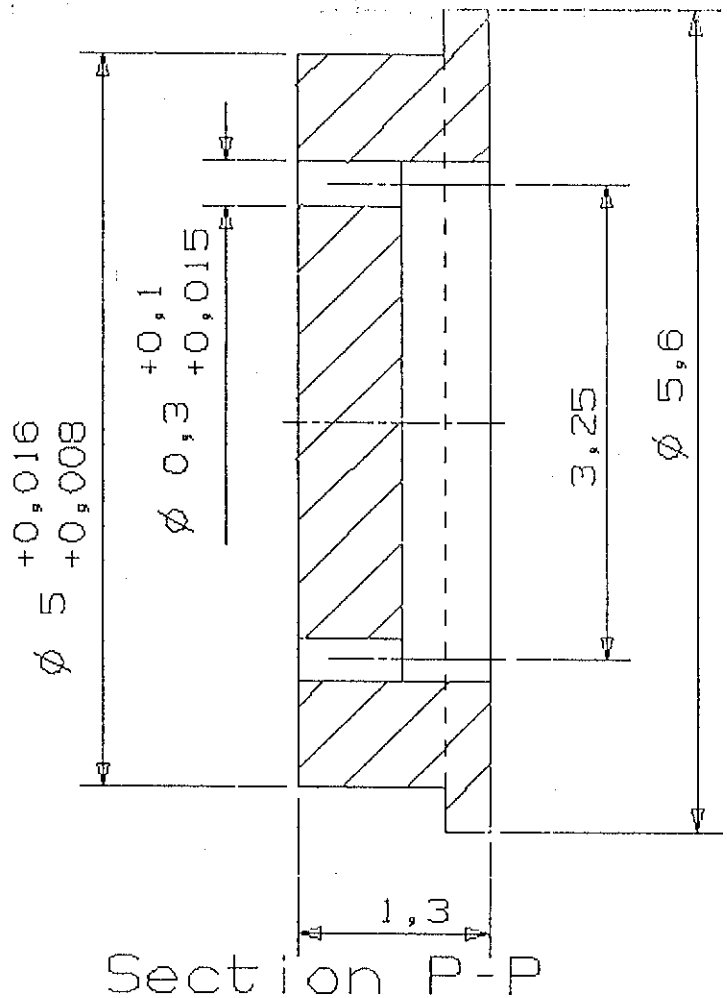

Section P-P

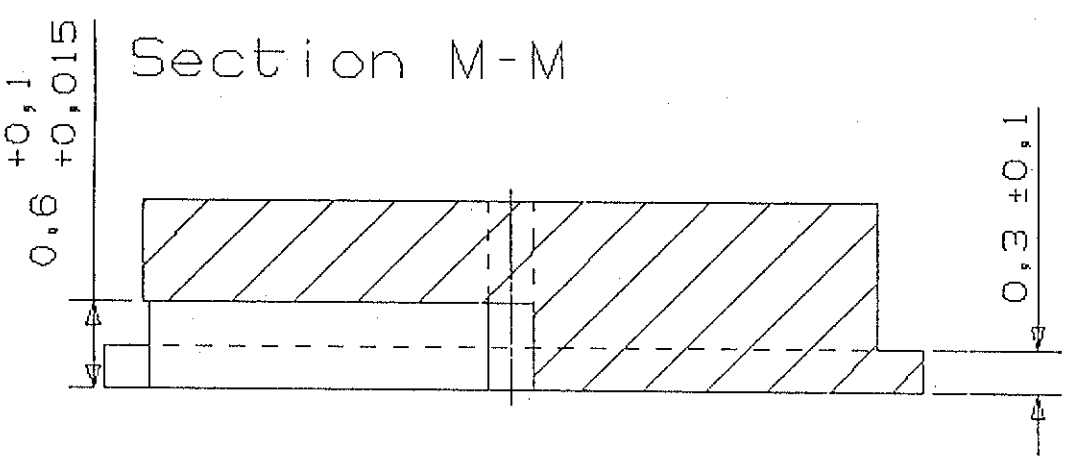

Section M-M

Part Name:	CABLE SEAL	Part Number:	CON-2
Material:	PTFE	Scale:	20:1
Version:	1.2	dimensions	in mm
Tolerance	+/- 0,2		
Designer:	C.Paulitsch	Design Date:	05.01.04
Checked by:	R. Penner	Release Date:	05.01.04

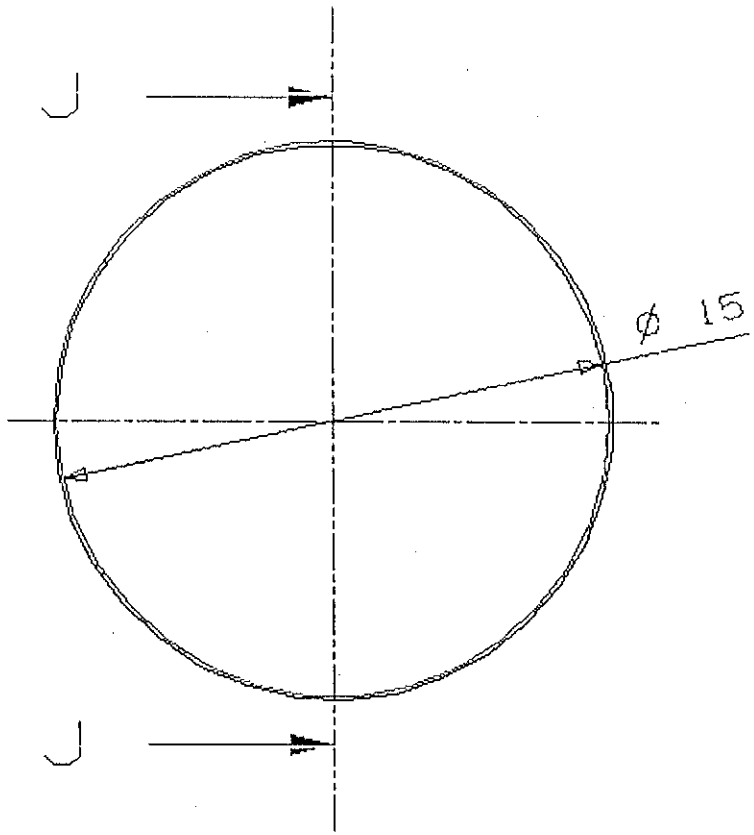

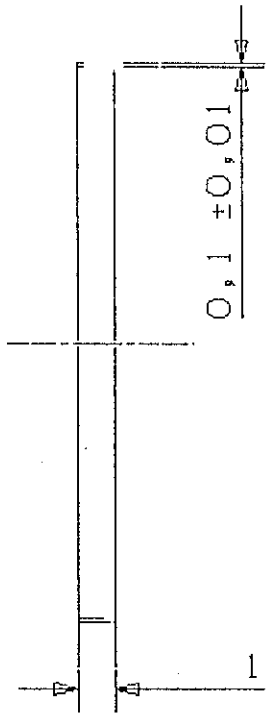

SECTION J - J

Part Name:	Circle spring	Part Number:	S-1
Material:	Phosphor bronze CuSn6	Scale:	5:1
Version:	1.0	dimensions	in mm
Tolerance	+/-0.2		
Designer:	C.Pavlitsch	Design Date:	26.11.03
Checked by:		Review Date:	

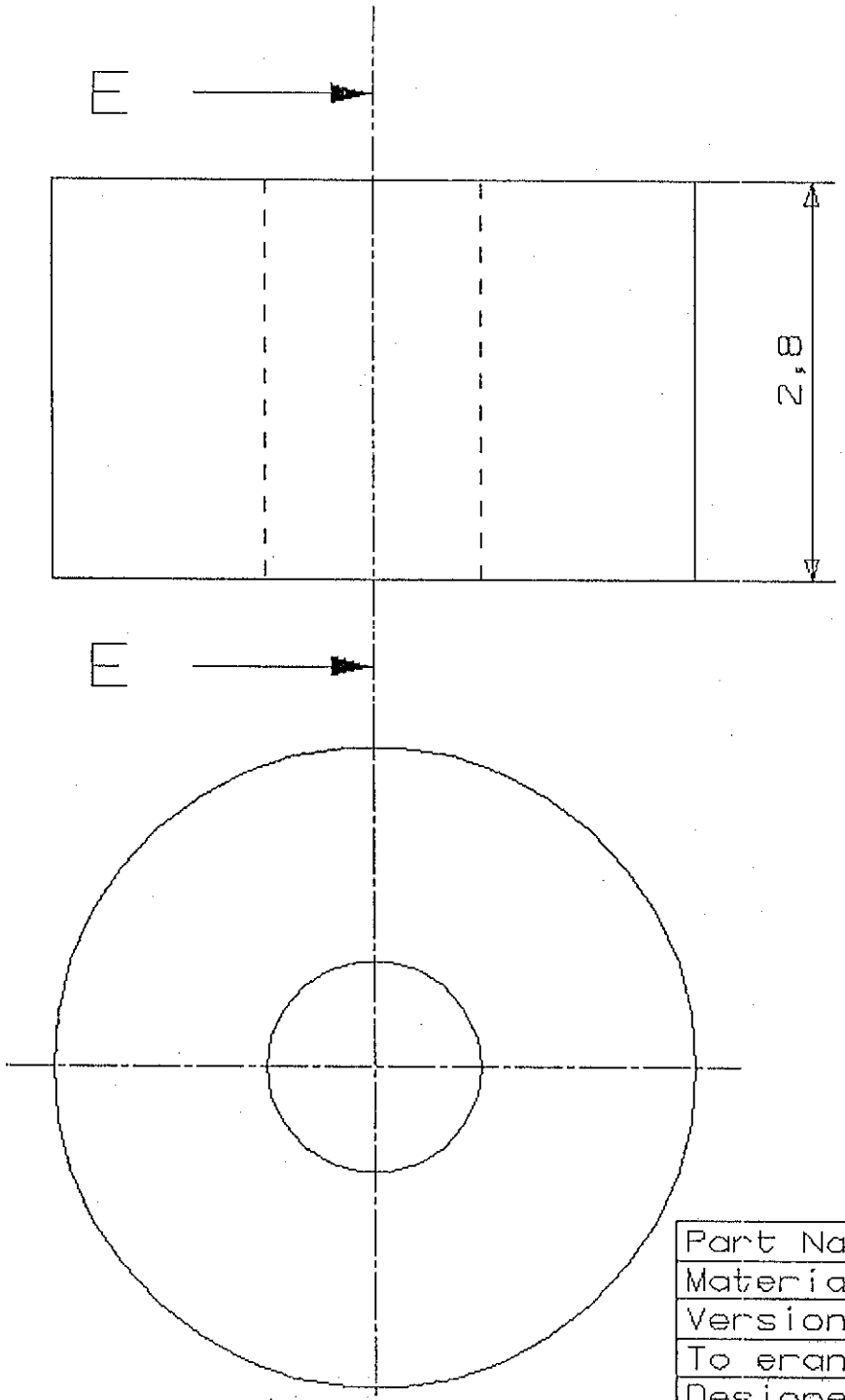

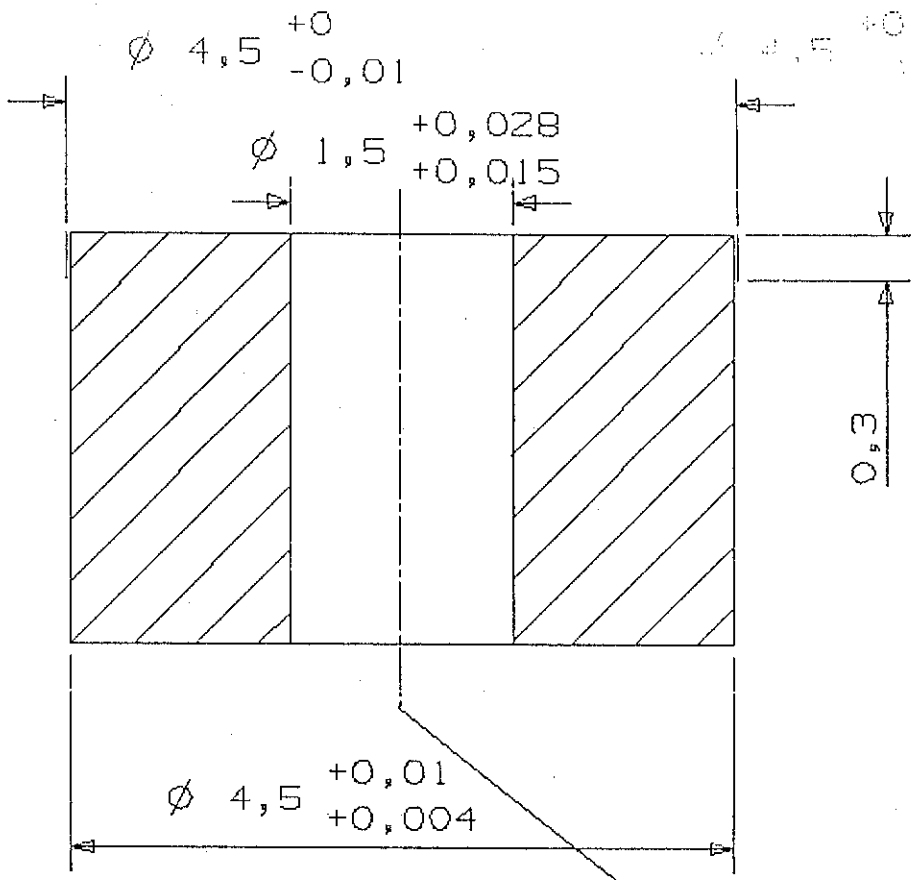

SECTION E - E

Hole made during assembly

Part Name:	Lower Bushing	Part Number:	B-2
Material:	RG7 2.1090.04	Scale:	20:1
Version:	1.0	dimensions in mm	
To erance	+/-0.2	4,5 n6	+0,004/+0,01
Designer:	C.Paulitsch	Design Date:	19.11.03
Checked by:	R.Boonen	Review Date:	24.11.03

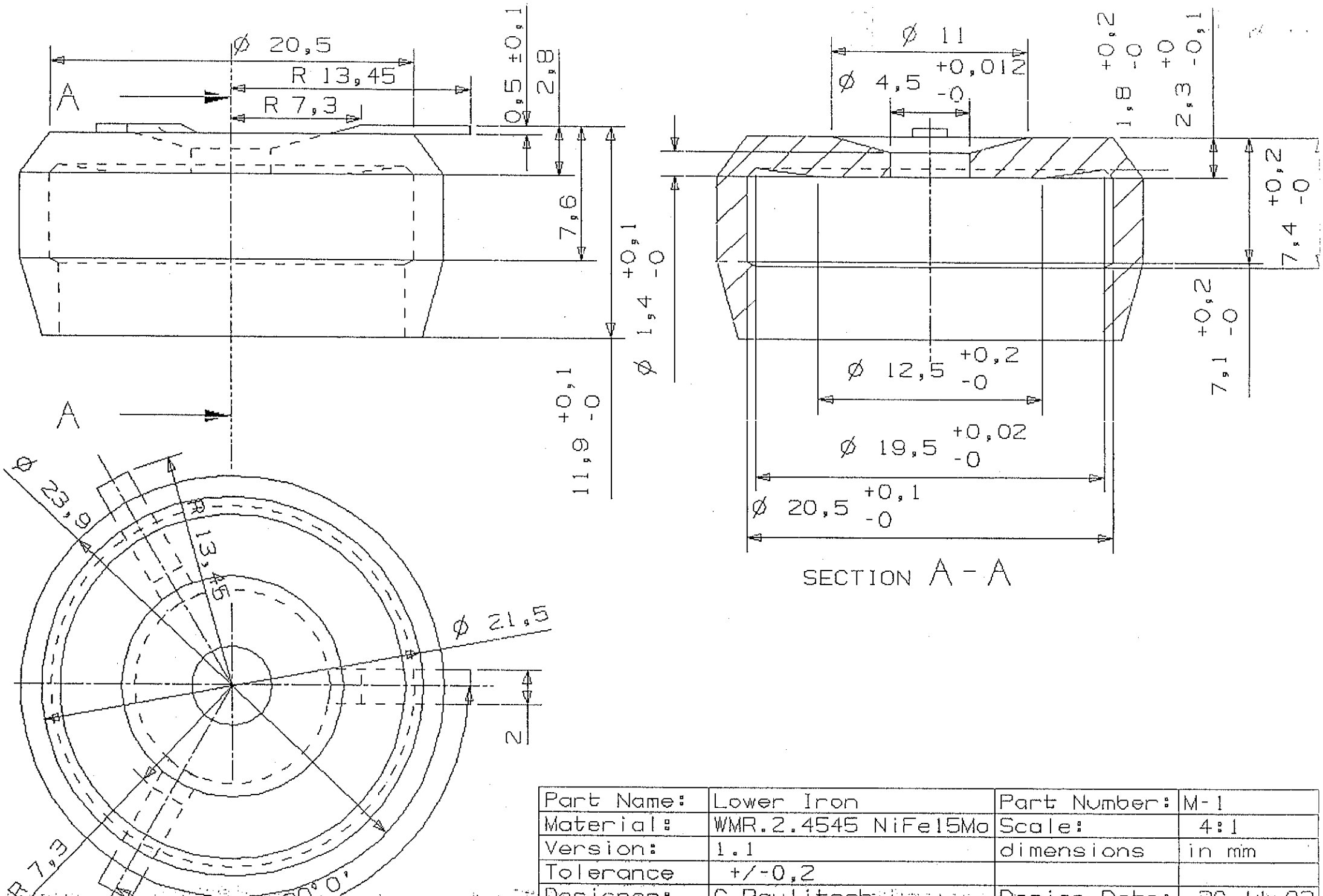

Part Name:	Lower Iron	Part Number:	M-1
Material:	WMR.2.4545 NiFe15Mo	Scale:	4:1
Version:	1.1	dimensions	in mm
Tolerance	+/-0,2		
Designer:	C.Paulitsch	Design Date:	26.11.03
Checked by:	R.Reenen	Date:	01.12.03

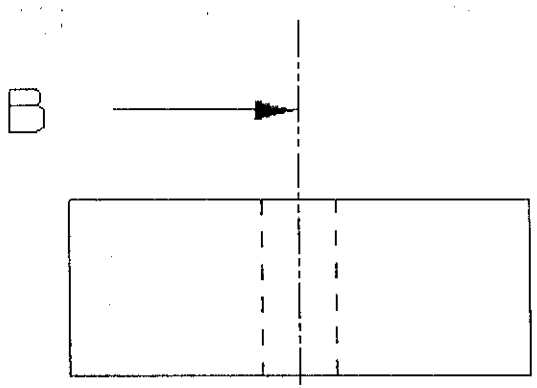

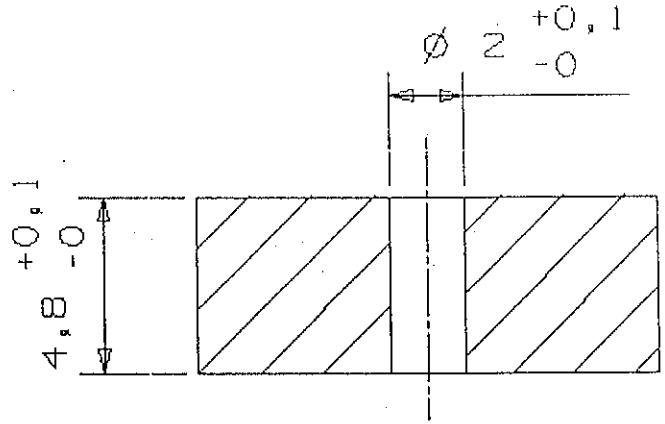

SECTION B - B

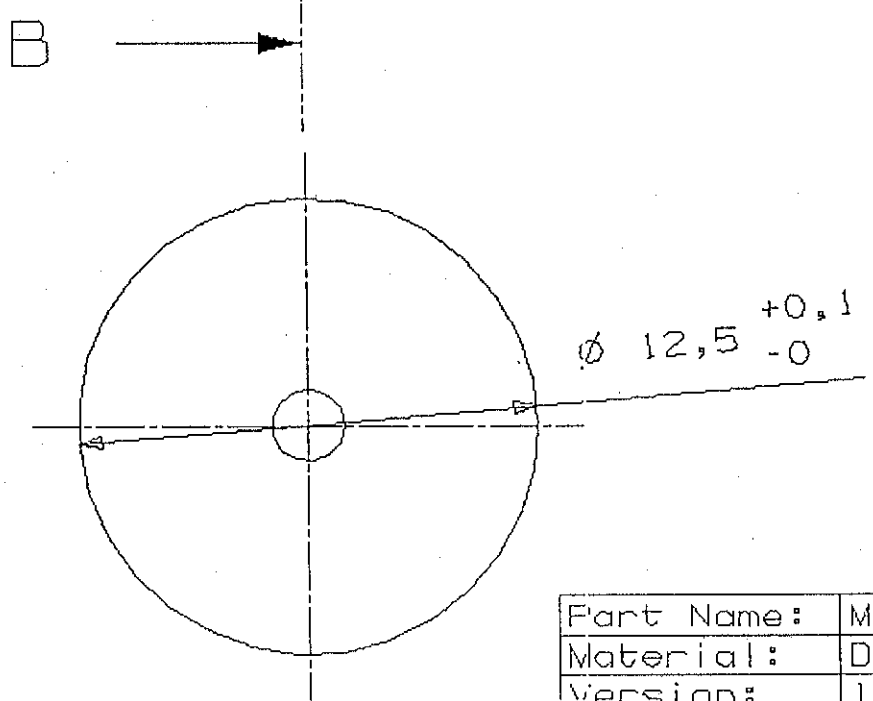

Part Name:	Magnet	Part Number:	M-2
Material:	DIN 385/111 N48	Scale:	5:1
Version:	1.0	dimensions in mm	
Tolerance	+/-0,2		
Designer:	C.Paulitsch	Design Date:	18.11.03
Checked by:	R.Boonen	Review Date:	24.11.03

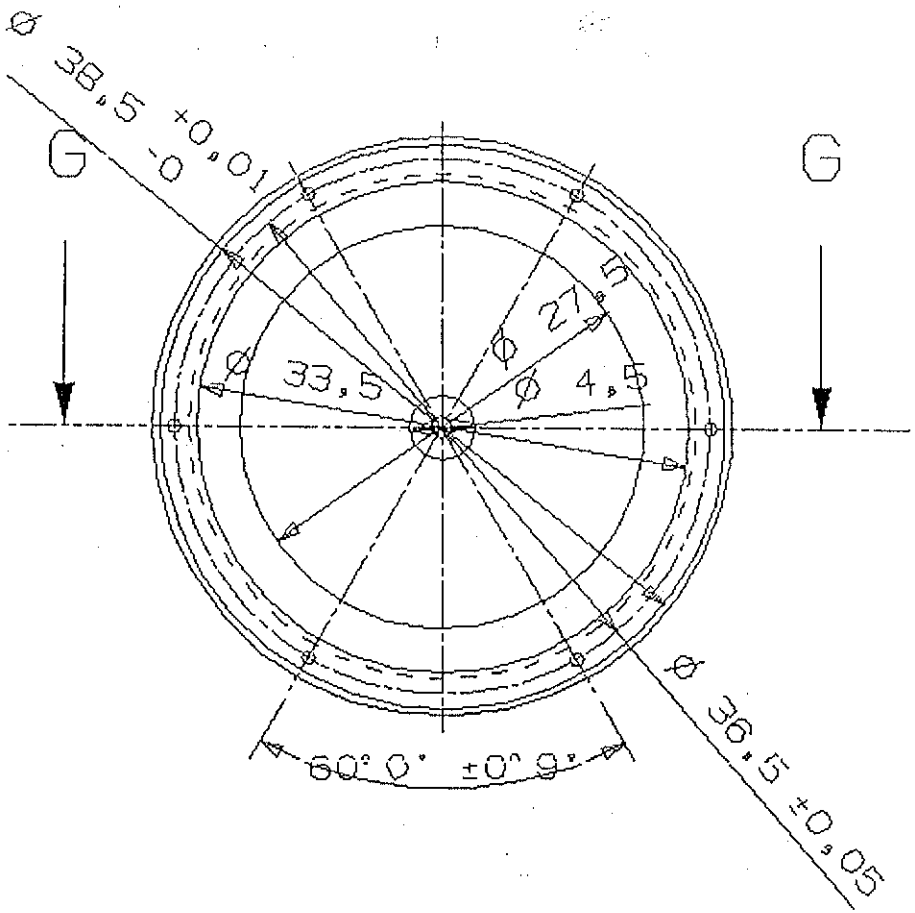

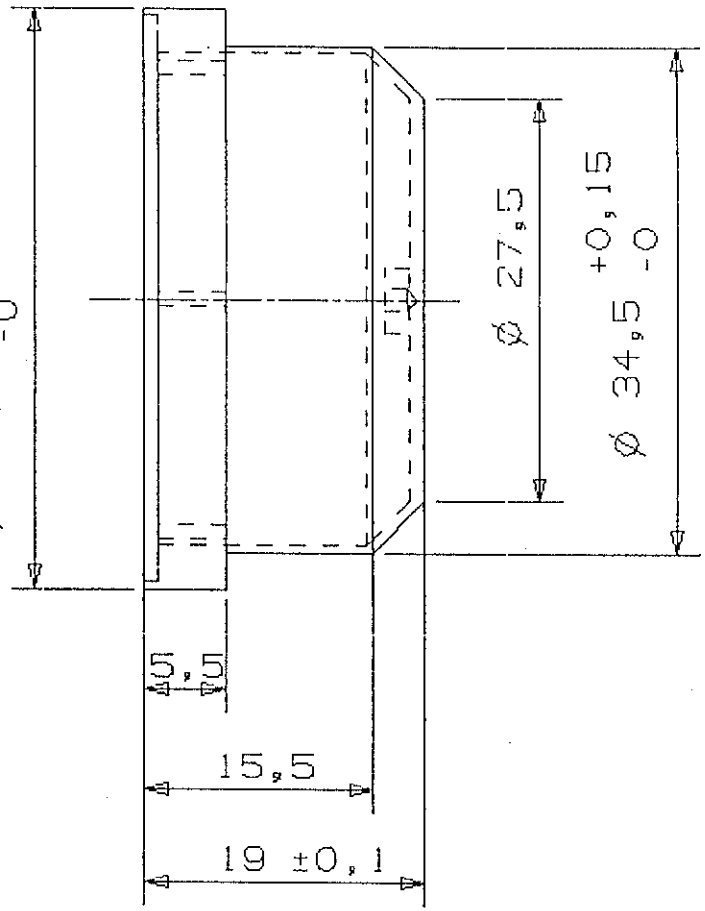

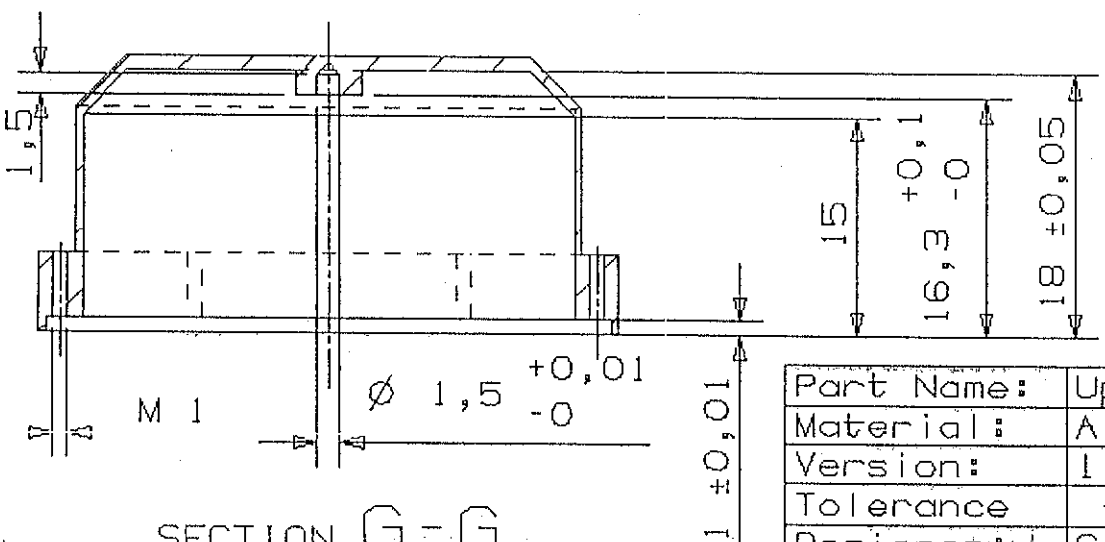

SECTION G - G

Part Name:	Upper Cover	Part Number:	C-2
Material:	AlMgSi1 F28 1F3/50ST	Scale:	2:1
Version:	1.1	dimensions	in mm
Tolerance	+/-0,2		
Designer:	C.Paulitsch	Design Date:	26.11.03
Checked by:		Review Date:	

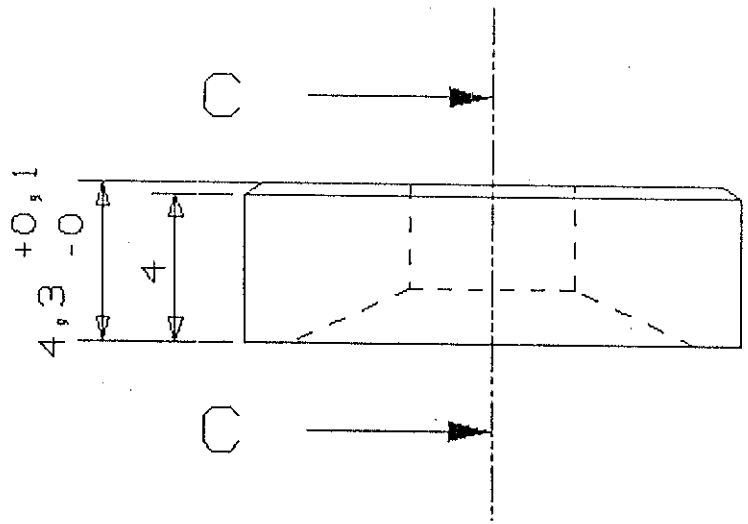

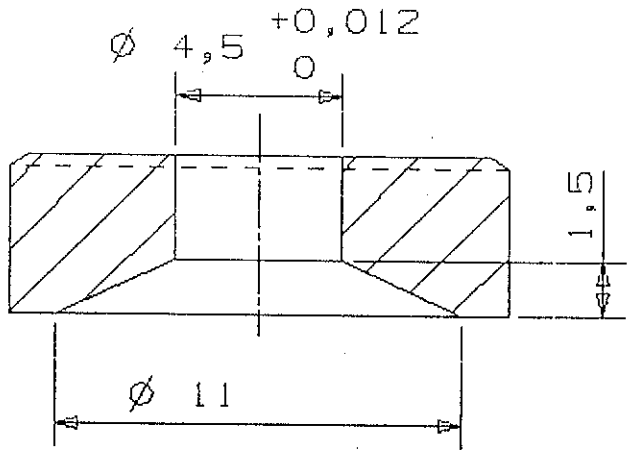

SECTION C - C

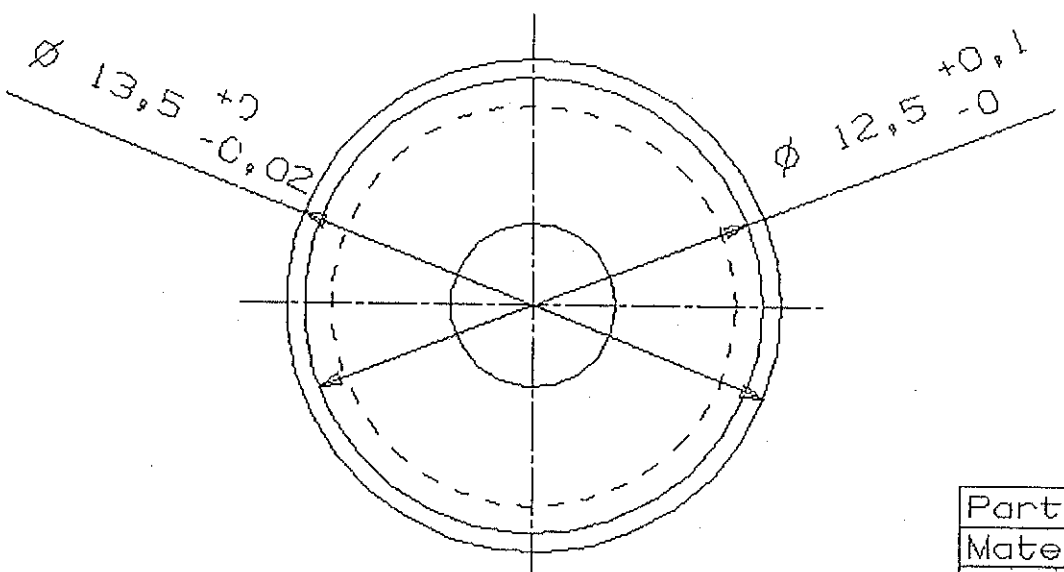

Part Name:	Upper Iron	Part Number:	M-3
Material:	WMR.2.45.45	Scale:	5:1
Version:	1.0	dimensions in mm	
Tolerance	+/- 0,2		
Designer:	C.Paulitsch	Design Date:	19.11.03
Checked by:	R.Kapper	Review Date:	24.11.03

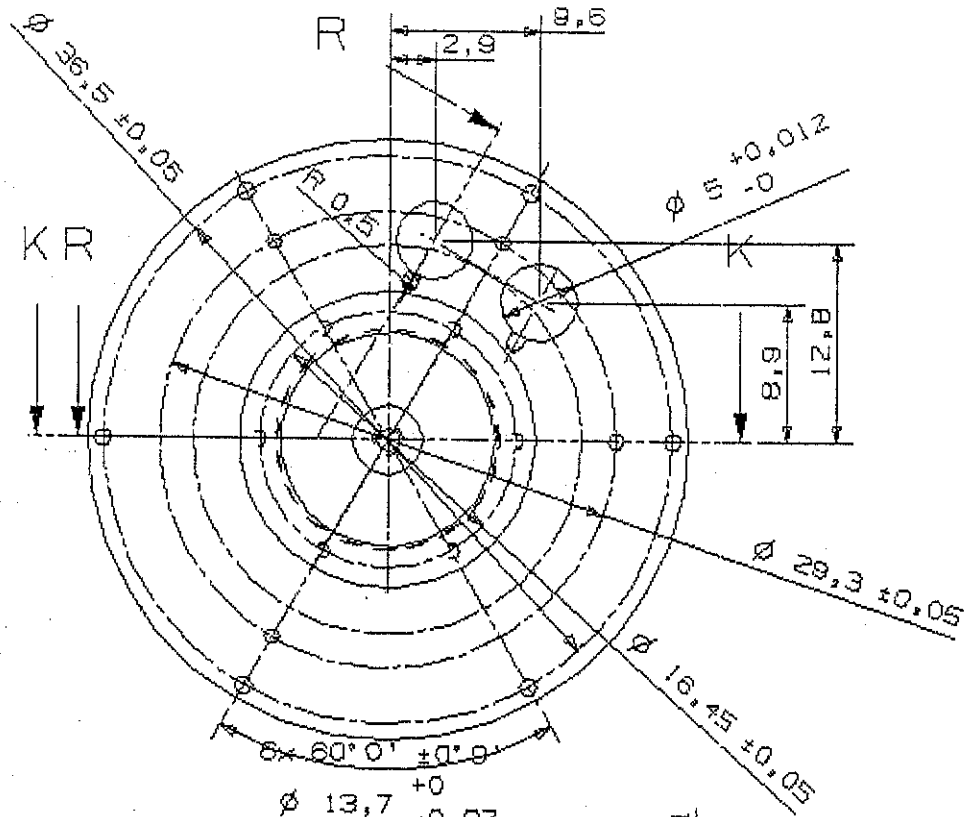

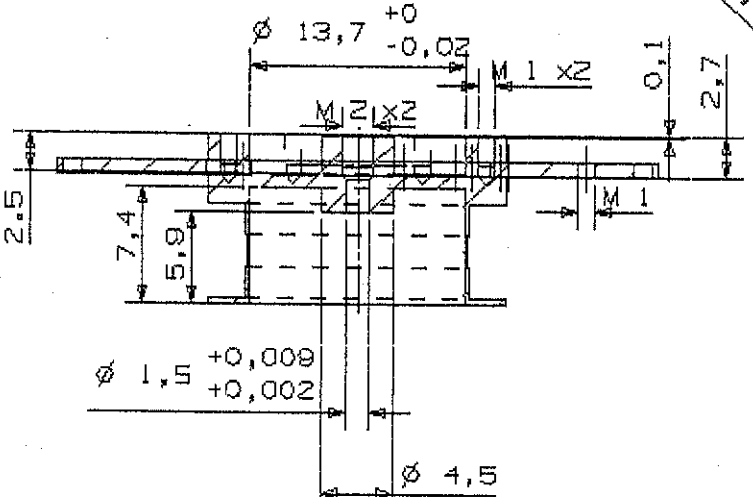

SECTION K-K

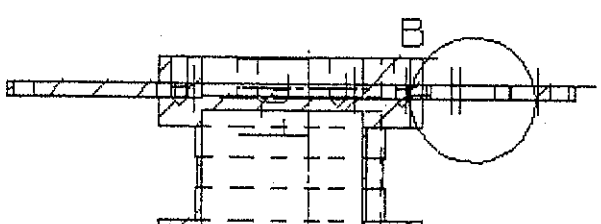

SECTION R-R

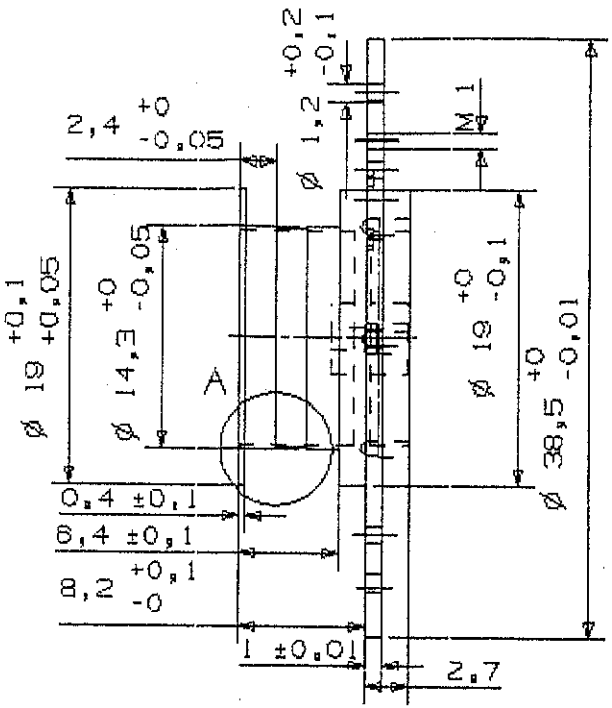

Detail A

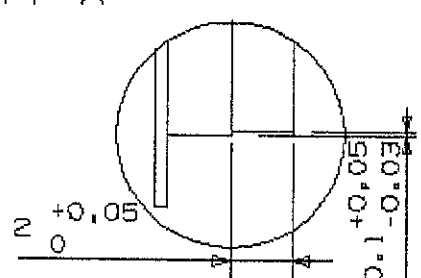

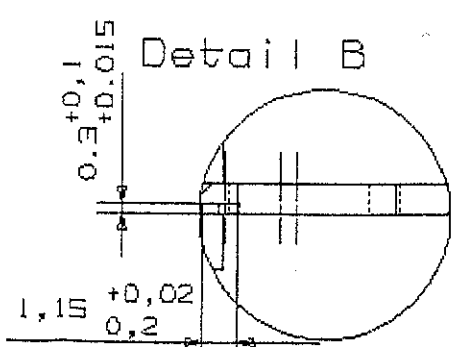

Detail B

Part Name:	Lower cover	Part Number:	C-1
Material:	AlCuMgPb	Scale:	4:1
Version:	1.4	dimensions	in mm
Tolerance	+/-0.2		
Designer:	C.Paulitsch	Design Date:	06.01.
Checked by:		Review Date:	